UNIVERSITY OF SOUTHAMPTON

FACULTY OF NATURAL AND ENVIRONMENTAL SCIENCE

School of Chemistry

Theory and spectroscopy of dihydrogen endofullerenes

by

Salvatore MAMONE

Thesis for the degree of Doctor of Philososphy

November 2011

UNIVERSITY OF SOUTHAMPTON

Abstract

FACULTY OF NATURAL AND ENVIRONMENTAL SCIENCE
School of Chemistry
Doctor of Philosophy

THEORY AND SPECTROSCOPY OF DIHYDROGEN ENDOFULLERENES

by
Salvatore Mamone

Recent advances in synthetic chemistry made available a new class of fascinating compounds in which a molecule of hydrogen is encased inside the hollow cavity of the highly symmetric fullerene C_{60}. There is a great interest in studying endohedral fullerene complexes owing to the rigidity, symmetry, homogeneity and isolation provided by the carbon cages. On one side these properties result in very detailed and well-resolved spectra even in the condensed phase. On the other side such supermolecules are a unique real-world example of a quantum rotor confined in an almost spherical trap, whose dynamics can be directly and accurately treated from first principles. The study of the quantum dynamics and the analysis of the spectroscopic observations of $H_2@C_{60}$ provide a stepping stone for the characterization of the carbon-hydrogen interaction in curved nanocarbons.

In this work symmetry is employed to simplify the analytical treatment of the dynamics of the endohedral hydrogen, by expanding the non-bonding confining potential in terms of spherical multipoles and by using a spherical basis to represent the effective rotational-translational Hamiltonian. The thesis features the first study of an endohedral hydrogen fullerenes, $H_2@C_{60}$, by infrared spectroscopy . The quantization of the translational motion, the high rotational freedom and rotational-translational couplings clearly show up in the infrared spectra. The successful assignment of the IR peaks to transitions between the quantum states of the confined hydrogen by means of the presented theoretical model has lead to the first accurate determination of the molecular vibro-rotational parameters and effective hydrogen-cage potentials in $H_2@C_{60}$.

The nuclear spin dynamics is very sensitive to the local environment around the hydrogen molecules. Nuclear magnetic resonance spectroscopy at cryogenic temperatures shows that the symmetry at the center of the cages is reduced by solid state effects and/or occluded impurities. The observations of small but not yet completely understood discrepancies in the lineshapes and relaxations of two samples of $H_2@C_{60}$ stress the influence of the preparation, storage and manipulation on the nuclear spin dynamics of endohedral hydrogen fullerenes.

Contents

List of Figures

List of Tables

Declaration of Authorship

This thesis is the result of work done wholly while I was in registered candidature for a Ph.D. degree at this University. The material presented herein is based on work mostly done by myself. Where the work was carried out jointly with others, a substantial part is my own original work and co-workers and their roles have been, clearly, indicated. The material contained herein has not been submitted by the author for a degree at any other institution.
Date: February 6, 2012

Signed:

Acknowledgments

Here I would like to express my gratitude to the people who made my Ph.D. experience valuable and pleasant.

Firstly I wish to thank my surpevisor, Malcolm H. Levitt, for all his advice during my PhD. I am very grateful for the guidance, the suggestions and the patience he showed during this time in which I learnt a lot, not only about science. Thanks Malcolm for being such a great mentor to me! I have to thank also all the previous and current members of the group who contributed to my personal and scientific growth, especially Marina, Ole, Sergey, Axel, Ilde, Andrea, Michael, Peppe and Maria. In particular Marina thought me the rudiments of NMR and helped me through my first year. Marina also started the ongoing and successful collaboration with Toomas Room and coworkers for the study of the infrared spectroscopy in endohedral fullerenes. Thanks to Ole, our engineer, for preparing the cryostatic NMR instrumentations in Southampton from scratch and for his technical support. I am indebted to Peppe for the countless discussions and exchange of ideas and I hope our collaboration will be as fruitful in the future.

This work would not have been possible without the collaboration with the Japanese group of Prof. Komatsu and Murata, and the American group of Prof. Turro, who synthesized and kindly provided all the endohedral hydrogen fullerene samples. Their amazing work is the source of much of the research in the field today.

The milliKelvin study was possible thanks to the collaboration with Prof. John Owers-Bradley and coworkers in Nottingham. In particular thanks to Kuldeep Panesar for all the help during such experiments.

During my Ph.D. I had the opportunity to visit the group of professor Nicholas J. Turro, aka the Boss, at Columbia University in New York. His enthusiasm, dynamism and curiosity for science will always be a source of inspiration to me. I greatly appreciated the hospitality of Steffen and the heartiness of Mrs. Turro. Thanks to Judy and Alberto, two of the nicest persons I have ever met, with whom I had my best and most enjoyable moments there.

A special thank goes to Peppe, Maria, Rosa and Gerardo, Pietro, Miko, Asia, Grzesiu and Agnieszka. It was really a pleasure to have met such great people! In particular

Maria and Rosa were such a kind friends and colleagues. I am very grateful to Agnieszka, with whom I shared all the good and bad times during these years, for bearing with me during the writing of this thesis: dziekuie kochanie moje.

Finally I have to thank my family, my brothers Carmelo, Vincenzo, Domenico and my mother Maria for the encouragement and support during all the hard times I encountered in my PhD. This work is dedicated to the memory of my father who always insisted on the importance of improving ourselves and our education. I believe he would be proud to know that I finally completed this work.

S.Mamone,
September 2011,
Southampton.

Chapter 1

Introduction

The supramolecular complex $H_2@C_{60}$, represented in figure 1.1, combines H_2, the simplest molecule of all, with one of the most symmetric molecules, the fullerene C_{60}. While hydrogen is among the most well known and studied molecules C_{60} was discovered in 1985 in the vapors of a laser-ablated graphite rod [4]: it is composed of 60 carbon atoms arranged so to form a soccer ball shaped molecule. It is the prototype of fullerenes, a class of carbon based molecules in which the atoms organize in closed and often very symmetric nanoscopic structures. The nomenclature stresses the guest-at-host configuration: hydrogen is included inside the cavity of the fullerene molecule.

In this introductory chapter the basic properties and structure of the two molecular units, hydrogen and C_{60}, the procedure adopted to synthesize the complex and the principal spectroscopic techniques used so far to study it are reviewed.

Figure 1.1: The supra molecular complex $H_2@C_{60}$.

1.1 Spin isomers of molecular hydrogen

Because of its simplicity hydrogen has always been used to test the understanding of quantum mechanics. The prediction of the existence of para- and ortho-hydrogen as the two distinct allotropes (isomeric forms of a single element) of molecular hydrogen was an early triumph of quantum mechanics. The quantum basis for the two forms is

as follows: H_2 is composed of two sets of identical spin 1/2 particles, two protons and two electrons. Both electrons and protons are fermions. The Pauli principle requires the total molecular wave-function to be antisymmetric for exchange of the space and spin coordinates of the two indistinguishable protons. The proton spins can combine in a symmetric way to give a total nuclear spin of 1 or in an antisymmetric way to give a total nuclear spin of 0, giving rise to the distinct species of ortho and para-hydrogen. In a diatomic molecule, with no net electronic angular momentum and spin, the spatial symmetry for exchange of the nuclei is determined by the parity $(-1)^j$ where $j = 0, 1, \ldots$ is the rotational angular momentum quantum number. As a result, in the electronic ground state, para-H_2 (antisymmetric singlet spin function) is associated with symmetric rotational functions ($j = 0$, even), and ortho-H_2 (symmetric triplet spin function) is associated with rotational wave-functions that are antisymmetric (j=odd). Similar considerations hold for the heavier isotopomer D_2 whose nuclei are bosons with spin 1. In that case the molecular wave-function is symmetric by exchange of the nuclear coordinates and the symmetric spin combinations (ortho-D_2) have either spin 2 or 0 while the antisymmetric combination (para-D_2) has spin 1. In the electronic ground state ortho-D_2 is associated with symmetric rotational functions ($j = 0$, even) while para-D_2 is associated with antisymmetric rotational functions (j = odd). The concept of spin isomerism has no sense in the heteronuclear HD molecule and there is no selective link between the nuclear spin state and the rotational quantum number.

The existence of ortho and para isomers is relevant in hydrogen since interconversion between the two species is slow in the absence of a catalyst. The reason is that for light molecules the separation between rotational energy levels is large and typical intramolecular interactions are either spin independent or symmetric by exchange of the two equivalent nuclei. The role of a catalyst, usually a paramagnetic substance, is to introduce a non-symmetric spin interaction at the nuclei which connects efficiently ortho and para manifolds so enhancing the conversion process. In the absence of a spin catalyst, ortho and para isomers form two independent thermal reservoirs since internal thermalization among all the degree of freedom is reached much faster than interconversion. The thermal equilibrium at room temperature is a statistical mixture of ortho- and para- species with a ratio 3:1 in the case of H_2 and 2:1 in the case of D_2. Many measurable quantities are determined by the relative abundance of the ortho and para species which depends on the history and preparation of the sample. Farkas' book [5] is an excellent introduction to the basic theoretical aspects and early experimental observations of spin isomerism and spin interconversion in molecular hydrogen.

1.2 Overview of C_{60} structure

In the C_{60} fullerene molecule the 60 carbon atoms are arranged at the vertices of a truncated icosahedron. This structure has been proposed on the discovery of the molecule and received numerous confirmations since then. In a truncated icosahedron there are

12 pentagonal faces and 20 hexagonal faces: each pentagonal face is surrounded by 5 hexagons and each hexagonal face is surrounded by three pentagons alternating with three hexagons. The figure is characterized by the presence of the following rotational elements of symmetry: 6 primary C_5 symmetry axes passing through opposite pentagonal faces, 10 C_3 symmetry axes passing through opposite hexagonal faces and 15 C_2 symmetry axes passing through the center of opposite hexagon-hexagon edges, see figure 1.2. Each rotational symmetry element is replicated into an improper one by composition with the inversion operation (with respect to the geometric center) for a total of 120 symmetry operations. C_{60} belongs to the icosahedral point group I_h and is the closest realization of a spherical molecule. In the real molecule the atoms are not disposed according to a *regular* icosahedron since the bonds in the pentagonal faces and in the hexagonal-hexagonal edges have different length, 1.46 Å (single bond) and 1.40 Å (double bond) respectively [6]. The geometric diameter is 7.1 Å but the molecule extends to 10.4 Å in consideration of the electronic shell.

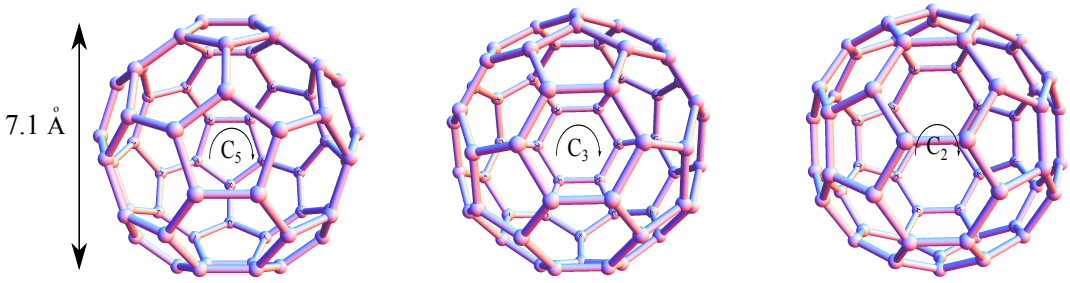

Figure 1.2: View of the icosahedral C_{60} molecule and its rotational symmetry elements: C_5 axes cross opposite pentagonal faces, C_3 axes cross opposite hexagonal faces, C_2 axes cross opposite edges.

In virtue of Van der Waals interactions C_{60} forms a molecular solid in normal conditions. At normal pressure the centers of the molecules are arranged on a face centered cubic (fcc) lattice with constant 14.17 Å corresponding to a nearest-neighbor center-to-center distance about 10 Å. The phase diagram of solid C_{60} is characterized by the existence of a transition at 260 K between a high-temperature fcc phase and a low-temperature simple cubic (sc) phase. Such transition corresponds to an abrupt change in the molecular reorientational dynamics while the arrangement of the cage centers remains unchanged [7, 8]. In the high-temperature phase molecules enjoy free uncorrelated rotational motion resembling identical spherical balls: the solid belongs to the space group $Fm\bar{3}m$ with four equivalent spherical C_{60} per unit cell (one vertex and three nearest face centers), see figure 1.3. Below 260 K the molecules exhibit orientational order: fullerenes on opposite faces get oriented in the same way leading to a simple cubic (sc) lattice $Pa\bar{3}$ with four non equivalent C_{60} per unit cell [9, 10]. Although not obvious a priori the inter-molecular potential has two configurational local minima separated by a potential barrier: a low-energy p orientation in which each electron-poor pentagonal face is directly opposed to one electron-rich hexagonal edge of the nearest

surrounding molecules and a high-energy *h* orientation in which hexagonal faces are adjacent to hexagonal double bonds of the nearest molecules [6]. In the low-temperature phase molecules perform thermal-activated jumps between the inequivalent *p* and *h* orientations and the corresponding 60 symmetrically equivalent orientations. At lower temperatures jumps among the inequivalent configurations are less frequent and a small fraction of molecules freezes in the less favorable *h* configuration leading to merohedral disorder. A third transition happens when the ratcheting motion among equivalent position gets frozen as well [11]. The exact temperatures at which this glassy transition is observed depends on the time response of the probe used; it is between 180 K and 100 K.

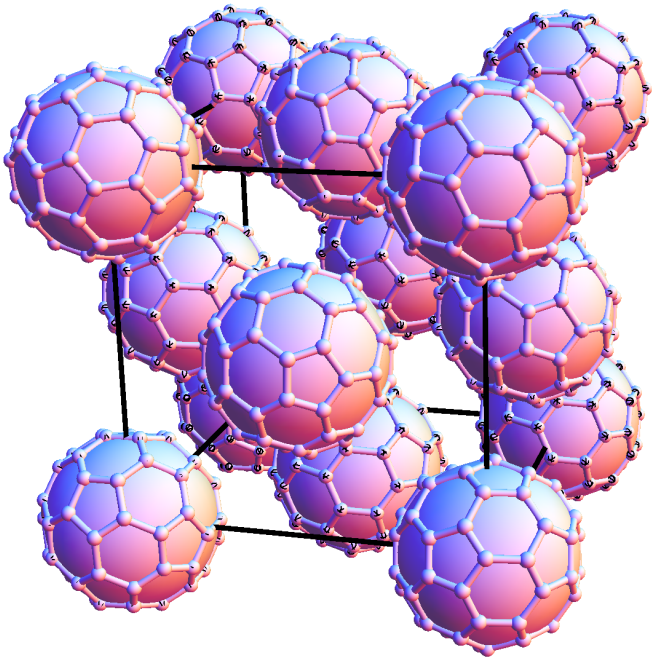

Figure 1.3: High-temperature face centered cubic crystal structure of solid C_{60} at $T >$ 260 K. Each C_{60} rotates freely and independently of the others behaving as a spherical ball. Vertices are equivalent to face centers and middle points of the edges are equivalent to the body center. All these sites have octahedral symmetry.

1.3 Endohedral hydrogen fullerene synthesis

The possibility of inserting small atoms or molecules in the hollow cavity of fullerenes has attracted the interest of the scientists soon after their recognition. The first endohedral fullerene complexes were metallo-fullerenes obtained by laser vaporization/arc vaporization of graphite rods impregnated with the metal[12, 13, 14]. Interesting examples are fullerene encapsulating clusters that would not be stable otherwise, such as

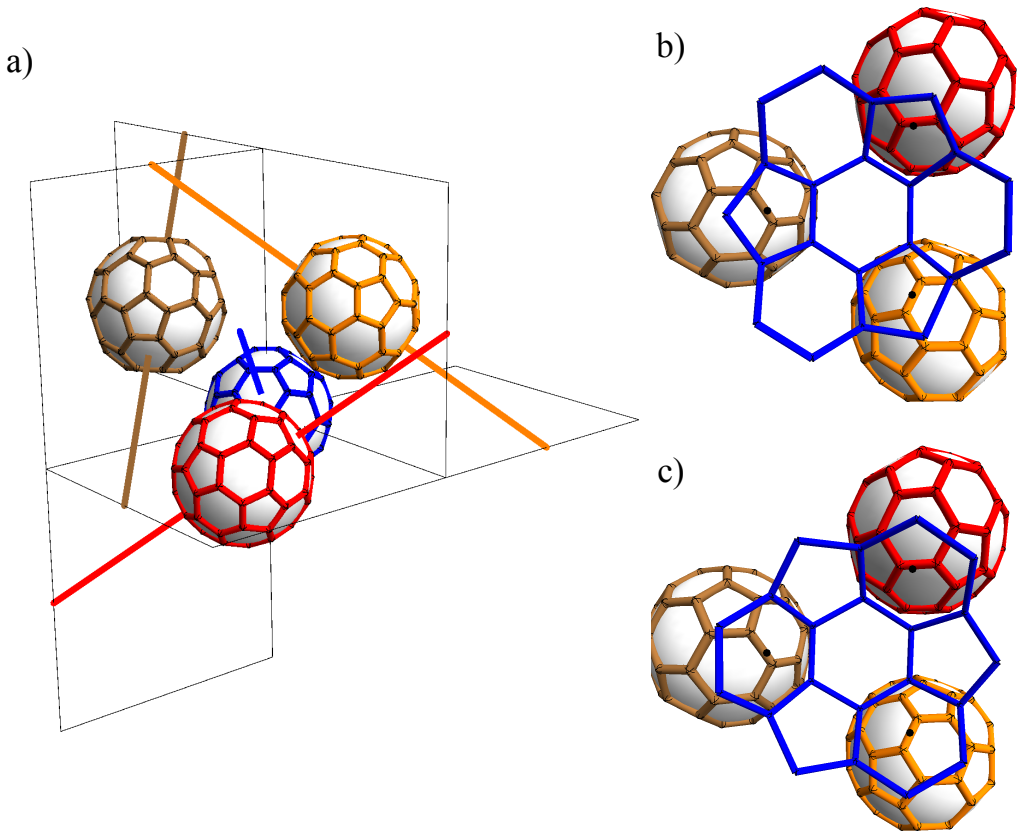

Figure 1.4: Low-temperature simple cubic crystal structure of solid C_{60} $T < 260$ K. In a) only four inequivalent C_{60} in the unit cell are shown. The C_3 axes of the molecules orient along the principal diagonal of the cubic structure as shown. The four molecules are rotated along this axes so to be in one of the two minimal energy configurations shown on the right: b) *p* configuration and c) *h* configuration have double bonds electron-rich edges opposite to pentagonal and hexagonal faces respectively.

trimetalnitride complexes inside C_{80} [15] and $C_2Sc_2C_{84}$ [16, 17] which is a remarkable example of a quantum gyroscope. Noble gas atoms were inserted by exposing fullerenes to high temperatures and pressures [18, 19, 20]. However difficulties remain in preparing and separating macroscopic amounts of pure complexes and only a small fraction of fullerenes (up to few percent) can be filled using such methods. A breakthrough in the field came when Komatsu and co-workers established a completely synthetic route, schematically represented in figure 1.5 for the encapsulation of H_2 in C_{60} [21, 22, 23]. Firstly a sufficiently large orifice is cut in the carbon structure through a series of controlled reactions. By applying high temperature and high pressure molecular hydrogen is then forced into the open cages (100% load) where it remains trapped once normal conditions are restored. Finally the hole is sewed up without any hydrogen escape by another series of chemical reactions. High performance liquid chromatography separates out the residual amount of empty fullerenes leaving 100% of the fullerenes filled. Using this *molecular surgery* procedure one hydrogen molecule can be enclosed in C_{60} and up to two molecules inside C_{70} [24]. All the samples of endohedral fullerenes

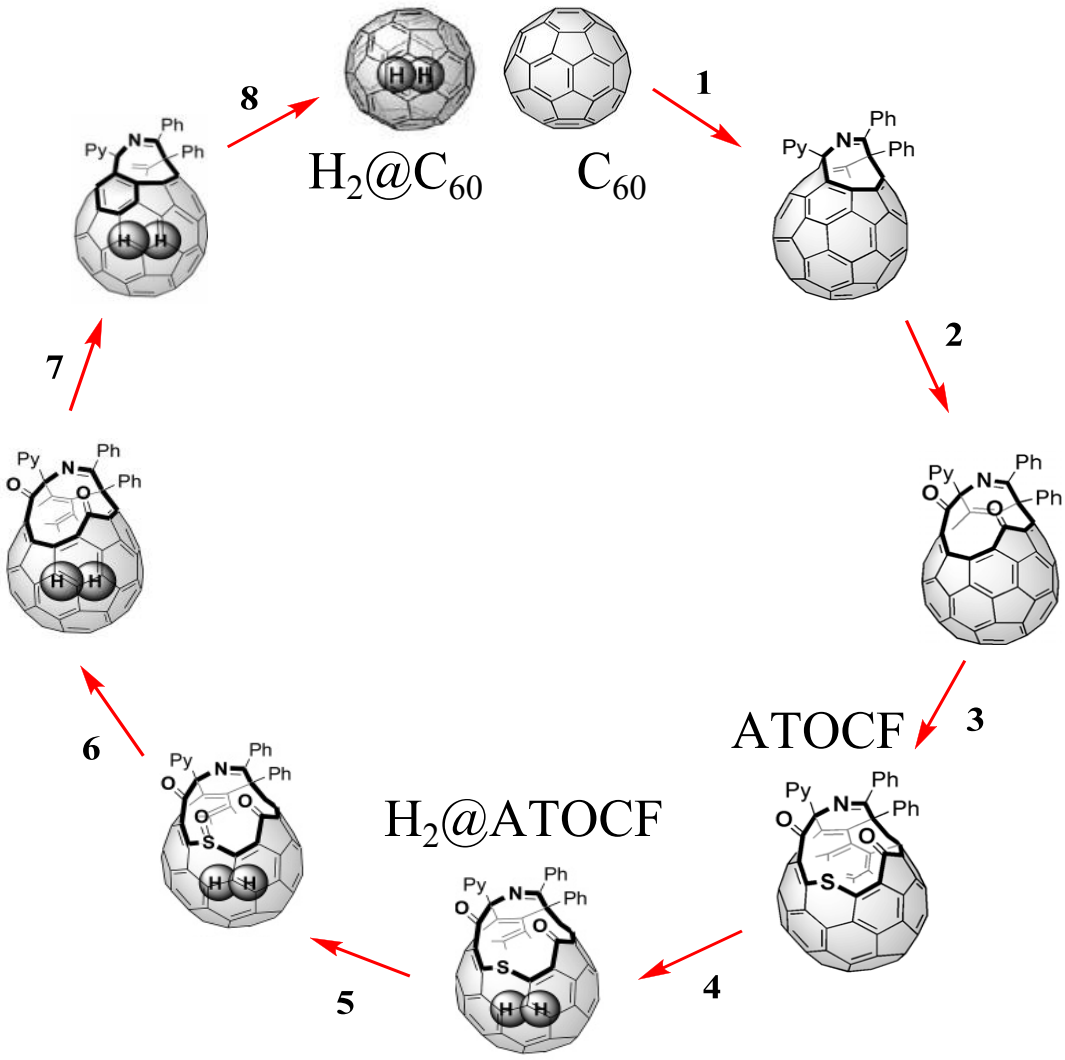

Figure 1.5: Molecular surgery multi-step reaction for the synthesis of $H_2@C_{60}$. In step 4 the empty azacyclic-thiacyclic-open-cage-fullerene (ATOCF) is filled with hydrogen to give $H_2@$ATOCF.

studied in this thesis were produced by the group of Komatsu and coworkers at Kioto University (Japan) or Turro and coworkers at Columbia University (USA) following the synthetic procedure described above.

1.4 Quantum dynamics of $H_2@C_{60}$

The availability of endohedral hydrogen fullerene complexes in relatively large amounts prompted their theoretical and experimental investigations. $H_2@C_{60}$ is a unique complex that can be compared to clathrates, molecules trapped in the interstices of a crystal lattice or molecules trapped in a carcerand. However, due to the rigidity, stability, symmetry, and simplicity of the carbon framework, it can be treated with a rigor far beyond these other cases. The dynamics of the endohedral molecule is essentially determined

by supra molecular non-covalent interactions with the carbon atoms of the cage. Early ab initio calculations suggested that hydrogen rotates freely inside C_{60} rather than sticking to the walls of the cage [1]. The small mass of hydrogen combined with the small available room inside the cavity lead to highly quantistic dynamics with large spacing between sparse energy levels. Indeed the translational motion associated with the molecular center of mass is quantized in $H_2@C_{60}$: the continuum of states typical of the free molecule splits into discrete translational levels. The walls of C_{60} act as a spring force recalling the molecule to the center of the cage and introduce couplings between the translational and the rotational motion. The coupled rotational-translational levels are organized following patterns that reflect the symmetry and the strength of the confining potential. The high symmetry of C_{60} allows considerable simplification of the theoretical analysis and facilitates the interpretation of spectroscopic data in terms of transitions between the quantized modes of the confined molecule. For $H_2@C_{60}$ the difference between icosahedral and spherical symmetry is not of relevance in most cases. The intuitive picture of $H_2@C_{60}$ as an unhindered vibrating quantum rotor trapped in a nearly harmonic spherical cage and subjected to translational-rotational coupling is definitively corroborated by several spectroscopic observations [25], part of which are discussed in this thesis.

1.5 Outline of the thesis

The thesis is organized as follows. In the first chapter the mathematical framework underlying the quantitative analysis of the quantum dynamics and spectroscopy of $H_2@C_{60}$ is introduced. The chapter is centered on spherical tensors, in particular bipolar spherical harmonics as a spherical basis to describe the angular motion of a confined diatomic molecule in a highly symmetric environment. The Wigner-Eckart theorem is used to derive matrix elements of spherical operators over such spherical basis. In the second chapter the Hamiltonian of $H_2@C_{60}$ is derived showing that in the spherical approximation the motion of the endohedral hydrogen is decoupled from the rotations of the cage. The spherical approximation is justified by the smallness of non spherical versus spherical terms in the multipole expansion of the confining potential. For any reasonable choice of the non-bonding carbon-hydrogen interaction the confining potential is given by a large harmonic isotropic term combined with small anharmonic and rotational-translational corrections. In each vibrational manifold the rotational-translational quantum dynamics of H_2, determined by an effective potential with parametric dependence on the vibrational quantum number, is described in the basis of an harmonic oscillator whose orbital motion is coupled to the rotation of the molecule. The third chapter contains the experimental infrared spectra of $H_2@C_{60}$ and their analysis. The confinement-induced electric dipole is discussed in term of symmetry rather than of fundamental physical mechanisms. When combined with the quantum dynamical model of $H_2@C_{60}$ this approach allows one to obtain a complete description of the infrared spectra. Low

temperature spectra provide the main input for the assignment process, allowing the determination of the vibrational frequency and rotational constants, translational excitation and translation-rotation couplings in the first excited vibrational state. The refinement of the model over the high temperature spectra allow the determination of the effective potential in the ground and first vibrational state. The agreement between the refined model and the experiments is satisfactory but some minor features remain to be addressed. In the fourth chapter the ^{1}H NMR spectroscopy of two samples of $H_2@C_{60}$, prepared in slightly different way, is reported. The low temperature lineshapes and spin-lattice relaxation times show significant but yet unexplained differences. The chapter contains a study of the lineshape and spin-lattice relaxations between 2 and 0.1 K. The fifth chapter provide the theoretical framework for the interpretation of the nuclear spin dynamics in the system. A conclusive chapter summarizes the results obtained in this work and contains perspectives for future studies.

Chapter 2

Mathematical tools

In this chapter I discuss some mathematical aspects related to the high symmetry encountered in the study of a diatomic molecule confined in the C_{60} cavity. For a free rotor in a spherical potential the angular part of the nuclear wave-function is given in terms of bipolar spherical harmonics which generalize the spherical harmonics to a set of two angular variables: in the specific case these are the polar angles of the center of mass and of the internuclear vector with respect to a given reference frame. The rank of the bipolar harmonics coincides with the total angular momentum which is a good quantum number for the eigenstates of the confined rotor wave-function. Bipolar spherical harmonics can be used not only to describe the quantum state of endohedral fullerenes but as basis to expand local operators such as the intermolecular potential between the fullerene cage and the hydrogen molecule. The Wigner-Eckart theorem reduces the evaluation of matrix elements of spherical operators over the spherical basis to the evaluation of Wigner j-symbols. The property of the Wigner symbols allows one to obtain selection rules for spherical operators straightforwardly.

The chapter is organized as follows. At first the basic properties and definitions of geometric rotations in three-dimensions, angular momentum operators, commutation rules, irreducible representations of the rotation group, Euler angles and Wigner matrices are recalled. The Wigner j-symbols, with emphasis on the 3-j symbols, are then introduced in connection with the topic of composition of angular momenta. Spherical tensor operators are defined and the Wigner-Eckart theorem for simple and composite system is discussed first generally and then for the specific case of operators associated to spherical and bipolar spherical harmonics. All these topics fall within the wider field of the quantum theory of angular momentum. The relationships reported here form the mathematical background for the description of the enodhedral hydrogen quantum dynamics and the quantitative analysis of the low and high temperature infrared spectroscopy of $H_2@C_{60}$, which is the topic of the next two chapters.

2.1 Rotations in three dimensions

A rotation in the three-dimensional space is defined by a unit vector, $\boldsymbol{n}$, which determines the axis about which the rotation is performed, and the rotation angle Θ: $\hat{R}_{\boldsymbol{n}}(\Theta)$. The geometric effect of a rotation over a point is to move it through an angle Θ over the circle located in the plane perpendicular to $\boldsymbol{n}$. The sense of the rotation is clockwise for a positive Θ when looked along the direction defined by $\boldsymbol{n}$ and anticlockwise for negative Θ. This convention is called the 'right-hand' convention and it will be used throughout all this work. The set of rotations through axes which all have one point O in common is a non commutative group:

$$\hat{R}_{\boldsymbol{n}_1}(\Theta_1)\,\hat{R}_{\boldsymbol{n}_2}(\Theta_2) \neq \hat{R}_{\boldsymbol{n}_2}(\Theta_2)\,\hat{R}_{\boldsymbol{n}_1}(\Theta_1). \tag{2.1}$$

A rotation with $\Theta = 0$ along any $\boldsymbol{n}$ is the identity operation $\mathbb{1}$, since it does not produce any net transformation. The inverse of a rotation is another rotation defined as

$$\left[\hat{R}_{\boldsymbol{n}}(\Theta)\right]^{-1} \overset{\text{def}}{=} \hat{R}_{-\boldsymbol{n}}(\Theta) = \hat{R}_{\boldsymbol{n}}(-\Theta)\,. \tag{2.2}$$

It is possible to prove that in a system of Cartesian orthogonal coordinates $OXYZ$

$$\hat{R}_{\boldsymbol{n}}(\Theta) = \mathrm{e}^{-\mathrm{i}\Theta\hat{J}_{\boldsymbol{n}}} \tag{2.3}$$

with $\hat{J}_{\boldsymbol{n}} = \boldsymbol{n}_X\hat{J}_X + \boldsymbol{n}_Y\hat{J}_Y + \boldsymbol{n}_Z\hat{J}_Z$, $\{\boldsymbol{n}_X, \boldsymbol{n}_Y, \boldsymbol{n}_Z\}$ and $\left\{\hat{J}_X, \hat{J}_Y, \hat{J}_Z\right\}$ being the Cartesian components of $\boldsymbol{n}$ and of the angular momentum operator $\hat{\mathbf{J}}$, respectively. $\left\{\hat{J}_X, \hat{J}_Y, \hat{J}_Z\right\}$ are the generators of the rotation group since any element of the group can be obtained by exponentiation, equation (2.3). Geometrical arguments show that the commutator between infinitesimal rotations around orthogonal axes satisfy [26]

$$\left[\hat{R}_{\boldsymbol{X}}(\delta\Theta)\,, \hat{R}_{\boldsymbol{Y}}(\delta\Theta)\right] \overset{\text{def}}{=} \hat{R}_{\boldsymbol{X}}(\delta\Theta)\,\hat{R}_{\boldsymbol{Y}}(\delta\Theta) - \hat{R}_{\boldsymbol{Y}}(\delta\Theta)\,\hat{R}_{\boldsymbol{X}}(\delta\Theta) = \hat{R}_{\boldsymbol{Z}}(\delta\Theta) \tag{2.4}$$

at first order in $\delta\Theta$, which implies

$$\left[\hat{J}_X, \hat{J}_Y\right] = \hat{J}_X\hat{J}_Y - \hat{J}_Y\hat{J}_X = \mathrm{i}\hat{J}_Z. \tag{2.5}$$

Applying the argument above cyclically in $\{\boldsymbol{X}, \boldsymbol{Y}, \boldsymbol{Z}\}$, the commutator of the angular momentum components follows

$$\left[\hat{J}_i, \hat{J}_j\right] = \varepsilon_{ijk}\hat{J}_k \qquad i = X, Y, Z \tag{2.6}$$

where the Levi-Civita symbol ε_{ijk} is defined as:

$$\varepsilon_{ijk} = \begin{cases} 1 & \text{if } ijk \text{ is an even permutation of } XYZ \\ 0 & \text{if } ijk \text{ contains any two equal indices} \\ -1 & \text{if } ijk \text{ is an odd permutation of } XYZ \end{cases} \tag{2.7}$$

Equation (2.6) *defines* angular momentum operators. The set of commutation rules

$$\left[\hat{J}^2, \hat{J}_i\right] = 0 \qquad i = X, Y, Z, \tag{2.8a}$$
$$\left[\hat{J}_Z, \hat{J}_\pm\right] = \pm\hat{J}_\pm, \tag{2.8b}$$
$$\left[\hat{J}_+, \hat{J}_-\right] = 2\hat{J}_Z \tag{2.8c}$$

follows from equation (2.6), with

$$\hat{J}^2 = \hat{J}_X^2 + \hat{J}_Y^2 + \hat{J}_Z^2. \tag{2.9a}$$
$$\hat{J}_\pm = \hat{J}_X \pm \mathrm{i}\hat{J}_Y. \tag{2.9b}$$

The square of the angular momentum $\hat{J}^2$ commutes with all the angular momentum components. Ladder operators $\hat{J}_\pm$ are used to find explicit representations of angular momentum operators.

2.1.1 Representation of angular momentum operators and rotations

It is well known that the finite dimensional representations of the rotations operator have dimensions $2j + 1$ with j integer or half integer. In other words for any given j there is an orthonormal basis, $|j, m_j\rangle$ in ket notation, for which

$$\hat{J}^2|j, m_j\rangle = j(j+1)|j, m_j\rangle \tag{2.10a}$$
$$\hat{J}_Z|j, m_j\rangle = m_j|j, m_j\rangle \tag{2.10b}$$
$$\hat{J}_\pm|j, m_j\rangle = \left[j(j+1) - m(m \pm 1)\right]^{1/2}|j, m_j \pm 1\rangle \tag{2.10c}$$

with m_j integers or half integers according to the value of j and $\left|m_j\right| \leq j$. In particular $\hat{J}_+|j, j\rangle = 0$ and $\hat{J}_-|j, -j\rangle = 0$. j and m_j are referred as the square and the Z-projection values of the angular momentum respectively. The argument is based on the commutation relationships Equations (2.10a), (2.10b) and (2.10c) and detailed discussions can be found in any textbook on angular momentum theory [27, 28].

Euler angles

Any rotation can be described by a set of three angles: the most obvious being the rotation angle Θ and the two polar angles $\{\theta, \phi\}$ defining the rotation axis $\boldsymbol{n}$ in a given

reference frame $OXYZ$. A rotation can be 'decomposed' into three consecutive rotations along two orthogonal axis of the reference frame $OXYZ$ obtaining the same geometrical effect. For example one can choose the Z and the Y direction (Z-Y-Z convention) so that:

$$\hat{R}_{\boldsymbol{n}}(\Theta) = \hat{R}_{\boldsymbol{Z}}(\alpha)\,\hat{R}_{\boldsymbol{Y}}(\beta)\,\hat{R}_{\boldsymbol{Z}}(\gamma). \tag{2.11}$$

The sequence $\{\alpha, \beta, \gamma\}$ is a set of 'Euler angles'. The explicit relationships among the Euler angles $\{\alpha, \beta, \gamma\}$ and the polar parameters $\{\omega, \theta, \phi\}$ can be found in [29].

Any rigid frame superimposed to the orthogonal axes of the reference frame is transported into a frame $OX'Y'Z'$ by the three consecutive rotations according to equation (2.11): a first rotations of an angle γ around the Z axis, a second rotations of angle β around the Y axis and a third rotation of angle α around the Z axis. For any $\beta \neq 0$ the line of nodes N is the intersection of the OXY and $OX'Y'$ planes positive oriented according to positive Y axis. The same transformation can be accomplished by a set of three rotations in reversed order [30]:

- first rotate through α about the fixed axis Z, bringing the Y axis on the line of nodes;
- then rotate through β about the line of nodes N, bringing the Z axis on the Z' axis;
- finally rotate through γ about the Z' axis to bring in position the X' and Y' axes.

This second definiton is easier to follow geometrically and gives a clearer interpretation of the Euler angles, see figure 2.1: α is the angle between Y and the line of nodes, β is the angle among Z and Z' and γ is the angle between the line of nodes and Y'. Note that if $\beta = 0$ only $\alpha + \gamma$ is defined and if $\beta = \pi$ only $\alpha - \gamma$ is defined. In the former case Z and Z' are coincident and $\alpha + \gamma$ represents the angle between Y and Y' while in the latter case Z and Z' are opposite and the angle between Y and Y' is given $\alpha - \gamma$.

Rotation matrices

Euler angles may be used to form the $(2j+1)$-dimensional matrix representations of rotations in the $|j, m_j\rangle$ basis:

$$D^{j}_{m'_j,m_j}(\alpha,\beta,\gamma) = \langle j, m'_j|\hat{R}_{\boldsymbol{Z}}(\alpha)\,\hat{R}_{\boldsymbol{Y}}(\beta)\,\hat{R}_{\boldsymbol{Z}}(\gamma)|j, m_j\rangle = \mathrm{e}^{-\mathrm{i}\left(m'_j\alpha + m_j\gamma\right)} d^{j}_{m'_j,m_j}(\beta) \tag{2.12a}$$

$$d^{j}_{m'_j,m_j}(\beta) = \langle j, m'_j|\hat{R}_{\boldsymbol{Y}}(\beta)|j, m_j\rangle \tag{2.12b}$$

$D^{j}_{m'_j,m_j}$ and $d^{j}_{m'_j,m_j}$ are referred as the Wigner and the 'reduced' Wigner matrices, respectively. The general formula to evaluate the reduced Wigner matrices elements $d^{j}_{m'_j,m_j}$ in function of the Euler angles $\{\alpha, \beta, \gamma\}$ is given in [29], along with explicit matrix forms for low j-values.

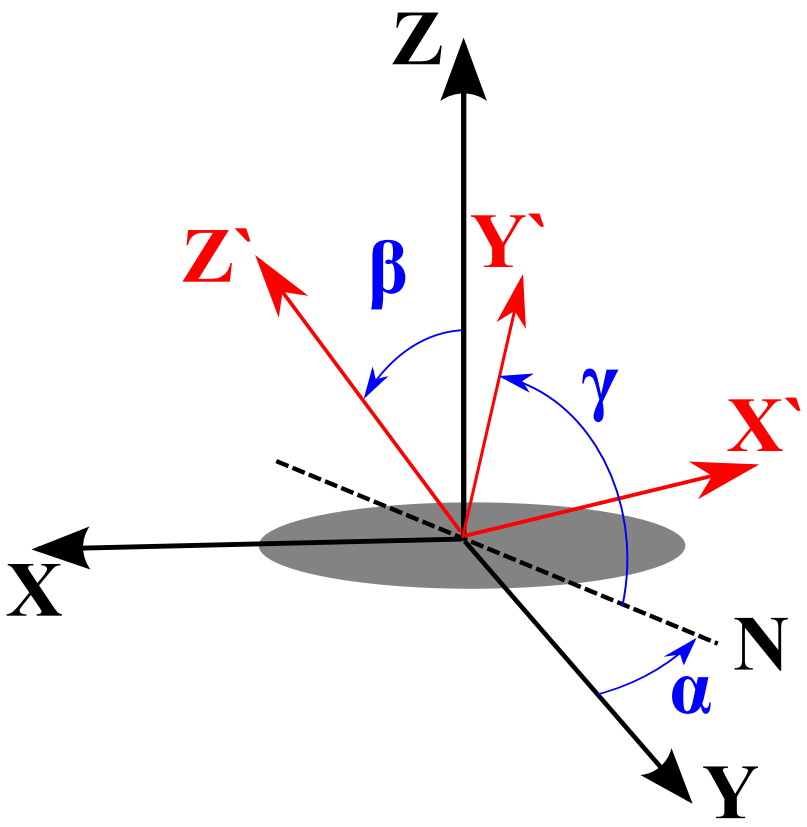

Figure 2.1: Euler angles in the Z-Y-Z convention. The rigid orthogonal frame $OXYZ$ is transported onto the orthogonal rigid frame $OX'Y'Z'$ by a set of three consecutive rotations. The dotted line represents the intersection between the XY plane and the $X'Y'$ plane (line of nodes).

2.2 Addition of angular momenta

The coupling of angular momenta is a central topic in quantum mechanics. For a single particle the total angular momentum $\hat{\boldsymbol{J}}$ is the sum of the orbital angular momentum $\hat{\boldsymbol{L}}$ and of the spin $\hat{\boldsymbol{I}}$: $\hat{\boldsymbol{J}} = \hat{\boldsymbol{L}} + \hat{\boldsymbol{I}}$. For two particles the total angular momentum $\hat{\boldsymbol{J}}$ is the sum of the angular momenta, $\hat{\mathbf{J}}_1$ and $\hat{\mathbf{J}}_2$, of each particle: $\hat{\boldsymbol{J}} = \hat{\mathbf{J}}_1 + \hat{\mathbf{J}}_2$. In general the total angular momentum of a system is the 'sum' of the angular momenta of the constituents. The sum of two (commuting) angular momenta is an angular momentum because the components of $\hat{\boldsymbol{J}}$ satisfy equation (2.6). The finite dimensional matrix representation of the sum of two angular momenta has dimension $2j+1$ with j integer or half integer. For given values of the angular momenta, j_1 and j_2, the angular momentum j can assume only certain values according to the triangular inequality [26]:

$$|j_1 - j_2| \leq j \leq j_1 + j_2. \tag{2.13}$$

In other words the $(2j_1 + 1) \times (2j_2 + 1)$-dimensional representation can be reduced in $2j+1-$dimensional blocks with $j = j_1+j_2, \ldots, |j_1-j_2|$ each with basis $|j, m_j; j_1, j_2\rangle$. The

Clebsch-Gordan coefficients are the projection of the uncoupled basis over the coupled one:

$$C^{j\,m}_{j_1\,m_1,j_2\,m_2} = \langle j, m; j_1 j_2 | j_1, m_1; j_2, m_2 \rangle. \tag{2.14}$$

Following the phase convention of Condon and Shortley [29], the Clebsch-Gordan coefficients are real. For fixed j_1 and j_2 they represent the entries of the unitary transformations linking the coupled basis and the uncoupled one:

$$|j, m; j_1, j_2\rangle = \sum_{m_1,m_2} C^{j\,m}_{j_1\,m_1,j_2\,m_2} |j_1, m_1; j_2, m_2\rangle, \tag{2.15a}$$

$$|j_1, m_1; j_2, m_2\rangle = \sum_{j,m_j} C^{j\,m}_{j_1\,m_1,j_2\,m_2} |j, m; j_1, j_2\rangle. \tag{2.15b}$$

2.2.1 Wigner symbols

The Clebsch-Gordan coefficients are the simplest example of coupling coefficients. More complex coefficients are obtained on coupling three or more angular momenta. In such case there is more than one state $|j, m\rangle$ with given values of j and m. The order in which angular momenta are coupled in pairs in successive steps is relevant and specific notation is used to stress the use of the particular recoupling scheme s. Wigner $3n$-j coefficients relate the total angular momentum eigenstates when coupling $n + 1$ angular moments according to different schemes. All the recoupling coefficients can be written in terms of Clebsch-Gordan coefficients or 3-j symbols, see below. The various angular momentum values j_i and projection m_i enter in the Clebsch-Gordan coefficients in an asymmetric way. A more symmetric symbol is the 3-j Wigner symbol:

$$\begin{pmatrix} j_1 & j_2 & j_3 \\ m_1 & m_2 & m_3 \end{pmatrix} = (-1)^{j_3+m_3+2j_1} \frac{1}{\sqrt{2j_3+1}} C^{j_3\,m_3}_{j_1\,-m_1,j_2\,-m_2} \tag{2.16}$$

$$C^{j_3\,m_3}_{j_1\,m_1,j_2\,m_2} = (-1)^{j_1-j_2+m_3} \sqrt{2j_3+1} \begin{pmatrix} j_1 & j_2 & j_3 \\ m_1 & m_2 & -m_3 \end{pmatrix} \tag{2.17}$$

Some properties of the 3-j symbols are [29]:

- the 3-j symbol in equation (2.16) is zero if the arguments in the first row j_1, j_2, j_3 does not form a triangular triad satisfying equation (2.13) or if $m_1 + m_2 + m_3 \neq 0$;
- the value of a 3-j symbol does not change by an even permutation of its columns but is multiplied by a factor $(-1)^{j_1+j_2+j_3}$ by an odd permutation of its columns. For example

$$\begin{pmatrix} j_1 & j_2 & j_3 \\ m_1 & m_2 & m_3 \end{pmatrix} = \begin{pmatrix} j_3 & j_1 & j_2 \\ m_3 & m_1 & m_2 \end{pmatrix} = (-1)^{j_1+j_2+j_3} \begin{pmatrix} j_1 & j_3 & j_2 \\ m_1 & m_3 & m_2 \end{pmatrix}; \tag{2.18}$$

- the value of a 3-j symbol is multiplied by a factor $(-1)^{j_1+j_2+j_3}$ if the sign of all the

momentum projections is changed:

$$\begin{pmatrix} j_1 & j_2 & j_3 \\ m_1 & m_2 & m_3 \end{pmatrix} = (-1)^{j_1+j_2+j_3} \begin{pmatrix} j_1 & j_2 & j_3 \\ -m_1 & -m_2 & -m_3 \end{pmatrix}. \tag{2.19}$$

In the following only 3-j, 6-j and 9-j symbols will be used. The 6-j symbols are defined by

$$\begin{aligned} \langle j_1 j_2 (j_{12}), j_3; jm | j_1, j_2 j_3 (j_{23}), j' m' \rangle = \delta_{j,j'} \delta_{m,m'} (-1)^{j_1+j_2+j_3+j} \\ \times \sqrt{(2j_{12}+1)(2j_{23}+1)} \begin{Bmatrix} j_1 & j_2 & j_{12} \\ j_3 & j & j_{23} \end{Bmatrix} \end{aligned} \tag{2.20}$$

and their definition in term of the Clebsch-Gordan coefficients is given by

$$\begin{Bmatrix} a & b & c \\ d & e & f \end{Bmatrix} = (-1)^{d+e+f+\delta+\epsilon+\phi} \sum_{\substack{\alpha,\beta,\gamma \\ \delta,\epsilon,\phi}} \begin{pmatrix} a & b & c \\ \alpha & \beta & \gamma \end{pmatrix} \begin{pmatrix} a & e & f \\ \alpha & \epsilon & -\phi \end{pmatrix} \begin{pmatrix} d & b & f \\ -\delta & \beta & \phi \end{pmatrix} \begin{pmatrix} d & e & c \\ \delta & -\epsilon & \gamma \end{pmatrix} \tag{2.21}$$

where only three summation indices are independent because of the property of the 3-j symbols.[29] The 9-j symbols are defined by

$$\begin{aligned} &\langle j_1 j_2 (j_{12}), j_3 j_4 (j_{34}), jm | j_1 j_3 (j_{13}), j_2 j_4 (j_{24}), j' m' \rangle = \\ &\delta_{j,j'} \delta_{m,m'} \left[(2j_{12}+1)(2j_{13}+1)(2j_{34}+1)(2j_{34}+1) \right]^{1/2} \begin{Bmatrix} j_1 & j_2 & j_{12} \\ j_3 & j_4 & j_{34} \\ j_{13} & j_{24} & j \end{Bmatrix} \end{aligned} \tag{2.22}$$

and their definition in terms of the Clebsch-Gordan coefficients is given by

$$\begin{Bmatrix} a & b & c \\ d & e & f \\ g & h & j \end{Bmatrix} = \sum_{\substack{\alpha,\beta,\gamma \\ \delta,\varepsilon,\phi \\ \eta,\mu,\nu}} \begin{pmatrix} a & b & c \\ \alpha & \beta & \gamma \end{pmatrix} \begin{pmatrix} d & e & f \\ \delta & \epsilon & \phi \end{pmatrix} \begin{pmatrix} g & h & j \\ \eta & \mu & \nu \end{pmatrix} \begin{pmatrix} a & d & g \\ \alpha & \delta & \eta \end{pmatrix} \begin{pmatrix} b & e & h \\ \beta & \epsilon & \mu \end{pmatrix} \begin{pmatrix} c & f & j \\ \gamma & \phi & \nu \end{pmatrix} \tag{2.23}$$

where only five summation indices are independent because of the first property of the 3-j symbols [29]. A more efficient formula for the computation of 9-j symbols makes use of a single sum over 6-j symbols [31]:

$$\begin{Bmatrix} a & b & c \\ d & e & f \\ g & h & j \end{Bmatrix} = \sum_x (-1)^{2x} (2x+1) \begin{Bmatrix} a & d & g \\ h & j & x \end{Bmatrix} \begin{Bmatrix} b & e & h \\ d & x & f \end{Bmatrix} \begin{Bmatrix} c & f & j \\ x & a & b \end{Bmatrix} \tag{2.24}$$

where x takes integer values from 0 to the greatest integer compatibile with non-null 6-j symbol.

Analytical formulae and tables of 3-j, 6-j, 9-j symbols and Clebsch-Gordan coefficients can be found in [29]. Computational software, such as Mathematica [32], provide built-in routines for the evaluation of 3-j and 6-j symbols while 9-j symbols have been computed by using equation (2.24) .

2.3 Spherical tensor operators

Classically the effect of a rotation over a physical system can be defined in two steps

- first rotate all the coordinates (position and velocities) of the particle composing system;
- then recalculate all the physical observables in the new configuration.

The physical properties that remain unchanged in the initial and rotated configuration are scalars or invariants (under rotation). Other physical quantities change whenever the system is rotated: for example the electric dipole moment associated with a charge distribution changes its direction if the system is rotated (in the same way as vector does). Higher multipole moments transform under rotation in a more complicated way. The way in which a physical quantity transforms under the effect of a rotation is encoded in its tensorial rank, a concept clarified below referring directly to the quantum mechanical case.

The use of Wigner matrices allows one to describe algebraically the *action* of a rotation through equation (2.11) and equation (2.12a) on a quantum state:

$$\hat{R}_{\boldsymbol{n}}(\Theta)\left[|j,m\rangle\right] = \hat{R}(\alpha,\beta,\gamma)\left[|j,m\rangle\right] = \sum_{m'} |j,m'\rangle D^{j}_{m',m}(\alpha,\beta,\gamma) \tag{2.25}$$

The notation $\hat{R}_{\boldsymbol{n}}(\Theta)\left[|j,m\rangle\right]$ emphasizes that the rotation is acting on the ket $|j,m\rangle$. By extension, an irreducible spherical tensor of (integer) rank k is by definition a set of $2k+1$ functions, labelled by an index $q = -k,\ldots,k$, which transforms according to equation (2.25):

$$\hat{R}_{\boldsymbol{n}}(\Theta)\left[T^{k}_{q}(A)\right] = \hat{R}(\alpha,\beta,\gamma)\left[T^{k}_{q}(A)\right] = \sum_{q'} T^{k}_{q'}(A)\, D^{k}_{q',q}(\alpha,\beta,\gamma)\,. \tag{2.26}$$

where A denotes the set of variables on which the tensor depends. $T^{k}_{q}(A)$, $q = -k, -k+1,\ldots,k$, are the components of the spherical tensor.

In quantum mechanics physical observables are represented by operators. The action of a rotation on an operator $\hat{O}$ is obtained by sandwiching it between the rotation

operator, equation (2.3), and its inverse:

$$\hat{\hat{R}}_{\boldsymbol{n}}(\Theta)\left[\hat{O}\right] \stackrel{\text{def}}{=} \mathrm{e}^{-\mathrm{i}\Theta\hat{J}_{\boldsymbol{n}}}\hat{O}\,\mathrm{e}^{\mathrm{i}\Theta\hat{J}_{\boldsymbol{n}}}. \tag{2.27}$$

Here $\hat{\mathbf{J}}$ is the angular momentum of the system. In other words in the space of linear operators a rotation is represented by a *superoperator* $\hat{\hat{R}}_{\boldsymbol{n}}(\Theta)$.

An irreducible spherical tensor operator (ISTO) is by definition a set of $2k+1$ operators, labelled by an index $q = -k, -k+1, \ldots, k$, which transforms according to equation (2.26):

$$\hat{\hat{R}}_{\boldsymbol{n}}(\Theta)\left[T^k_q\left(\hat{O}\right)\right] = \hat{R}(\alpha,\beta,\gamma)\left[T^k_q\left(\hat{O}\right)\right] = \sum_{q'} T^k_{q'}\left(\hat{O}\right) D^j_{q',q}(\alpha,\beta,\gamma)\,. \tag{2.28}$$

An equivalent definition of an ISTO is [26]

$$\left[\hat{J}_Z, T^k_q\left(\hat{O}\right)\right] = qT^k_q\left(\hat{O}\right) \tag{2.29a}$$

$$\left[\hat{J}_\pm, T^k_q\left(\hat{O}\right)\right] = \left[k(k+1) - p(p\pm 1)\right]^{1/2} T^k_{q-1}\left(\hat{O}\right) \tag{2.29b}$$

2.3.1 ISTO for single quantum system

An example of a spherical tensor of rank 1 is given by the angular momentum $\hat{\mathbf{J}}$ with components organized in the following way:

$$T^1_0\left(\hat{\mathbf{J}}\right) = \hat{J}_Z \tag{2.30a}$$

$$T^1_{\pm 1}\left(\hat{\mathbf{J}}\right) = \mp\frac{1}{\sqrt{2}}\left(\hat{J}_X \pm \mathrm{i}\hat{J}_Y\right) \tag{2.30b}$$

Spherical tensor operators of higher rank can be built by coupling $\hat{\mathbf{J}}$ recursively [26]:

$$T^k_q\left(\hat{\mathbf{J}}\right) \stackrel{\text{def}}{=} \sum_{q_1=-1}^{1} C^{k\,q}_{k-1\,q-q_1,1\,q_1} T^{k-1}_{q-q_1}\left(\hat{\mathbf{J}}\right) T^1_{q_1}\left(\hat{\mathbf{J}}\right). \tag{2.31}$$

For example the rank two spherical tensor is

$$\begin{aligned}
T^2_{\pm 2}\left(\hat{\mathbf{J}}\right) &= T^1_{\pm 1}\left(\hat{\mathbf{J}}\right) T^1_{\pm 1}\left(\hat{\mathbf{J}}\right),\\
T^2_{\pm 1}\left(\hat{\mathbf{J}}\right) &= \frac{1}{\sqrt{2}}\left[T^1_{\pm 1}\left(\hat{\mathbf{J}}\right) T^1_0\left(\hat{\mathbf{J}}\right) + T^1_0\left(\hat{\mathbf{J}}\right) T^1_{\pm 1}\left(\hat{\mathbf{J}}\right)\right],\\
T^2_0\left(\hat{\mathbf{J}}\right) &= \frac{1}{\sqrt{6}}\left[T^1_1\left(\hat{\mathbf{J}}\right) T^1_{-1}\left(\hat{\mathbf{J}}\right) + 2T^1_0\left(\hat{\mathbf{J}}\right) T^1_0\left(\hat{\mathbf{J}}\right) + T^1_{-1}\left(\hat{\mathbf{J}}\right) T^1_1\left(\hat{\mathbf{J}}\right)\right].
\end{aligned} \tag{2.32}$$

The adjoint of a spherical operator is found easily:

$$T^k_q\left(\hat{\mathbf{J}}\right)^\dagger = (-1)^q T^k_{-q}\left(\hat{\mathbf{J}}\right). \tag{2.33}$$

The spherical tensor operators defined above are important for quantum systems with finite (integer or half integer) value I of total angular momentum $\boldsymbol{I}$. In this class the most notable example is given by nuclear spins. The maximum spherical rank supported is $k = 2I + 1$ and the spherical operators $T^k_q(\boldsymbol{I})$ form a basis of independent (orthogonal) operators. The norm of a spherical operator, in the trace sense, depends on I as follows

$$\left|T^k_q(\boldsymbol{I})\right| \stackrel{\text{def}}{=} \mathrm{Tr}_{M_I}\left[T^k_q(\boldsymbol{I})^\dagger\, T^k_q(\boldsymbol{I})\right] = \frac{k!}{2^{\frac{k}{2}}}\sqrt{\binom{2I+k+1}{2k+1}} \tag{2.34}$$

where the round parentheses contain a binomial coefficient. Spherical tensors can be built from any vectorial quantity or operator $\hat{\boldsymbol{O}}$=$\{\hat{O}_X, \hat{O}_Y, \hat{O}_Z\}$, replacing $\hat{\mathbf{J}}$ with $\hat{\boldsymbol{O}}$ in equations (2.30a) and (2.30b).

2.3.2 ISTO for composite quantum system

In a composite quantum system spherical tensor operators can be built in a similar way by multiplying two spherical tensors by the use of Clebsch-Gordan coefficients:

$$\left[T^{k_1}\left(\hat{O}_1\right) \otimes T^{k_2}\left(\hat{O}_2\right)\right]^k_q \stackrel{\text{def}}{=} \sum_{q_1=-k_1}^{k_1} C^{k\,q}_{k_1\,q_1,k_2\,-q-q_1}\, T^{k_1}_{q_1}\left(\hat{O}_1\right) \otimes T^{k_2}_{q_2}\left(\hat{O}_2\right). \tag{2.35}$$

$\otimes$ is the direct product of operators. As in angular momenta addition, the ranks which enter in the composite spherical tensor satisfy the triangular inequality: $|k_1 - k_2| \leq k \leq k_1 + k_2$. In particular the tensor scalar product (invariant under rotation) is defined as

$$T^k\left(\hat{O}_1\right) \cdot T^k\left(\hat{O}_2\right) \stackrel{\text{def}}{=} \sum_{q=-k}^{k} (-1)^q T^k_q\left(\hat{O}_1\right) T^k_{-q}\left(\hat{O}_2\right) = (-1)^k \sqrt{2k+1}\left[T^k\left(\hat{O}_1\right) \otimes T^k\left(\hat{O}_1\right)\right]^0_0 \tag{2.36}$$

having used $C^{0\,0}_{k\,q_1,k\,q_2} = \delta_{q_1,-q_2}(-1)^{k-q_1}/\sqrt{2k+1}$ in equation (2.35). More than one operator can be obtained for a given rank k and component q when composing more than two spherical operators and the coupling scheme s should also be specified [33].

2.3.3 Wigner-Eckart theorem

Spherical tensors allows one to to exploit the symmetry of a quantum system under rotation by the use of Wigner-Eckart theorem [27]. For a quantum system with basis

$|\tau, j, m_j\rangle$ the matrix elements of a spherical operators $T^k_p(A)$ can be obtained by:

$$\langle \tau, j, m | T^k_q\left(\hat{O}\right) | \tau', j', m' \rangle = (-1)^{j-m} \begin{pmatrix} j & k & j' \\ -m & q & m'_j \end{pmatrix} \langle \tau, j \| T^k\left(\hat{O}\right) \| \tau', j' \rangle. \tag{2.37}$$

The label τ denotes the set of quantum numbers, apart from the angular momentum ones, that are needed to completely define a quantum state of the system. The reduced matrix element $\langle \tau, j \| T^k\left(\hat{O}\right) \| \tau', j' \rangle$ is independent of the angular momentum components m, m', q. The factor $(-1)^{j-m}$ comes from the relative phase between the bra $\langle \tau, j, m|$ and the ket $|\tau, j, m\rangle$. The power of the Wigner-Eckart theorem stems from the fact that the evaluation of $(2j+1)(2k+1)(2j'+1)$ matrix elements is essentially reduced to the evaluation of an algebraic factor, the 3-j symbol, and one quantity, the reduced matrix element, which retains all the physical content of the matrix elements. A useful consequence of the Wigner-Eckart theorem is the 'replacement' theorem, which relates the matrix elements between two spherical operators with the same rank:

$$\langle \tau, j, m | T^k_q\left(\hat{O}_1\right) | \tau', j', m' \rangle = \frac{\langle \tau, j \| T^k\left(\hat{O}_1\right) \| \tau', j' \rangle}{\langle \tau, j \| T^k\left(\hat{O}_2\right) \| \tau', j' \rangle} \langle \tau, j, m | T^k_q\left(\hat{O}_2\right) | \tau', j', m' \rangle. \tag{2.38}$$

In the operator version of the replacement theorem, the operator $T^k_q\left(\hat{\boldsymbol{O}}\right)$ is replaced by the corresponding angular momentum tensor operator $T^k_q\left(\hat{\mathbf{J}}\right)$:

$$T^k_q\left(\hat{\boldsymbol{O}}\right)\Big|_{\substack{j=j' \\ \tau=\tau'}} = \frac{\langle \tau, j \| T^k\left(\hat{\boldsymbol{O}}\right) \| \tau', j \rangle}{\langle j \| T^k\left(\hat{\mathbf{J}}\right) \| j' \rangle} T^k_q\left(\hat{\mathbf{J}}\right) \tag{2.39}$$

in a subspace with $\tau = \tau'$ and $j = j'$ or when the mixing of states with different j can be neglected. The reduced matrix element of the rank k angular momentum spherical tensor operator in equation (2.31) is proportional to the norm of the operator [34]:

$$\langle j \| T^k\left(\hat{\mathbf{J}}\right) \| j' \rangle = \delta_{j,j'} \sqrt{(2k+1)} \left| T^k_q(\boldsymbol{I}) \right| = \delta_{j,j'} \frac{k!}{2^{\frac{k}{2}}} \sqrt{(2k+1)\begin{pmatrix} 2I+k+1 \\ 2k+1 \end{pmatrix}}. \tag{2.40}$$

Matrix elements for composite angular momentum operators

The Wigner-Eckart theorem can be used to evaluate matrix elements of products of spherical tensor operators. Consider two spherical operators $T^{k_1}_{q_1}\left(\hat{O}_1\right)$ and $T^{k_2}_{q_2}\left(\hat{O}_2\right)$ acting on two subsystems independently, i.e. $T^{k_1}_{q_1}\left(\hat{O}_1\right)$ commutes with all the operators relative to the subsystem 2 and in particular with $\hat{\mathbf{J}}_2$ with similar considerations applying to $T^{k_2}_{q_2}\left(\hat{O}_2\right)$. The matrix elements of the tensor product operator in the coupled basis

of the full system are given by

$$\langle \tau, j, m; \tau_1, j_1, \tau_2, j_2 | \left[T^{k_1}\left(\hat{O}_1\right) \otimes T^{k_2}\left(\hat{O}_2\right) \right]_q^k | \tau', j', m'; \tau'_1, j'_1, \tau'_2, j'_2 \rangle = \\ (-1)^{j-m} \begin{pmatrix} j & k & j' \\ -m & q & m'_j \end{pmatrix} \langle \tau, j; \tau_1, j_1, \tau_2, j_2 \| \left[T^{k_1}\left(\hat{O}_1\right) \otimes T^{k_2}\left(\hat{O}_2\right) \right]_q^k \| \tau', j'; \tau'_1, j'_1, \tau'_2, j'_2 \rangle \tag{2.41}$$

according to equation (2.37). The reduced matrix element can be expressed as product of the algebraic factor represented by a 9-j symbol and the product of the individual space reduced matrix elements

$$\langle \tau, j; \tau_1, j_1, \tau_2, j_2 \| \left[T^{k_1}\left(\hat{O}_1\right) \otimes T^{k_2}\left(\hat{O}_2\right) \right]_q^k \| \tau', j'; \tau'_1, j'_1, \tau'_2, j'_2 \rangle = [(2j+1)(2j'+1)(2k+1)]^{\frac{1}{2}} \\ \times \begin{Bmatrix} j_1 & j'_1 & k_1 \\ j_2 & j'_2 & k_2 \\ j & j' & k \end{Bmatrix} \sum_{\tau''} \langle \tau; \tau_1, j_1 \| T^{k_1}\left(\hat{O}_1\right) \| \tau''; \tau'_1, j'_1 \rangle \langle \tau''; \tau_2, j_2 \| T^{k_2}\left(\hat{O}_2\right) \| \tau'; \tau'_2, j'_2 \rangle \tag{2.42}$$

and the sum over τ'' is usually not necessary [35].

The evaluation of matrix elements for operators acting only one subsystem, let us say 1, in the coupled basis of the full system proceeds similarly

$$\langle \tau, j, m; \tau_1, j_1, \tau_2, j_2 | T^{k_1}_{q_1}\left(\hat{O}_1\right) | \tau', j', m'; \tau'_1, j'_1, \tau'_2, j'_2 \rangle = \delta_{\tau_2,\tau'_2} \delta_{j_2,j'_2} (-1)^{j-m} \begin{pmatrix} j & k_1 & j' \\ -m & q_1 & m'_j \end{pmatrix} \times \\ \times \langle \tau, j; \tau_1, j_1, j_2 \| T^{k_1}_{q_1}\left(\hat{O}_1\right) \| \tau', j'; \tau'_1, j'_1, j_2 \rangle. \tag{2.43}$$

In such case the reduced matrix element can be expressed as [35]

$$\langle \tau; \tau_1, j_1, j_2 \| T^{k_1}\left(\hat{O}_1\right) \| \tau'; \tau'_1, j'_1, j_2 \rangle = (-1)^{j_1+j_2+j'+k_1} \left[(2j+1)(2j'+1)\right]^{\frac{1}{2}} \begin{Bmatrix} j_1 & j & j_2 \\ j' & j'_1 & k_1 \end{Bmatrix} \times \\ \times \langle \tau; \tau_1, j_1 \| T^{k_1}\left(\hat{O}_1\right) \| \tau'; \tau'_1, j'_1 \rangle \tag{2.44}$$

A completely equivalent formula applies when an operator acts only on the subspace 2 by exchanging indices $1 \leftrightarrow 2$.

2.4 Spherical harmonics and bipolar spherical harmonics

In this section we introduce the spherical harmonics as a basis for the irreducible representations for a system that can be described in terms of scalar wave-functions. Bipolar spherical harmonics are then defined as a spherical basis for composite systems. Suc-

cessively it will be shown how spherical and bipolar spherical harmonics may be used as spherical operators.

Consider a system that can be described by a wave-function $\Psi(\boldsymbol{P})$ with $\boldsymbol{P} = \{X, Y, Z\}$ or $\boldsymbol{P} = \{r, \theta, \phi\}$ using Cartesian or spherical coordinates respectively. The action of a rotation over a wave-function is defined by the following equations

$$\Psi \overset{\hat{R}_{\boldsymbol{n}}(\Theta)}{\rightarrow} \Psi' = \hat{R}_{\boldsymbol{n}}(\Theta)[\Psi], \tag{2.45a}$$

$$\Psi'(\boldsymbol{P}) \overset{\text{def}}{=} \Psi\left(\left[\hat{R}_{\boldsymbol{n}}(\Theta)\right]^{-1}[\boldsymbol{P}]\right). \tag{2.45b}$$

This corresponds an active rotation of the *object* Ψ in the reference frame $OXYZ$. The angular momentum operators are then represented by differential operators:

$$\hat{J}_X = -\mathrm{i}\left(Y\frac{\partial}{\partial Z} - Z\frac{\partial}{\partial Y}\right) = \mathrm{i}\left(\sin\phi\frac{\partial}{\partial\theta} + \cot\theta\cos\phi\frac{\partial}{\partial\phi}\right) \tag{2.46a}$$

$$\hat{J}_Y = -\mathrm{i}\left(Z\frac{\partial}{\partial X} - X\frac{\partial}{\partial Z}\right) = -\mathrm{i}\left(\cos\phi\frac{\partial}{\partial\theta} - \cot\theta\sin\phi\frac{\partial}{\partial\phi}\right) \tag{2.46b}$$

$$\hat{J}_Z = -\mathrm{i}\left(X\frac{\partial}{\partial Y} - Y\frac{\partial}{\partial X}\right) = -\mathrm{i}\frac{\partial}{\partial\phi} \tag{2.46c}$$

$$\hat{J}^2 = -\frac{1}{\sin\theta}\frac{\partial}{\partial\theta}\left(\sin\theta\frac{\partial}{\partial\theta}\right) - \frac{1}{\sin^2\theta}\frac{\partial^2}{\partial^2\phi} \tag{2.46d}$$

in Cartesian and polar coordinates respectively. The irreducible angular momentum representations have dimensions $(2j+1)$ where j is an integer. Explicitly the basis $|j, m\rangle$ is given by the spherical harmonics

$$|j, m\rangle = Y_{jm}(\theta, \phi) = \Theta_{jm}(\theta)\Phi_m(\phi) \tag{2.47}$$

with

$$\Theta_{jm}(\theta) = \left[\frac{2j+1}{2}\frac{(j-m)!}{(j+m)!}\right]^{1/2} P_{jm}(\cos\theta), \tag{2.48a}$$

$$\Phi_m(\phi) = \sqrt{\frac{1}{2\pi}}\mathrm{e}^{\mathrm{i}m\phi}, \tag{2.48b}$$

where $P_{jm}(\cos\theta)$ are the associated Legendre polynomials. For negative m the phase convention of [36] is followed: $P_{jm}(\cos\theta) = (-1)^m P_{j|m|}(\cos\theta)$. The spherical harmonics satisfy equation (2.10) and are normalized according to

$$\int_0^{\pi}\int_0^{2\pi} \sin\theta \mathrm{d}\theta\mathrm{d}\phi\, Y^*_{jm}(\theta, \phi) Y_{j'm'}(\theta, \phi) = \delta_{j,j'}\delta_{m,m'}, \tag{2.49}$$

$Y^*_{jm}(\theta, \phi)$ being the complex conjugate of $Y_{jm}(\theta, \phi)$.

Bipolar spherical harmonics $F^{j_1 j_2}_{jm}$ are a generalization of spherical harmonics for a system composed by two subsystems described by scalar wafefunctions in the independent variables $\{r_1, \theta_1, \phi_1\}$ and $\{r_2, \theta_2, \phi_2\}$. The (commuting) orbital angular momenta of two subsystems $\boldsymbol{J}_1$ and $\boldsymbol{J}_2$ can be combined to give the total orbital angular momentum: $\mathbf{J} = \boldsymbol{J}_1 + \boldsymbol{J}_2$. The irreducible representations are built according to the prescriptions given in 2.2. The coupled basis is given by bipolar spherical harmonics obtained as the composition of spherical harmonics

$$|j, m; j_1, j_2\rangle = F^{j_1 j_2}_{jm}(\theta_1, \phi_1, \theta_2, \phi_2) \stackrel{\text{def}}{=} C^{jm}_{j_1 m_1, j_2 m_2} Y_{j_1 m_1}(\theta_1, \phi_1) Y_{j_2 m_2}(\theta_2, \phi_2) \tag{2.50}$$

according to equation (2.15b). Any positive integer power of the scalar product of two vectors can be expanded in terms of bipolar harmonics of rank 0 as

$$(\boldsymbol{r}_1 \cdot \boldsymbol{r}_2)^n = 4\pi (r_1 r_2)^n \sum_l \frac{(-1)^l \sqrt{2l+1}\, n!}{(n-l)!!(n+l+1)!!} F^{ll}_{00}(\theta_1, \phi_1, \theta_2, \phi_2) \tag{2.51}$$

where the index l assumes the values $l = 0, 2, \ldots, n-2, n$ if n is even and $n = 1, 3, \ldots, n-1$ if n is odd [29, 37].

2.4.1 Associated spherical operators

Spherical harmonics $Y_{kq}(\theta, \phi)$ with given k define a spherical tensor operator acting multiplicatively over functions $\Psi(r, \theta, \phi)$

$$T^k_q\left(\hat{Y}\right)\Psi \stackrel{\text{def}}{=} Y_{kq}(\theta, \phi)\Psi(r, \theta, \phi), \tag{2.52a}$$

$$T^k_q\left(\hat{Y}\right)[c_1\Psi_1 + c_2\Psi_2] = c_1 T^k_q\left(\hat{Y}\right)\Psi_1 + c_2 T^k_q\left(\hat{Y}\right)\Psi_2. \tag{2.52b}$$

Similarly bipolar spherical harmonics $F^{k_1 k_2}_{kq}$ with given k define a spherical tensor operator acting multiplicatively over functions $\Psi(r_1, \theta_1, \phi_1\, r_2, \theta_2, \phi_2)$ of two independent polar coordinate sets

$$T^{k,k_1k_2}_q\left(\hat{F}\right)\Psi \stackrel{\text{def}}{=} F^{j_1 j_2}_{jm}(\theta_1, \phi_1, \theta_2, \phi_2)\, \Psi(r_1, \theta_1, \phi_1\, r_2, \theta_2, \phi_2), \tag{2.53a}$$

$$T^{k,k_1k_2}_q\left(\hat{F}\right)[c_1\Psi_1 + c_2\Psi_2] = c_1 T^{k,k_1k_2}_q\left(\hat{F}\right)\Psi_1 + c_2 T^{k,k_1k_2}_q\left(\hat{F}\right)\Psi_2. \tag{2.53b}$$

Note the use of a different symbol to distinguish the use of spherical harmonics and bipolar spherical harmonics as spherical operators from their use as states.

The matrix element of the spherical operator, equation (2.52a), over the spherical

basis, equation (2.47), is given by the integral

$$\begin{aligned}\langle j,m|T^k_q\left(\hat{Y}\right)|j',m'\rangle &= \int_0^{\pi}\int_0^{2\pi} \sin\theta \mathrm{d}\theta\mathrm{d}\phi\, Y^*_{jm}(\theta,\phi)Y_{kq}(\theta,\phi)Y_{j'm'}(\theta,\phi)\\ &= (-1)^{j-m}\begin{pmatrix} j & k & j' \\ -m & q & m'\end{pmatrix}\begin{pmatrix} j & k & j' \\ 0 & 0 & 0\end{pmatrix}\left[\frac{(2j+1)(2k+1)(2j'+1)}{4\pi}\right]^{1/2},\end{aligned} \tag{2.54}$$

whence the reduced matrix element for the spherical harmonic operator, compare equation (2.37), is

$$\langle j\|T^k\left(\hat{Y}\right)\|j'\rangle = \begin{pmatrix} j & k & j' \\ 0 & 0 & 0\end{pmatrix}\left[\frac{(2j+1)(2k+1)(2j'+1)}{4\pi}\right]^{1/2}. \tag{2.55}$$

The matrix element of a bipolar spherical operator, equation (2.53a), over the coupled basis, equation (2.50), can be evaluated using the Wigner-Eckart theorem for composite systems, equation (2.41):

$$\langle j,m;j_1,j_2|T^{k,k_1k_2}_q\left(\hat{F}\right)|j',m';j'_1,j'_2\rangle = (-1)^{j-m}\begin{pmatrix} j & k & j' \\ -m & q & m'\end{pmatrix}\langle j;j_1j_2\|T^{k,k_1k_2}_q\left(\hat{F}\right)\|j';j'_1,j'_2\rangle \tag{2.56}$$

where, according to equation (2.42),

$$\begin{aligned}\langle j;j_1,j_2\|T^{k,k_1k_2}_q\left(\hat{F}\right)\|j';j'_1,j'_2\rangle &= [(2j+1)(2j'+1)(2k+1)]^{\frac{1}{2}}\begin{Bmatrix} j_1 & j'_1 & k_1 \\ j_2 & j'_2 & k_2 \\ j & j' & k\end{Bmatrix}\\ &\times\langle j_1\|T^{k_1}\left(\hat{Y}\right)\|j'_1\rangle\langle j_2\|T^{k_2}\left(\hat{Y}\right)\|j'_2\rangle\end{aligned} \tag{2.57}$$

and finally the individual reduced matrix elements can be evaluated with the use of equation (2.55).

The evaluation of matrix elements in the way outlined here provides a powerful tool for the analysis of the quantum dynamics and the spectroscopy in endohedral dihydrogen fullerenes. Quantum mechanical operators, such as the translation-rotation interaction and the dipolar spin Hamiltonian, may be written in terms of bipolar spherical harmonics, equation (2.53a), for which equations (2.56) and (2.57) allow one to evaluate matrix representations in the coupled basis.

Chapter 3

Theory

In this chapter the dynamics of endohedral hydrogen trapped in C_{60} is discussed. The aim is to provide the theoretical framework for the interpretation and the analysis of infrared spectroscopy observations. The classical Hamiltonian for the nuclear motion of a diatomic molecule confined in a rigid fullerene cage is presented and the confining potential is expanded in spherical multipoles. The confining potential is determined by the high symmetry and its strength can be estimated either by basic ab initio computations or by semi-empirical two body carbon-hydrogen interactions. The evidence is that molecular hydrogen behaves as a vibrating rotor rattling in an approximate isotropic potential: the translational motion is expected to be quantized and coupled to the molecular rotations because of the confinement. The potential for the translational motion is shown to be mainly harmonic: anharmonic corrections and roto-translational couplings can be treated as perturbations. In absence of more detailed ab initio calculations the vibrational energy levels are described by the use of few parameters (vibrational frequency, vibrational anharmonic correction, and roto-vibrational correction) rather than referring to the inter-nuclear potential for the confined case. Since the vibrational energy is large, the rotational-translational motion is studied via an effective Hamiltonian. In each vibrational state the distribution of the roto-translational energy levels depends on the coefficients of the expansion of the confining potential in terms of spherical multipoles. Such coefficients have been written in terms of the parameters describing the carbon-hydrogen interactions for a Lennard-Jones 12-6 potential. Ideally the comparison between theory and experimental spectra provides indirect access to such parameters that can be reliably used to study the dynamics of hydrogen in similar systems.

3.1 Classical description of a dihydrogen molecule inside a rigid C_{60} cage

A basic relationship of classical mechanics, repeatedly used in the following derivations, is discussed first. In classical mechanics the kinetic energy of a system of two

material points can be rewritten as sum of the kinetic energies of the center of mass and that of the relative vector. Explicitly, given two points with mass m_1 and m_2 and linear momenta $\boldsymbol{p}_1$ and $\boldsymbol{p}_2$, the kinetic energy is given by

$$K.E. = \frac{\boldsymbol{p}_1^2}{2m_1} + \frac{\boldsymbol{p}_2^2}{2m_2} = \frac{\boldsymbol{P}^2}{2M} + \frac{\boldsymbol{p}^2}{2\mu}. \tag{3.1}$$

Here $\boldsymbol{P}$ and $\boldsymbol{p}$ are the linear momenta associated to the center of mass $\boldsymbol{R}$ and relative $\boldsymbol{r}$ vector, respectively. The mass associated with the center of mass vector is the total mass $M = m_1 + m_2$ and the mass associated to the relative motion is the reduced mass $\mu = m_1 * m_2/(m_1 + m_2)$. Equation 3.1 is a direct consequence of the following relationships among pairs of conjugated dynamical variables, $\{(\boldsymbol{P}, \boldsymbol{R}), (\boldsymbol{p}, \boldsymbol{r})\}$ and $\{(\boldsymbol{p}_1, \boldsymbol{r}_1), (\boldsymbol{p}_2, \boldsymbol{r}_2)\}$:

$$\boldsymbol{P} = M\dot{\boldsymbol{R}} = \boldsymbol{p}_1 + \boldsymbol{p}_2 \qquad \boldsymbol{R} = \frac{m_1\boldsymbol{r}_1 + m_2\boldsymbol{r}_2}{m_1 + m_2} \tag{3.2}$$

$$\boldsymbol{p} = \mu\dot{\boldsymbol{r}} = \mu\left(\frac{\boldsymbol{p}_2}{m_2} - \frac{\boldsymbol{p}_1}{m_1}\right) \qquad \boldsymbol{r} = \boldsymbol{r}_2 - \boldsymbol{r}_1 \tag{3.3}$$

The inverse relationships are given by

$$\boldsymbol{p}_1 = \frac{m_1}{M}\boldsymbol{P} - \boldsymbol{p} \qquad \boldsymbol{p}_2 = \frac{m_2}{M}\boldsymbol{P} + \boldsymbol{p} \tag{3.4}$$

$$\boldsymbol{r}_1 = \boldsymbol{R} - \frac{\mu}{m_1}\boldsymbol{r} \qquad \boldsymbol{r}_2 = \boldsymbol{R} + \frac{\mu}{m_2}\boldsymbol{r} \tag{3.5}$$

In a given reference frame the configuration of a rigid C_{60} molecule can be defined by its center of mass vector $\boldsymbol{R}_{C_{60}}$ and its orientation with respect to the axis system. The orientation of a C_{60} molecule is more precisely defined by a set of 3 Euler angles, collectively denoted by $\Omega_{C_{60}}$, relating a frame rigidly bounded to the fullerene to the laboratory frame. In an analogous way the configuration of a diatomic molecule AB is defined by its center of mass vector $\boldsymbol{R}_{AB}$ and its orientation $\Omega_{\boldsymbol{R}_{AB}}$. The orientation of a linear molecule is determined by two polar angles defined by the internuclear A-B relative vector $\boldsymbol{r}_{AB}$ in the given frame. If AB is not considered rigid the relative nuclear distance r_{AB} has to be included among the dynamical variables. In C_{60} the center of mass coincides with the geometrical center of the molecule while for a diatomic molecule this happens only in the homonuclear case. The classical Hamiltonian for a diatomic molecule in a rigid C_{60} cage is given by the sum of their kinetic energies plus the intramolecular potential of AB and the intermolecular potential between the cage and the endohedral molecule:

$$\mathcal{H} = \underbrace{\frac{P_{C_{60}}^2}{2m_{C_{60}}} + \frac{I_{C_{60}}\omega_{C_{60}}^2}{2}}_{(K.E.)_{C_{60}}} + \underbrace{\frac{P_{AB}^2}{2m_{AB}} + \frac{p_{AB}^2}{2\mu_{AB}}}_{(K.E.)_{AB}} + V^{A-B}(r_{AB}) + V^{C_{60}-AB}(\Omega_{C_{60}}, \boldsymbol{R}_{C_{60}}, \boldsymbol{R}_{AB}, \boldsymbol{r}_{AB}) \tag{3.6}$$

where

- $\boldsymbol{P}_{C_{60}}$ is the linear momentum of C_{60} associated with its center of mass vector $\boldsymbol{R}_{C_{60}}$;
- $I_{C_{60}}$ is the momentum of inertia of C_{60} (a spherical top) with respect to its center and $\omega_{C_{60}}$ is the modulus of the angular speed associated with the rotation of C_{60};
- $\boldsymbol{P}_{AB}$ is the linear momentum of AB associated with its center of mass vector $\boldsymbol{R}_{AB}$ and $m_{AB} = m_A + m_B$;
- $\boldsymbol{p}_{AB}$ is the linear momentum associated with the internuclear vector $\boldsymbol{r}_{AB}$ and $\mu_{AB} = m_A * m_B/(m_A + m_B)$ is the reduced mass of the diatomic molecule;
- V^{A-B} is the intramolecular potential for the molecule AB;
- $V^{C_{60}-AB}$ is the intermolecular potential between C_{60} and AB.

The potential $V^{C_{60}-AB}$ depends on the relative position of the center of mass and on the orientation of AB and C_{60}:

$$V^{C_{60}-AB}(\Omega_{C_{60}}, \boldsymbol{R}_{C_{60}}, \boldsymbol{R}_{AB}, \boldsymbol{r}_{AB}) = V^{C_{60}-AB}(\Omega_{C_{60}}, \boldsymbol{R}_{AB} - \boldsymbol{R}_{C_{60}}, \boldsymbol{r}_{AB}). \tag{3.7}$$

Using equation (3.1) the Hamiltonian can then be rewritten as

$$\mathcal{H} = \frac{\boldsymbol{P}_T^2}{2m_T} + \frac{I_{C_{60}}\omega_{C_{60}}^2}{2} + \frac{\boldsymbol{p}_{AB@C_{60}}^2}{2\mu_{AB@C_{60}}} + \frac{\boldsymbol{p}_{AB}^2}{2\mu_{AB}} + V^{A-B}(r_{AB}) + V^{C_{60}-AB}(\Omega_{C_{60}}, \boldsymbol{R}_{AB} - \boldsymbol{R}_{C_{60}}, \boldsymbol{r}_{AB}) \tag{3.8}$$

where

- $\boldsymbol{P}_T$ is the linear momentum associated with the center of mass vector of the complex AB@C_{60}: $\boldsymbol{R}_{AB@C_{60}} = (m_{AB}\boldsymbol{R}_{AB} + m_{C_{60}}\boldsymbol{R}_{C_{60}})/(m_{AB} + m_{C_{60}})$;
- $\boldsymbol{p}_{AB@C_{60}}$ is the linear momentum of AB associated with the difference of center of mass vectors $\boldsymbol{R}_{AB} - \boldsymbol{R}_{C_{60}}$;
- $\mu_{AB@C_{60}} = m_{AB}m_{C_{60}}/(m_{AB} + m_{C_{60}})$ is the reduced mass of the confined molecule.

Equation (3.8) shows that the translational motion of the center of mass of the system is decoupled from all the internal dynamics. This degree of freedom will be neglected in the following. A first approximation, justified by the high molecular symmetry, consists in neglecting the terms in the potential that depend explicitly on the orientation of C_{60}:

$$V^{C_{60}-AB}(\Omega_{C_{60}}, \boldsymbol{R}_{AB} - \boldsymbol{R}_{C_{60}}, \boldsymbol{r}_{AB}) \rightarrow V^{C_{60}-AB}(\boldsymbol{R}_{AB} - \boldsymbol{R}_{C_{60}}, \boldsymbol{r}_{AB}). \tag{3.9}$$

That is completely equivalent to considering C_{60} as a spherical molecule. In this approximation the rotational motion of C_{60} is decoupled from the internal dynamics and

can also be neglected. The Hamiltonian for the motion of $AB@C_{60}$ in the spherical approximation is given by:

$$\mathcal{H} = \frac{\boldsymbol{P}^2}{2M} + \frac{\boldsymbol{p}^2}{2\mu} + U^{AB@C_{60}}(\boldsymbol{R}, \boldsymbol{r}) \tag{3.10a}$$

$$U^{AB@C_{60}}(\boldsymbol{R}, \boldsymbol{r}) = V^{A-B}(r) + V^{C_{60}-AB}(\boldsymbol{R}, \boldsymbol{r}). \tag{3.10b}$$

where a simplified notation was used

$$\boldsymbol{P} = \boldsymbol{p}_{AB@C_{60}}, \tag{3.11a}$$

$$M = \mu_{AB@C_{60}}, \tag{3.11b}$$

$$\boldsymbol{p} = \boldsymbol{p}_{AB}, \tag{3.11c}$$

$$\mu = \mu_{AB}, \tag{3.11d}$$

$$\boldsymbol{R} = \boldsymbol{R}_{AB} - \boldsymbol{R}_{C_{60}}, \tag{3.11e}$$

$$\boldsymbol{r} = \boldsymbol{r}_{AB}. \tag{3.11f}$$

Note that $\boldsymbol{R}$ is the vector going from the center of C_{60} to the center of mass of AB and $\{\boldsymbol{P}, \boldsymbol{R}\}$, $\{\boldsymbol{p}, \boldsymbol{r}\}$ are conjugate dynamical variables. For clarity the set of vectors defining the configuration of a diatomic molecule AB in a reference frame centered at C_{60} is shown in figure 3.1. The main result of this section is contained in equations (3.10a) and (3.10b) which state that the motion of a confined diatomic molecule in a spherically symmteric cage can be studied by using reduced masses and that the confining potential given by the sum of the intramolecular component V^{A-B} and of the intermolecular component $V^{C_{60}-AB}$. The intra molecular component depends on the separation r of the two nuclei but not on the orientation. The explicit form of the intramolecular potential and of the intermolecular potential is discussed in the following sections.

Symmetry considerations for the intermolecular potential

It is very convenient to expand the intermolecular potential $V^{C_{60}-AB}(\boldsymbol{R}, \boldsymbol{r})$ in terms of bipolar spherical harmonics where the angular variables are the polar angles $\Omega_{\boldsymbol{R}}$ and $\Omega_{\boldsymbol{r}}$. Assuming a spherical approximation for C_{60}, the intermolecular potential is invariant for any rotation of the cage or equivalently for any rotation of $\boldsymbol{R}$ and $\boldsymbol{r}$:

$$V^{C_{60}-AB}\left[\hat{R}_{\boldsymbol{n}}(\Theta)\,\boldsymbol{R}, \hat{R}_{\boldsymbol{n}}(\Theta)\,\boldsymbol{r}\right] = V^{C_{60}-AB}(\boldsymbol{R}, \boldsymbol{r}) \tag{3.12}$$

In the language of spherical tensors $V^{C_{60}-AB}$ is a tensor of rank 0, i.e. a scalar. As a consequence of the completeness of the bipolar spherical harmonics and assuming that

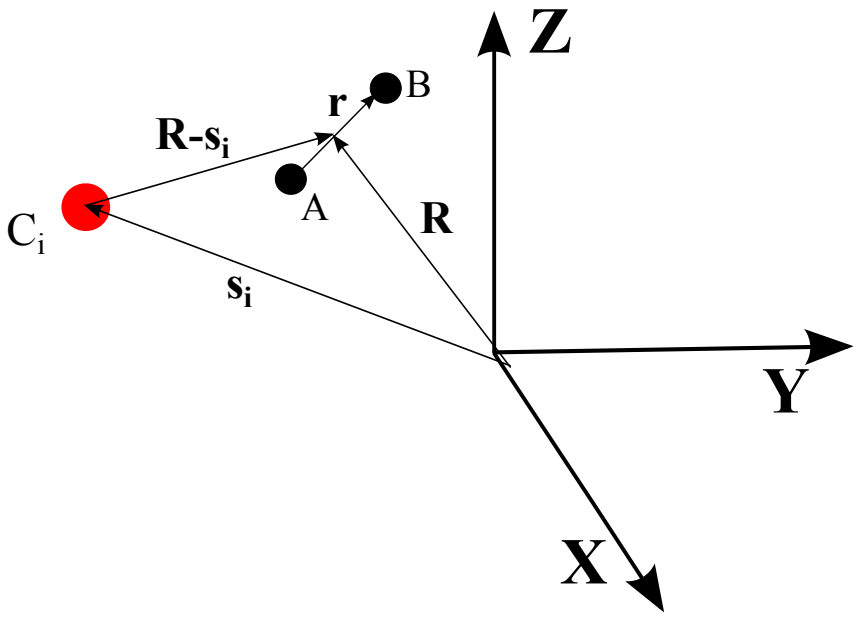

Figure 3.1: Graphical representation of the geometrical vectors defining the configuration of a diatomic molecule inside C_{60}. $\boldsymbol{R}$ is the vector going from the center of C_{60} to the center of mass of AB and $\boldsymbol{r}$ is the relative vector of AB. $\boldsymbol{s}_i$ is the vector going from the center of the fullerene to the $i-$th carbon atom. The coordinate system is centered at the center of the full system: diatomic molecule+fullerene.

the potential is an analytic function of its arguments the following expansion holds:

$$V^{C_{60}-AB}(\boldsymbol{R},\boldsymbol{r}) = \sum_{l,j}\sum_{n} V_{00}^{lj;n}(r)\, R^n F_{00}^{lj}(\Omega_{\boldsymbol{R}},\Omega_{\boldsymbol{r}}) \tag{3.13}$$

where the indices satisfy

(i) l and j are null or positive integers;

(ii) $l = j$ from the triangle relation;

(iii) n is a null or a positive integer; because of equation (2.51) coefficients with n odd must have l = odd and terms with n even must have l = even;

(iv) $V_{00}^{lj;0} = 0$ unless $l = 0$ because when the center of mass of the diatomic molecule is at the center of the fullerene the potential cannot depend on the corresponding angular variables;

(v) for homonuclear molecules only even j terms are allowed;

(vi) for homonuclear molecules n is even.

Bipolar spherical harmonics can be used to expand the intermolecular potential even when the real icosahedral symmetry of C_{60} is considered. In icosahedral symmetry the

dependence on the cage orientation $\Omega_{C_{60}}$ cannot be discarded. The intermolecular potential is invariant under any symmetry operation of the group I_h and belongs to the total symmetric representation A_{1g}. In such a case the following terms in the multipolar expansion are represented by bipolar spherical harmonics of rank $6, 10, \ldots$ [38]. Multipoles of rank higher than 0 are responsible for lifting the degeneracy of the quantum energy levels obtained in the spherical approximation, for homogeneous broadening of spectroscopic lines and for the coupling between the rotation of the endohedral molecule and that of C_{60}. In the following the spherical approximation will be assumed and the orientation/rotational motion of the fullerene will become irrelevant for the quantum dynamics of the confined hydrogen: all the angular variables will be then referred to the laboratory system. It will be understood that AB = HD or H_2 or D_2.

3.2 Potential for a dihydrogen molecule inside C_{60}

In a molecule the electrons move fast while the heavier nuclei hardly move from their equilibrium position. This observation is the basis for the study of molecular dynamics in the Born-Oppenheimer approximation: the Schrödinger equation for the electrons in the molecule is solved with the nuclei at fixed positions for all the possible nuclear configurations. The energy associated with the motion of the electrons (electronic energy) is then a function of the coordinates of all the nuclei. The dependence of the electronic energy, which includes the internuclear Coulombian repulsion energy, on the nuclear coordinates can be visualized as a potential electronic surface (PES). The nuclei perform small oscillations around the equilibrium position defined by the minimum/minima of the PES. The scheme depicted above describes accurately a molecule in its electronic ground state.

The PES for a diatomic molecule confined in a rigid molecular frame is a function of the nuclear coordinates of the diatomic molecule, for a total of six variables. The computational evaluation of the six dimensional PES for an hydrogen molecule moving inside the cavity of a fullerene, considered as rigid, is a formidable task. No high level calculations faced such a problem up to now. A quantum dynamical evaluation by Cross[1] of few points of the PES of $H_2@C_{60}$ showed that the confined hydrogen molecule, approximated as rigid, does not stick to the wall of the C_{60} cage but rather rotates almost freely in the confining potential. This justifies the treatment of endohedral dihydrogen fullerenes as made by two units: the hydrogen molecule and the enclosing cage. The internuclear (hydrogen-hydrogen) potential is only slightly modified by the confinement and the hydrogen molecule can be thought as a whole object moving in the external potential determined by the cage. For endohedral hydrogen the potential energy surface is then the sum of the internuclear potential plus the confining potential. The justification of such an approximation relies in the consistency and in the matching of theoretical predictions with experimental observations. Figure 3.2 shows the PES for a rigid hydrogen molecule inside C_{60} as computed in [1]. The confining potential

has mainly a parabolic character with a minimum when the fullerene is at the center of the cage, i.e at $\boldsymbol{R} = \mathbf{0}$. A very small dependence on the orientation of the internuclear vector is evident when the H_2 is off center: such anisotropy torque is responsible for the translation-rotation interaction term in the potential.

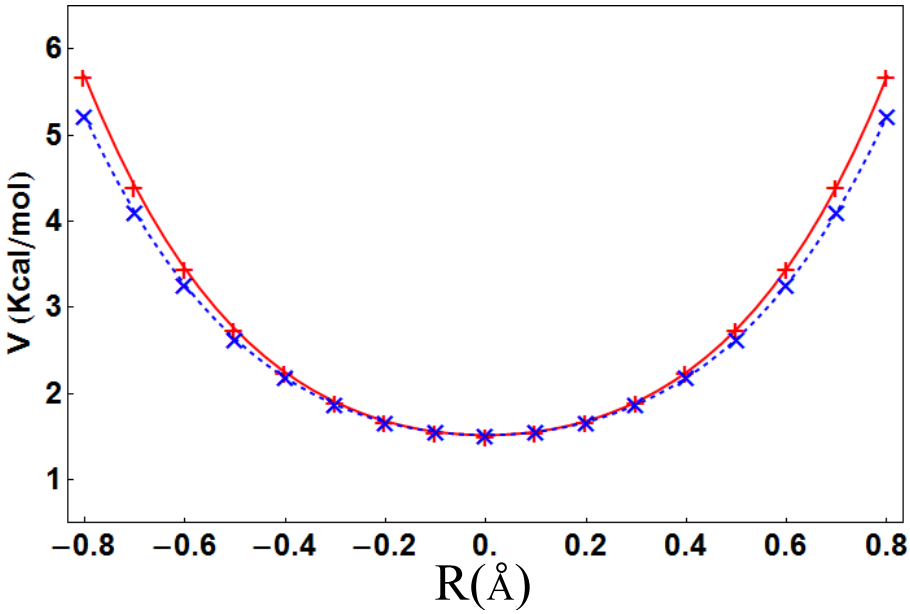

Figure 3.2: The potential electronic surface for $H_2@C_{60}$ from ab initio calculation has been explored moving the center of a rigid H_2 molecule along the fivefold symmetry axis of a rigid fullerene: the (+) and (×) symbols represent the computed energy for H_2 parallel and perpendicular to such axis, respectively. The two lines represent the best fits to the computed points. Adapted from [1].

Intermolecular potential

The difficulty of computing a reliable PES for a hydrogen molecule inside C_{60} by ab initio methods and therefore to estimating the influence of the confinement on the dynamics of the confined molecule is circumvented by assuming that the interaction of the hydrogen molecule with the cage can be written as a pairwise additive potential of the form [39]:

$$V^{C_{60}-AB}(\boldsymbol{r}_A, \boldsymbol{r}_B) = \sum_{k=1}^{60} V^{C-AB}(\boldsymbol{r}_A, \boldsymbol{r}_B, \boldsymbol{s}_k) \tag{3.14}$$

where the variables $\boldsymbol{r}_A$, $\boldsymbol{r}_B$ correspond to the positions of the nuclei, A and B, and $\boldsymbol{s}_k, 1 \leq k \leq 60$ corresponds to the fixed positions of each of the sixty carbon nuclei. In other words, the carbon atoms interact independently with the hydrogen molecule and the confining potential is the sum of such interactions over all the carbon atoms. Since in a dihydrogen molecule the electronic configuration depends on the charge of the nuclear species rather than on its mass, it is safe to assume that the instantaneous interaction of a single hydrogen molecule with a carbon atom does not depend on the

hydrogen isotopomer so that $V^{\mathrm{C-AB}} = V^{\mathrm{C-H_2}}$. A realistic potential has to take in account that in the hydrogen ground electronic state most of the electronic density is located at the geometric center of the molecule $(\boldsymbol{r}_\mathrm{A} + \boldsymbol{r}_\mathrm{B})/2$ and not only around the two hydrogen nuclei. In reference [2] the authors suggested that a three site potential may represent well such a situation:

$$V^{\mathrm{C-H_2}}_{\text{3 sites}}(\boldsymbol{r}_\mathrm{A}, \boldsymbol{r}_\mathrm{B}) = V^{\mathrm{C-H}}(\boldsymbol{s}, \boldsymbol{r}_\mathrm{A}) + V^{\mathrm{C-H}}(\boldsymbol{s}, \boldsymbol{r}_\mathrm{B}) + wV^{\mathrm{C-H}}(\boldsymbol{s}, \frac{\boldsymbol{r}_\mathrm{A} + \boldsymbol{r}_\mathrm{B}}{2}) \tag{3.15}$$

where $V^{\mathrm{C-H}}$ is the interaction between the carbon atom placed in $\boldsymbol{s}$ and the site located at nuclear positions $\boldsymbol{r}_\mathrm{A}$ and $\boldsymbol{r}_\mathrm{B}$ and w is a multiplicative factor weighting the interaction with the site located at the geometric center of the hydrogen molecule. If one defines the interaction between the cage and a site by summing the single site interaction $V^{\mathrm{C-H}}$ on all the carbon atoms as

$$V^{\mathrm{C_{60}-H}}(\boldsymbol{x}) = \sum_{i=1}^{60} V^{\mathrm{C-H}}(\boldsymbol{s}_i, \boldsymbol{x}), \tag{3.16}$$

the fullerene-hydrogen potential can be written as the sum of interactions between the cage and each of the three sites as follows:

$$V^{\mathrm{C_{60}-AB}}(\boldsymbol{r}_\mathrm{A}, \boldsymbol{r}_\mathrm{B}) = V^{\mathrm{C_{60}-H}}(\boldsymbol{r}_\mathrm{A}) + V^{\mathrm{C_{60}-H}}(\boldsymbol{r}_\mathrm{B}) + wV^{\mathrm{C_{60}-H}}(\frac{\boldsymbol{r}_\mathrm{A} + \boldsymbol{r}_\mathrm{B}}{2}). \tag{3.17}$$

by using equation (3.15) and the definition equation (3.16). In the spherical approximation the interaction with carbon atoms is spread evenly on the surface of a sphere so that the sum over the carbon atoms in equation (3.16) can be replaced by an integral over a spherical distribution

$$V^{\mathrm{C_{60}-H}}(\boldsymbol{x}) = \sum_{i=1}^{60} V^{\mathrm{C-H}}(\boldsymbol{s}_i, \boldsymbol{x}) \to V_\mathrm{S}^{\mathrm{C_{60}-H}}(\boldsymbol{x}) = \frac{60}{4\pi}\int_{\mathrm{Sphere}} \mathrm{d}\Omega_{\boldsymbol{s}}\, V^{\mathrm{C-H}}(\boldsymbol{s}, \boldsymbol{x}). \tag{3.18}$$

By symmetry arguments $V_\mathrm{S}^{\mathrm{C_{60}-H}}$ depends only on the distance from the center of the fullerene $x = |\boldsymbol{x}|$. As a further step the single site potential $V^{\mathrm{C-H}}$ can be described in terms of a Lennard-Jones (LJ) 6-12 potential:

$$V^{\mathrm{C-H}}(\boldsymbol{x}) = 4\epsilon\left[\left(\frac{\sigma}{|\boldsymbol{x}|}\right)^{12} - \left(\frac{\sigma}{|\boldsymbol{x}|}\right)^{6}\right]. \tag{3.19}$$

In equation (3.19) the power-12 term describes the repulsive interaction for short internuclear distance while the power-6 term represents the attractive tail of the potential at long distance. ϵ is the minimum value of the potential and σ is related to the equilibrium distance by $|\boldsymbol{x}|_E = \sqrt[6]{2}\sigma$. Neglecting the constant term, the polynomial approximation

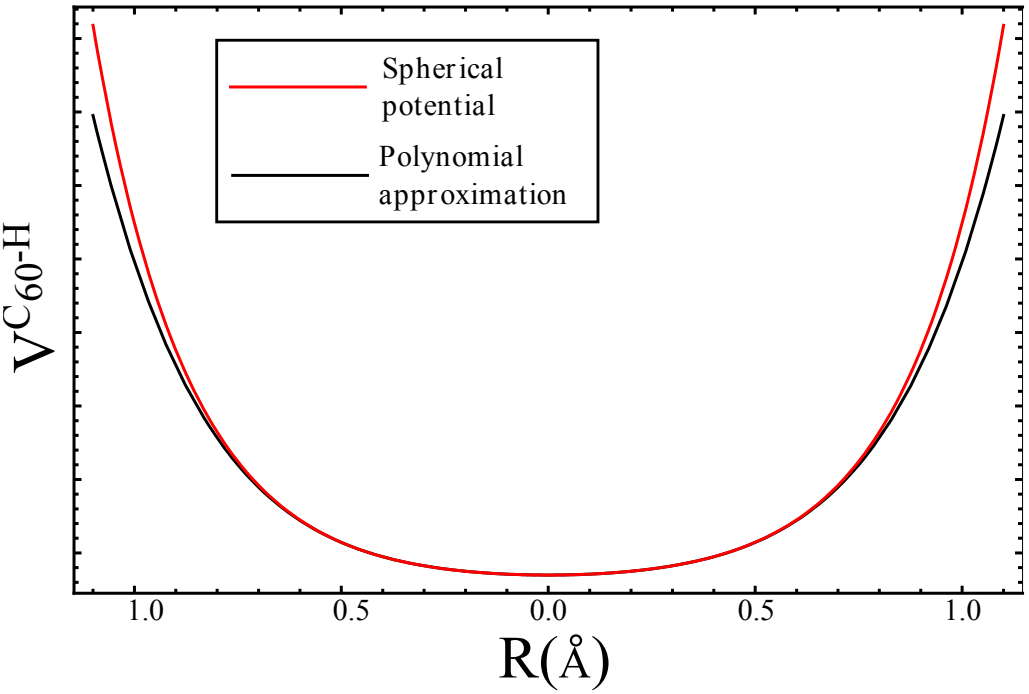

Figure 3.3: Comparison between the spherical approximation of the confining potential $V^{C_{60}-H}(R)$ inside a fullerene cage (red line) and its best polynomial approximation up to R^6 (black line). The spherical potential was obtained by smearing the carbon-hydrogen interactions over a sphere, see equation (3.18). The two curves are explicitly obtained from the 12-6 Lennard-Jones potential V^{C-H}, equation (3.19), with parameters from [2]. The vertical scale is in arbitrary units.

for $V_S^{C_{60}-H}(\boldsymbol{x})$ up to order 6 in x,

$$V_S^{C_{60}-H}(\boldsymbol{x}) \approx F_0 x^2 + H_0 x^4 + J_0 x^6, \tag{3.20}$$

is satisfactory for a wide range of the parameters ϵ and σ. In figure 3.3 the spherical potential, equation (3.18), is compared to the polynomial approximation, equation (3.20), using the values given in [2]. The difference is negligible for hydrogen moving within a sphere $x \leq 1$ Å.

The polynomial approximation in equation (3.20) is valid also when other forms of carbon-hydrogen interaction V^{C-H} are used and so it will be assumed without any reference to a specific potential V^{C-H}. In such a case the cage-molecule interaction, equation (3.17), can be written in terms of the center of mass vector $\boldsymbol{R}$ and relative internuclear vector $\boldsymbol{r}$ as:

$$V^{C_{60}-AB}(\boldsymbol{R},\boldsymbol{r}) = V^{C_{60}-H}\left(\boldsymbol{R} - \frac{\mu_{AB}}{m_A}\boldsymbol{r}\right) + V^{C_{60}-H}\left(\boldsymbol{R} + \frac{\mu_{AB}}{m_B}\boldsymbol{r}\right) + wV^{C_{60}-H}\left(\boldsymbol{R} + \frac{m_A - m_B}{2(m_A + m_B)}\boldsymbol{r}\right) \tag{3.21}$$

where μ_{AB} is the reduced mass of the diatomic molecule. For the heteronuclear HD the

potential in equation (3.21) can be expanded as

$$
\begin{aligned}
V^{\mathrm{C_{60}-HD}}(R,r) = {} & \underbrace{4\pi\left[(2+w)F_0 + \frac{5(20+w)}{54}H_0 r^2 + \frac{7(272+w)}{1296}J_0 r^4\right]}_{V_{00}^{00;2}(r)} R^2 F_{00}^{00} + \\
& \underbrace{4\pi\left[(2+w)H_0 + \frac{7(20+w)}{36}J_0 r^2\right]}_{V_{00}^{00;4}(r)} R^4 F_{00}^{00} \underbrace{-\frac{2\pi}{3\sqrt{3}}\left[2(2+w)F_0 r + \frac{(56+w)}{9}H_0 r^3\right]}_{V_{00}^{11;1}(r)} R F_{00}^{11} \\
& \underbrace{-\frac{2\pi}{3\sqrt{3}}\left[4(2+w)H_0 r + \frac{7(56+w)}{15}J_0 r^3\right]}_{V_{00}^{11;3}(r)} R^3 F_{00}^{11} + \\
& \underbrace{\frac{2\pi}{9\sqrt{5}}\left(\frac{4(20+w)}{3}H_0 r^2 + \frac{(272+w)}{9}J_0 r^4\right)}_{V_{00}^{22;2}(r)} R^2 F_{00}^{22} + \underbrace{\frac{8\pi}{9\sqrt{5}}(20+w)J_0 r^2}_{V_{00}^{22;4}(r)} R^4 F_{00}^{22} + \\
& \underbrace{-\frac{8\pi}{135\sqrt{7}}(56+w)J_0 r^3}_{V_{00}^{33;3}(r)} R^3 F_{00}^{33} + \underbrace{\frac{(20+w)}{36}F_0 r^2 + \frac{(272+w)}{1296}H_0 r^4}_{V^{\mathrm{conf}}(r)}.
\end{aligned}
\tag{3.22}
$$

considering terms up to R^4 and r^4. Here the dependence of the bipolar harmonics on the polar angles of $\boldsymbol{R}$ and $\boldsymbol{r}$ is understood. The potential has been reorganized to stress the connection with the multipole expansion, equation (3.13). Note that odd and even powers of R appear with odd and even bipolar harmonics respectively. In the following only the dynamics of homonuclear hydrogen $\mathrm{A_2} = \mathrm{H_2}, \mathrm{D_2}$ will be discussed leading to a simplified form of the confining potential

$$
\begin{aligned}
V^{\mathrm{C_{60}-A_2}}(R,r) = {} & \underbrace{4\pi\left[(2+w)F_0 + \frac{5}{3}H_0 r^2 + \frac{7}{8}J_0 r^4\right]}_{V_{00}^{00;2}(r)} R^2 F_{00}^{00} + \underbrace{4\pi\left[(2+w)H_0 + \frac{7}{2}J_0 r^2\right]}_{V_{00}^{00;4}(r)} R^4 F_{00}^{00} \\
& + \underbrace{\frac{16\pi}{\sqrt{5}}\left(\frac{H_0}{3}r^2 + \frac{J_0}{4}r^4\right)}_{V_{00}^{22;2}(r)} R^2 F_{00}^{22} + \underbrace{\frac{16\pi}{\sqrt{5}}J_0 r^2}_{V_{00}^{22;4}(r)} R^4 F_{00}^{22} + \underbrace{\frac{F_0}{2}r^2 + \frac{H_0}{8}r^4}_{V^{\mathrm{conf}}(r)}.
\end{aligned}
\tag{3.23}
$$

In the homonuclear case only even powers of R are present. Only four spherical multipoles are sufficient to describe the intermolecular potential $V^{\mathrm{C_{60}-A_2}}$. The $r-$only dependent part of $V^{\mathrm{C_{60}-A_2}}$ is incorporated into the vibrational potential as discussed in the next section while the remaining part constitutes the confining potential driving the dynamics of endohedral hydrogen.

It is worth giving an estimate of the magnitude of the coefficients using the values

reported in [2] for the LJ 12-6 potential: $\epsilon = 5.94 * 10^{-24}$ J and $\sigma = 2.95$ Å:

$$F_0 = 0.12 \text{ J m}^{-2} \tag{3.24a}$$
$$H_0 = 0.20 \times 10^{20} \text{ J m}^{-4} \tag{3.24b}$$
$$J_0 = 0.10 \times 10^{40} \text{ J m}^{-6} \tag{3.24c}$$

These values imply that the internuclear part of the confining potential $V^{\text{conf}}(r)$ is small compared to the internuclear potential in the free molecule, as will be shown in section 3.2: the former can be treated as a small perturbation of the latter. The expressions for the confining potential, equations (3.22) and (3.23), in terms of the parameters F_0, H_0, J_0 may be cumbersome but they give an indication of which terms have to be considered in the spherical multipole expansion. Furthermore the expected order of magnitude of the coefficients was obtained as function of the internuclear distance r.

Internuclear potential

For the isolated hydrogen molecule the electronic energy depends only on the internuclear distance r. For low excitation energies the nuclei perform only small oscillations around the minimum of the potential. It follows that for low energy vibrations such a potential can be approximated by a quadratic function centered at the equilibrium position r_e^{F}

$$V^{\text{A-B}}(r) \approx {f_e}^{\text{F}}(r - r_e^{\text{F}})^2, \tag{3.25}$$

neglecting the constant term at the minimum of the internuclear potential. The superscript F refers to free molecule parameters. In the quadratic approximation, neglecting molecular rotation, the vibrational motion is purely harmonic with $\omega_e^{\text{F}} = \sqrt{{f_e}^{\text{F}}/2\mu}$. A better approximation is given by the inclusion of cubic and quartic corrections

$$V^{\text{A-B}}(r) \approx {f_e}^{\text{F}}(r - r_e^{\text{F}})^2 + {g_e}^{\text{F}}(r - r_e^{\text{F}})^3 + {h_e}^{\text{F}}(r - r_e^{\text{F}})^4. \tag{3.26}$$

The anharmonic corrections ${g_e}^{\text{F}}$ accounts for the asymmetry of the internuclear potential around r_e. The influence of the cubic and quartic terms can be treated as perturbation of the quadratic one so that the vibrational motion is that of an anharmonic oscillator.

The effect of the confinement in the C_{60} case is to add further terms to the internuclear potential of the free molecule with the net result of modifying the internuclear distance, the vibrational frequency and the values for the coefficients of the cubic and quartic corrections, see equation (3.23). The influence of the confining potential V^{conf} on the internuclear potential is completely negligible as can be seen by comparing the values of the coefficients in equations (3.24) with the approximate values for the coeffi-

cients of $V^{\mathrm{A-B}}$ of free H_2:

$$f_e{}^{\mathrm{F}} \approx 286.6\ \mathrm{J\,m^{-2}}, \tag{3.27a}$$
$$g_e{}^{\mathrm{F}} \approx -556.9 \times 10^{10}\ \mathrm{J\,m^{-3}}, \tag{3.27b}$$
$$h_e{}^{\mathrm{F}} \approx 631.4 \times 10^{20}\ \mathrm{J\,m^{-4}}. \tag{3.27c}$$

This set of coefficients is obtained by comparing the theoretical expansion of the energy levels with the experimental spectra of the free molecule as explained in 3.3. An analogous analysis can also be done for D_2. At this point it is worth noting that the influence of the confinement on the internuclear dynamics can not be included only into V^{conf}. Quantum dynamical effects that influence the distribution of electrons in the endohedral molecule are not well incorporated into a potential energy surface derived from a Lennard Jones potential. Although a LJ type potential is adequate for describing the intermolecular part of the interaction in confined hydrogen it is not correct to assume it is the only source of corrections to the free molecule internuclear potential. The V^{conf} potential is part of the endohedral potential $V^{\mathrm{endo}}(r)$ which includes all the effects of the fullerene on the vibrational potential:

$$V^{\mathrm{vib}}(r) = V^{\mathrm{A-B}}(r) + V^{\mathrm{endo}}(r). \tag{3.28}$$

Assuming $V^{\mathrm{endo}}(r_e^{\mathrm{F}}) << V^{\mathrm{A-B}}(r_e^{\mathrm{F}})$, the effect on the internuclear potential may be evaluated by performing a series expansion of the internuclear potential in the neighborhood of the equilibrium distance:

$$\begin{aligned} V^{\mathrm{vib}}(r) &= f_e\,(r-r_e)^2 + g_e\,(r-r_e)^3 + h_e\,(r-r_e)^4 \\ &\approx (f_e{}^{\mathrm{F}} + \delta f_e)\left[r - (r_e^{\mathrm{F}} + \delta r_e)\right]^2 + (g_e{}^{\mathrm{F}} + \delta g_e)\left[r - (r_e^{\mathrm{F}} + \delta r_e)\right]^3 + \\ &\quad + (h_e{}^{\mathrm{F}} + \delta h_e)\left[r - (r_e^{\mathrm{F}} + \delta r_e)\right]^4. \end{aligned} \tag{3.29}$$

The variation of the internuclear equilibrium distance depends mostly on the first derivative of $V^{\mathrm{endo}}(r)$ at $r = r_e^{\mathrm{F}}$

$$\delta r_e \approx -\frac{\left.\frac{\partial V^{\mathrm{endo}}(r)}{\partial r}\right|_{r=r_e^{\mathrm{F}}}}{2f_e}, \tag{3.30}$$

while the corrections induced by higher order derivatives of V^{endo} are less important than the variation of internuclear distance in determining the coefficients f_e, g_e, h_e so that

$$\delta f_e \approx 3 g_e \delta r_e, \tag{3.31a}$$
$$\delta g_e \approx 4 h_e \delta r_e, \tag{3.31b}$$
$$\delta h_e \approx 0. \tag{3.31c}$$

The variation of δr_e has opposite sign to the first derivative of the endohedral potential at r_e. A positive variation in the internuclear distance $\delta r_e > 0$ is reflected in a reduction of f_e and hence a redshift of the classical vibrational frequency and vice versa $\delta r_e < 0$ implies blueshift since $g_e < 0$ for endohedral hydrogen. If the fullerene cage acts attractively on the endohedral molecule δr_e is expected to be positive and the vibrational frequency is expected to be redshifted and if the interaction is repulsive the opposite is expected.

3.2.1 Classical Hamiltonian for homonuclear hydrogen in C_{60}

According to the discussion relative to the confining potential for homonuclear hydrogen in C_{60} given in the previous section, the classical Hamiltonian can be separated into three parts:

$$\mathcal{H} = \mathcal{H}_{\text{V-R}} + \mathcal{H}_{\text{T}} + V_{\text{R-T}}. \tag{3.32}$$

The vibrational-rotational Hamiltonian $\mathcal{H}_{\text{V-R}}$ is that of a vibrating rotor with cubic and quartic corrections and equilibrium length r_e:

$$\mathcal{H}_{\text{V-R}} = \frac{\boldsymbol{p}^2}{2\mu} + \underbrace{f_e(r-r_e)^2 + g_e(r-r_e)^3 + h_e(r-r_e)^4}_{V^{\text{vib}}(r)} \tag{3.33}$$

The translational Hamiltonian $\mathcal{H}_{\text{T}}$ is that of a harmonic oscillator with anharmonic corrections:

$$\mathcal{H}_{\text{T}} = \underbrace{\frac{\boldsymbol{P}^2}{2M} + + V_{00}^{00;2}(r)R^2F_{00}^{00}}_{\mathcal{H}_{\text{T}}^{Har}} + \underbrace{V_{00}^{00;4}(r)R^4}_{\mathcal{H}_{\text{T}}^{An}} \tag{3.34}$$

The potential $V_{\text{R-T}}$ represents the coupling between the translational degrees of freedom and the rotational degrees of freedom:

$$V_{\text{R-T}}(r,R) = \left[V_{00}^{22;2}(r)R^2 + V_{00}^{22;4}(r)R^4\right]F_{00}^{22}. \tag{3.35}$$

A very simple but illuminating example to discuss is the harmonic approximation for both the $V^{\text{H}-\text{C}_{60}}$ and $V^{\text{vib}}(r)$:

$$\left.\begin{aligned} V^{\text{H}-\text{C}_{60}}(x) &= F_0x^2, \\ V^{\text{vib}}(r) &= f_0\,(r-r_0)^2 \end{aligned}\right\} \Rightarrow \mathcal{H}^{\text{A}_2} = \frac{\boldsymbol{P}^2}{2M} + (2+w)F_0R^2 + \frac{\boldsymbol{p}^2}{2\mu} + f_0(r-r_0)^2. \tag{3.36}$$

Classically the confining potential has a parabolic shape with a minimum when the geometric center of hydrogen is at the center of the cage. Within the harmonic approximation there is no coupling between the translational and the vibro-rotational motion. It is easy to see that the translational (subscript T) motion of the center of mass vector and the vibrational (subscript e) motion of the internuclear vector perform harmonic

oscillations independently and with classical frequencies given by:

$$\omega_T = \sqrt{\frac{(2+w)F_0}{M}}, \tag{3.37a}$$

$$\omega_e = \sqrt{\frac{2f_e}{\mu}}. \tag{3.37b}$$

Using the values equations (3.24) and (3.27), the purely harmonic translational and vibrational frequencies are expected to be around $180\,\mathrm{cm}^{-1}$ and $4400\,\mathrm{cm}^{-1}$ for $H_2@C_{60}$ and $140\,\mathrm{cm}^{-1}$ and $3100\,\mathrm{cm}^{-1}$ for $D_2@C_{60}$, respectively. Such values needs to be corrected by considering the influence of anharmonicities and interactions with the rotations prior to any comparison with experimental data. The separation of the Hamiltonian in equation (3.36) into two independent parts, harmonic vibrational and harmonic translational, suggests a perturbative study of the fully coupled dynamics in terms of the eigenfunctions of a vibrating rotor (internuclear vector) and an oscillator (center of mass vector) with both motions perturbed by anharmonic corrections. The classical Hamiltonian in equation (3.32) is the starting point for the study of the quantum dynamics of homonuclear dihydrogen enclosed in C_{60}.

3.3 Quantum dynamics of the vibro-rotational motion

The quantum Hamiltonian of a vibrating rotor with small anharmonic corrections is given by

$$\mathcal{H}_{\text{V-R}} = \frac{\boldsymbol{p}^2}{2\mu} + V^{\text{vib}}(r) = -\frac{\hbar^2}{2\mu} r \frac{\partial^2}{\partial^2 r} \frac{1}{r} + \frac{\hbar^2 \hat{\boldsymbol{J}}^2}{2\mu r^2} + f_e(r-r_e)^2 + g_e(r-r_e)^3 + h_e(r-r_e)^4 \tag{3.38}$$

where $V^{\text{vib}}(r)$ given in equation (3.29) and spherical coordinates $\{r, \theta, \phi\}$ have been used in the second line. The explicit form of the square of the angular momentum $\hat{\boldsymbol{J}}^2$ is given by the differential operator in the variables $\{\theta, \phi\}$, equation (2.46d). The centrifugal term $\hbar^2 \hat{\boldsymbol{J}}^2/(2\mu r^2)$ acts as a potential barrier at short distance. The radial symmetry of the vibration-rotation Hamiltonian, equation (3.38), allows one to separate the solution of the Schrödinger equation into a product of a radial times an angular part

$$\mathcal{H}_{\text{V-R}} \psi^{v,J,M_J}_{\text{vib-rot}}(r,\theta,\phi) = E^{v,J}_{\text{V-R}} \psi^{v,J,M_J}_{\text{vib-rot}}(r,\theta,\phi)\,, \tag{3.39a}$$

$$\psi^{v,J,M_J}_{\text{vib-rot}}(r,\theta,\phi) = \underbrace{\psi^{v,J}_{\text{vib}}(r)}_{\text{radial}} \underbrace{Y_{JM_J}(\theta,\phi)}_{\text{rotational}}. \tag{3.39b}$$

In Dirac's ket notation the eigenfunctions in equation (3.39b) can be written as $|v, J, M_J\rangle$. The rotational part of the wave-function is given by spherical harmonics

$$|J, M_J\rangle \stackrel{\text{def}}{=} Y_{JM_J}(\theta, \phi). \tag{3.40}$$

The integer quantum numbers J and M_J define the quantum angular momentum for rotation of the internuclear vector. J corresponds to the number of rotational quanta. The quantum number v labels the radial part of the wavefunctions together with J. In general the vibration-rotation Hamiltonian is not separable, even in the case of purely harmonic vibration potential, because vibrations and rotations are coupled by the dependence of the centrifugal term on $1/r^2$. Anyway the vibration rotation Hamiltonian of hydrogen can be approximatively separated into the Hamiltonian of a vibrator (for the radial part) and the Hamiltonian of a rotator (for the angular part) in the sense specified below. In such an approximation, the radial part of the eigenfunctions is given by

$$|v\rangle \stackrel{\text{def}}{=} \psi^v_{\text{vib}}(r) = \left(\frac{\beta_e}{\pi}\right)^{\frac{1}{4}} \left(\frac{1}{2^v v!}\right)^{\frac{1}{2}} \frac{1}{r}\, \mathrm{e}^{-\frac{\beta_e (r-r_e)^2}{2}}\, \mathtt{H}_v\left[\sqrt{\beta_e}(r - r_e)\right] \tag{3.41}$$

with

$$\beta_e = \frac{\mu \omega_e}{\hbar} \tag{3.42}$$

and the vibrational frequency defined by equation (3.37b). The radial wave-function depends only on the (null or positive) integer v referred as the number of quanta of vibrations. $\mathtt{H}_v$ are Hermite polynomials [36]: explicitly $\mathtt{H}_0(x) = 1$ and $\mathtt{H}_1(x) = x$ for $v = 0, 1$. The wave-function is centered at $r = r_e$ and its spatial extension is determined by:

$$\langle \Delta r \rangle_v \stackrel{\text{def}}{=} \left[\langle \psi^v_{\text{vib}}(r) | (r - r_e)^2 | \psi^v_{\text{vib}}(r) \rangle\right]^{\frac{1}{2}} = \sqrt{\left(v + \frac{1}{2}\right)\frac{1}{\beta_e}} \tag{3.43}$$

since the probability density falls down to 0 quickly within a few $\langle \Delta r \rangle_v$ from r_e. The vibrational rotational levels $|v, J\rangle$ are $(2J + 1)$-fold degenerate. The energy is approximately given by the sum of the vibrational energy E^v_{V} and the rotational energy ${}^vE^J_{\text{R}}$:

$$E^{v,J}_{\text{V-R}} \approx \underbrace{\hbar\, {}^v\omega_V \left(v + \frac{1}{2}\right)}_{E^v_{\text{V}}} + \underbrace{{}^vB\, J(J+1) - D_e\, [J(J+1)]^2}_{{}^vE^J_{\text{R}}} \tag{3.44}$$

For the sake of simplicity all terms which are constant with respect to v and J have been dropped because they do not have direct observable spectroscopic effect. The vibrational energy is the energy of a one dimensional quantum harmonic oscillator with

vibrational frequency depending on the vibrational state:

$$ {}^{v}\omega_V = \omega_e \left[1 - x_e \left(v + \frac{1}{2} \right) \right] \tag{3.45} $$

The adimensional parameter x_e takes into account the effect of anharmonic corrections on the vibrational frequency. In particular the vibrational frequency for the pure vibrational transitions between $v = 0$ and $v = 1$ is

$$ \omega_0 = \omega_e \left(1 - 2x_e \right) \tag{3.46} $$

The rotational energy is essentially the centrifugal energy with an effective v rotational constant ${}^{v}B$:

$$ {}^{v}B = B_e - \alpha_e \left(v + \frac{1}{2} \right) \tag{3.47} $$

where B_e is the momentum of inertia of a rigid molecule with internuclear distance r_e

$$ B_e = \frac{\hbar^2}{2\mu r_e^2} \tag{3.48} $$

and α_e is the lowest order vibration correction to the rotational constant. The term with coefficient D_e represents the lowest higher order centrifugal correction to the rotational energy. The relationships between the coefficients x_e, α_e and D_e and the molecular and potential parameters are given by [40, 3]

$$ x_e = -\frac{3}{4} \left[\frac{5 {g_e}^2}{4 {f_e}^2 \beta_e} - \frac{h_e}{f_e \beta_e} \right], \tag{3.49a} $$

$$ \alpha_e = \frac{3}{2} \frac{B_e^2}{\hbar \omega_e} \left[\frac{g_e r_e}{f_e} - 1 \right], \tag{3.49b} $$

$$ D_e = 4 \frac{B_e^3}{\left(\hbar \omega_e \right)^2}. \tag{3.49c} $$

according to perturbation theory applied to the vibration-rotation Hamiltonian equation (3.38). Table 3.1 reports the numerical values for the vibrational and rotational constants of free homonuclear hydrogen, H_2 and D_2, in the electronic ground state, obtained by matching the experimental frequency of spectroscopic data to equation (3.44). Specifically the numerical estimates for the coefficients f_e, g_e and h_e in H_2, equation (3.27), can be obtained from the values ω_e, $\omega_e x_e$ and α_e given in the tables by using the expressions equations (3.37b), (3.49a) and (3.49b).

	$\frac{\omega_e}{2\pi c}$ /cm^{-1}	$\frac{B_e}{hc}$ /cm^{-1}	$\frac{\omega_e x_e}{2\pi c}$ /cm^{-1}	$\frac{\alpha_e}{hc}$ /cm^{-1}	$\frac{D_e}{hc}$ /cm^{-1}	$\frac{^{0\text{-}1}\omega_V}{2\pi c}$ /cm^{-1}	r_e / Å	Δr_0 / Å
H_2	4395.2	60.80	117.9	2.99	0.05	4155.0[41]	0.741	0.07
D_2	3118.4	30.43	64.09	1.05	0.005	2994.0[41]	0.741	0.05

Table 3.1: Numerical values for the vibrational and rotational constants of free homonuclear hydrogen in the electronic ground state, adapted from [3]. All the values reported in the columns, except the last three, are obtained by matching the theoretical equation (3.44) with experiments. $^{0\text{-}1}\omega_V$ is the experimental frequency for the pure ground-state vibrational transition $|v = 0, J = 0\rangle \rightarrow |v = 1, J = 0\rangle$ obtained directly by Raman spectroscopy experiments. Δr_0 and r_e are calculated from the first two entries using equations (3.42), (3.43) and (3.48).

The conditions for the validity of the approximate solutions are given by [40]

$$\frac{\langle \Delta r \rangle_v}{r_e} << 1, \tag{3.50a}$$

$$\left[\frac{2B_e j(J+1)}{\hbar\omega_e}\right]^2 << 1, \tag{3.50b}$$

$$g_e \frac{\langle \Delta r \rangle_v}{f_e} << 1, \tag{3.50c}$$

$$h_e \frac{\langle \Delta r \rangle_v^{\,2}}{f_e} << 1, \tag{3.50d}$$

$$\frac{B_e}{\hbar\omega_e}\frac{g_e r_e}{f_e} << 1. \tag{3.50e}$$

The first inequality requires the spatial extension of the eigenstate to be small compared to the internuclear separation at equilibrium. The second inequality requires rotational energies to be small compared to the vibrational ones and ensure that higher order centrifugal corrections are small, $D_e << B_e$. The first two inequalities ensure that the vibrational and rotational motions are separable and it is possible to write the radial part of the wavefunctions of the three dimensional vibrating rotor as in equation (3.41). The third and the fourth inequalities ensure the validity of the harmonic approximation for the vibrational motion and that $x_e << 1$. The last inequality ensures that $\alpha_e << B_e$. The inequalities above fix implicitly the maximum values of the vibrational quanta and rotational quanta, v and J, for which the energy and wavefunctions of the Hamiltonian in equation (3.38) can be safely approximated by equation (3.39b) and equation (3.44), respectively. All these conditions are clearly satisfied for endohedral hydrogen fullerenes in the lowest vibrational-rotational states because the confinement induces only small changes in the internuclear potential parmeters with respect to the free molecule.

In summary the vibro-rotational Hamiltonian of hydrogen is approximately separable into a vibrational and a rotational part so that: a) the eigenstates can be written as $|v\rangle|J, M_J\rangle$, where $|v\rangle$ represents the radial wavefuncion in equation (3.41) and $|J, M_J\rangle$ represents a spherical harmonic, equation (3.40); b) the energy can be written as sum of the vibrational and rotational energy, equation (3.44).

3.3.1 Effective quantum Hamiltonian for the rotational-translational motion

In molecular hydrogen vibrations are characterized by higher frequencies than translations (and rotations). The coupling between vibrations and the other degrees of freedom is small compared to the separation in energy between vibrational states. The quantum motion of rotations and translations can be studied independently within each vibrational state. The interference among levels in different vibrational manifolds are negligible and can be included parametrically into an effective Hamiltonian. Specifically, at the level of approximation needed for the analysis of the available spectroscopic data of endohedral hydrogen fullerenes, the vibro-rotational Hamiltonian may be written as

$$ {}^{v}\mathcal{H}_{\text{V-R}} = E^{v}_{\text{V}} + {}^{v}\mathcal{H}_{\text{R}} \tag{3.51} $$

where the effective rotational Hamiltonian is

$$ {}^{v}\mathcal{H}_{\text{R}} = {}^{v}BJ^2 + D_e J^4. \tag{3.52} $$

As far as the translational motion is concerned, the molecule vibrates so fast that the potential experienced by the confined molecule is an average of the instantaneous potential over the vibrational eigenfunction:

$$ V^{\text{C}_{60}-\text{A}_2}(\boldsymbol{R}, \boldsymbol{r}) \rightarrow {}^{v}V^{\text{C}_{60}-\text{A}_2}(R, \Omega_{\boldsymbol{R}}, \Omega_{\boldsymbol{r}}) = \langle \psi^{v}_{\text{vib}}(r) | V^{\text{C}_{60}-\text{A}_2}(\boldsymbol{R}, \boldsymbol{r}) | \psi^{v}_{\text{vib}}(r) \rangle. \tag{3.53} $$

The dependence on the internuclear distance is eliminated through a quantum average over the vibrational state. The vibrationally averaged coefficients of the multipole expansion, equation (3.13), are defined as

$$ {}^{v}V^{lJ;n}_{00} = \langle \psi^{v}_{\text{vib}}(r) | V^{lJ;n}_{00}(r) | \psi^{v}_{\text{vib}}(r) \rangle. \tag{3.54} $$

It follows that, in a given vibrational state v, the translational Hamiltonian and the rotational-translational potential can be written as:

$$ {}^{v}\mathcal{H}_{\text{T}} = \underbrace{\frac{\boldsymbol{P}^2}{2M} + {}^{v}V^{00;2}_{00} R^2 F^{00}_{00}}_{{}^{v}\mathcal{H}^{Har}_{\text{T}}} + \underbrace{{}^{v}V^{00;4}_{00} R^4}_{{}^{v}\mathcal{H}^{An}_{\text{T}}}, \tag{3.55a} $$

$$ {}^{v}V_{\text{R-T}} = \left[{}^{v}V^{22;2}_{00} R^2 + {}^{v}V^{22;4}_{00} R^4 \right] F^{22}_{00}. \tag{3.55b} $$

The Hamiltonian for the coupled roto-translational (R-T) motion is reduced to a five dimensional Hamiltonian with a parametric dependence on the vibrational quantum num-

ber v:

$$ {}^{v}\mathcal{H}_{\text{R-T}} = {}^{v}\mathcal{H}_{\text{R}} + {}^{v}\mathcal{H}_{\text{T}} + {}^{v}V_{\text{R-T}} = \underbrace{{}^{v}\mathcal{H}_{\text{R}} + {}^{v}\mathcal{H}_{\text{T}}^{Har}}_{{}^{v}\mathcal{H}_{\text{R-T}}{}^{0}} + \underbrace{{}^{v}\mathcal{H}_{\text{T}}^{An} + {}^{v}V_{\text{R-T}}}_{{}^{v}\mathcal{H}_{\text{R-T}}{}^{1}} \tag{3.56} $$

The separation of ${}^{v}\mathcal{H}_{\text{R-T}}$ into a zero-order and a first-order term is made in view of a perturbative treatment of the coupled roto-translational quantum dynamics. In a given vibrational state, the endohedral hydrogen molecule behaves as a rotor with rotational constant ${}^{v}B$ moving in an external spherically symmetric potential. The full quantum Hamiltonian, comprehensive of the vibrational energy

$$ {}^{v}\mathcal{H} = E_{\text{V}}^{v} + {}^{v}\mathcal{H}_{\text{R-T}} \tag{3.57} $$

is diagonal in v since ${}^{v}\mathcal{H}_{\text{R-T}}$ does not mix vibrational states.

Zero-order rotation-translation Hamiltonian

The zero-order roto-translational quantum Hamiltonian is separable:

$$ {}^{v}\mathcal{H}_{\text{R-T}}{}^{0} = {}^{v}\mathcal{H}_{\text{R}} + {}^{v}\mathcal{H}_{\text{T}}^{Har} \tag{3.58} $$

The eigenstates, the energies and the degeneracies of the rotation Hamiltonian have been discussed in 3.3. The harmonic part of the effective Hamiltonian ${}^{v}\mathcal{H}_{\text{T}}$ is the starting point for the analysis of the translational motion. The quantum Hamiltonian for the motion in an isotropic harmonic potential with frequency ${}^{v}\omega_{T}$ is given by

$$ {}^{v}\mathcal{H}_{\text{T}}^{Har} = \frac{\boldsymbol{P}^2}{2M} + {}^{v}V_{00}^{00;2} R^2 F_{00}^{00} = -\frac{\hbar^2}{2M} R \frac{\partial^2}{\partial^2 R} \frac{1}{R} + \frac{1}{2} M {}^{v}\omega_{T}{}^{2} R^2 + \frac{\hbar^2 \hat{\boldsymbol{L}}^2}{2MR^2} \tag{3.59} $$

where $\{R, \Theta, \Phi\}$ are spherical coordinates for the center of mass vector and the oscillation frequency is given by

$$ {}^{v}\omega_{T} = \sqrt{\frac{{}^{v}V_{00}^{00;2}}{2\pi M}}. \tag{3.60} $$

The spherical symmetry allows one to find exact eigenvalues and eigenvectors

$$ {}^{v}\mathcal{H}_{\text{T}}^{Har}\, {}^{v}\psi_{\text{T}}^{N,L,M_L}(R,\Theta,\Phi) = {}^{v}E_{\text{T}}^{N}\, {}^{v}\psi_{\text{T}}^{N,L,M_L}(R,\Theta,\Phi) \tag{3.61a} $$

$$ {}^{v}\psi_{\text{T}}^{N,L,M_L}(R,\Theta,\Phi) = \underbrace{{}^{v}\psi_{\text{tran}}^{N,L}(R)}_{\text{radial}}\, \underbrace{Y_{LM_L}(\Theta,\Phi)}_{\text{angular}}. \tag{3.61b} $$

The angular part of the eigenfunction is given by spherical harmonics: $|L, M_L\rangle = Y_{LM_L}(\Theta,\Phi)$. The integer quantum numbers L and M_L define the quantum angular momentum for rotations of the center of mass vector with respect to the center of the fullerene. The quantum number N is a positive or null integer labelling the radial part of the wavefunctions together with L. For a given N, the quantum number L is re-

stricted to be in the range $L = N, N-2, \ldots, 1$ or 0 depending on N being odd or even, respectively. Explicitly the normalized radial part of the eigenfunctions is given by[42]:

$$|N, L; v\rangle = {}^{v}\psi^{N,L}_{\text{tran}}(R) = \zeta\left(N_f, L_f, {}^{v}\beta_T\right)({}^{v}\beta_T R^2)^{\frac{L}{2}} \mathrm{e}^{-\frac{{}^{v}\beta_T R^2}{2}} \mathtt{La}^{L+\frac{1}{2}}_{\frac{N-L}{2}}({}^{v}\beta_T R^2) \tag{3.62}$$

where

$$\zeta\left(N_f, L_f, {}^{v}\beta_T\right) = 2^{\frac{1}{2}} \frac{\left[(\frac{N-L}{2})!\right]^{1/2}}{\left[(\frac{N+L+1}{2})!\right]^{3/2}} {}^{v}\beta_T{}^{\frac{3}{4}} \tag{3.63}$$

is the normalization factor and ${}^{v}\beta_T = \frac{M^{v}\omega_T}{\hbar}$ determines the length scale of the system. Here $\mathtt{La}^{\alpha}_{n}(x)$ are the generalized Laguerre polynomials, [36]. Explicitly $\mathtt{La}^{\alpha}_{0}(x) = 1$ and $\mathtt{La}^{\alpha}_{0}(x) = \alpha + 1/2 - x$ for any $\alpha > -1$. The energy for the harmonic translational motion is given by:

$${}^{v}E^{N}_{\text{T}} = \hbar{}^{v}\omega_T\left(N + \frac{3}{2}\right). \tag{3.64}$$

The spatial degeneracy of the translational energy levels is $(N+1)(N+2)/2$.

The eigenstates of the zero-order Hamiltonian in equation (3.58) are exactly given by

$$|N, L, M_L, J, M_J; v\rangle = |J, M_J\rangle|N, L, M_L; v\rangle \otimes |J, M_J\rangle \tag{3.65}$$

with energy

$${}^{v}E^{J,N}_{\text{R-T;0}} = {}^{v}B\, J(J+1) + D_e\, [J(J+1)]^2 + \hbar{}^{v}\omega_T\left(N + \frac{3}{2}\right). \tag{3.66}$$

The degeneracy of the energy level is the product of the rotation and translation degeneracies: $(2J+1)(N+1)(N+2)/2$.

Coupled basis for rotation-translation motion

Separating the full Hamiltonian into a zero-order part and a first-order part allows one to use perturbative method to study the dynamics of the system. Eigenstates and eigenvalues of the full Hamiltonian can be connected to the ones of the zero-order unperturbed Hamiltonian. To evaluate the energy for the full Hamiltonian one needs an explicit matrix representation of the perturbative Hamiltonian in a parental basis. The choice of the basis used to study the quantum dynamics of a system is a matter of convenience. The best choice is to reorganize the basis of the zero-order Hamiltonian in order to exploit the symmetry of the full system. The advantage is that the matrix representation of the full Hamiltonian becomes block-diagonal according to the (irreducible) representation of its symmetry group: the matrix elements between states belonging to different representation are exactly zero. Since the endohedral potential for C_{60} is spherical to a good approximation, it is no surprise that the total orbital angular momentum of the endohedral hydrogen molecule $\hat{\mathbf{\Lambda}} = \hat{\boldsymbol{L}} + \hat{\boldsymbol{J}}$ provides approximate good quantum num-

bers (exact in spherical symmetry) for the eigenstates of the coupled rotation-translation Hamiltonian. The quantum dynamics of rotation-translation is then better analyzed in the following basis of eigenstates of $\hat{\mathbf{\Lambda}}$:

$$|N, L, J, \Lambda, M_\Lambda; v\rangle \stackrel{\text{def}}{=} {}^{v}\psi^{N,L}_{\text{tran}}(R)\, F^{LJ}_{\Lambda M_\Lambda}(\Theta, \Phi, \theta, \phi). \tag{3.67}$$

ψ_{tran} is given by equation (3.62) and the bipolar spherical harmonics F are discussed in section 2.4. All the quantum numbers are positive or null integers. For a given L and J the quantum number Λ is an integer within the range $|L-J| \leq \Lambda \leq L+J$ and $|M_\Lambda| \leq \Lambda$, according to the general theory of angular momentum. The limitation on the values of L with respect to N was discussed in the previous section. In the coupled basis the zero-order roto-translation Hamiltonian is diagonal. Another reason for using the coupled basis equation (3.67) is that molecular hydrogen is characterized by large rotational constants compared to translation-rotation coupling so that J is an approximate good quantum number for the endohedral hydrogen.

Since the translational anharmonic potential and the roto-translational potential are sums of terms each proportional to $R^k F^{LJ}_{00}$, the matrix elements between initial and final spherical states $|f; v_f\rangle$ and $|i; v_i\rangle$ (neglecting the spin part) are given by

$$\langle f|R^k F^{lj}_{00}|i\rangle = \underbrace{\langle N_f, L_f; v_f|R^k|N_i, L_i; v_i\rangle}_{\text{radial}} \underbrace{\langle L_f, J_f, \Lambda_f, M_{\Lambda f}|F^{lj}_{00}|L_i, J_i, \Lambda_i, M_{\Lambda i}\rangle}_{\text{angular}}. \tag{3.68}$$

Both the radial and the angular matrix elements reduce to algebraic factors. The evaluation of the matrix elements for the bipolar spherical harmonics in the coupled basis has been discussed in 2.4. The radial matrix element can be expressed after expanding the product of two Laguerre polynomials as

$$\begin{aligned}\langle N_f, L_f; v_f|R^k|N_i, L_i; v_i\rangle = {} & \frac{1}{2}\zeta\left(N_f, L_f, {}^{v_f}\beta_T\right)\zeta\left(N_i, L_i, {}^{v_i}\beta_T\right) \\ & \times\left(\frac{1}{{}^{v_i}\beta_T}\right)^{\frac{k+3}{2}}\left(\frac{{}^{v_f}\beta_T}{{}^{v_i}\beta_T}\right)^{\frac{L_f}{2}}\left(\frac{2}{1+\frac{{}^{v_f}\beta_T}{{}^{v_i}\beta_T}}\right)^{\frac{L_f+L_i+k+3}{2}} \\ \times\sum_{r=0}^{\frac{N_f-L_f}{2}}\sum_{s=0}^{\frac{N_i-L_i}{2}} & \frac{1}{r!s!}\binom{\frac{N_f+L_f+1}{2}}{\frac{N_f-L_f}{2}-r}\binom{\frac{N_i+L_i+1}{2}}{\frac{N_i-L_i}{2}-s}\left(\frac{{}^{v_f}\beta_T}{{}^{v_i}\beta_T}\right)^r\left(-\frac{2}{1+\frac{{}^{v_f}\beta_T}{{}^{v_i}\beta_T}}\right)^{r+s}\Gamma\left(r+s+\frac{L_f+L_i+k+3}{2}\right)\end{aligned} \tag{3.69}$$

where the round paratheses contain binomial coefficients and Γ is the standard gamma function [36]. This last formula is cumbersome but it is reported here because it is completely algebraic and it can be applied to states with ${}^{v_f}\beta_T \neq {}^{v_i}\beta_T$ compared to the one in [43].

Effect of the exclusion principle

The full quantum state of the nuclear wave-function is defined by (a linear combination of) the product of a space part and a spin part according to:

$$\psi_{\text{nuclear}} = \psi_{\text{space}}\psi_{\text{spin}}. \tag{3.70}$$

The quantum dynamics of homonuclear molecules is affected by the spin of its constituents according to the Pauli principle. The total wavefunctions describing a quantum system has a definite parity P, either +1 or -1, by exchange of the (space and spin) coordinates of any pair of identical constituents:

$$\Psi(\boldsymbol{x}_1, \boldsymbol{x}_2, \ldots) = P\,\Psi(\boldsymbol{x}_2, \boldsymbol{x}_1, \ldots). \tag{3.71}$$

The Pauli exclusion principle links the parity of a quantum system to the spin of the identical particles whose coordinates are exchanged: the parity must be -1 (and the wave-function is said antisymmetric) if the exchanged particles have half-integer spin (fermions) while the parity is +1 (and the wave-function is said symmetric) if the exchanged particles have integer spin (bosons). In an electronic state with zero electronic spin and zero electronic angular momentum, such as the ground electronic state of hydrogen, the parity of the molecular wavefuntion is determined by the parity of the nuclear wave-functions only [44], which is given by the product of the parities of the space and spin kets. As for the space part of nuclear wave-functions, the exchange of coordinates of the two nuclei corresponds to the following transformation of spherical coordinates

$$\{R, \Theta, \Phi, \theta, \phi\} \rightarrow \{R, \Theta, \Phi, \pi - \theta, 2\pi - \phi\} \tag{3.72}$$

so that the parity of the space ket, equation (3.67), is $P = (-1)^J$. For the spin ket of homonuclear diatomic molecules the parity by exchange of the spin coordinates is $(-1)^I$. It follows that:

- since acceptable wavefunctions for H_2 must have $P = -1$ by exchange of the two protons (^{1}H has spin 1/2) the allowed ket for the space part has J = even for para-H_2 ($I = 0$), and J = odd for ortho-H_2 ($I = 1$);

- since acceptable wavefunctions for D_2 must have $P = -1$ by exchange of the two deuterons (^{2}H has spin 1) the allowed ket for the space part has J = even for ortho-H_2 ($I = 2, 0$), and J = odd for para-D_2 ($I = 1$).

Within a given electronic state no mixing between states with even and odd J is allowed. Ortho and para isomers can be studied independently using the space part of the kets since the Hamiltonian of the spatial degrees of freedom does not contain spin operators explicitly.

3.3.2 Energy level strucure

For free hydrogen each of the discrete vibrational-rotational levels, described by equation (3.44), is flanked by a continuous set of infinitely degenerate translational energy levels. In the confined geometry the set of translational energy levels becomes quantized leaving only a discrete set of translational levels with finite degeneracy. The separation between consecutive translational energy levels is related to the strength of the confinement: the more the center of mass gets localized the more the sparseness of the energy levels increases. For isotropic harmonic confinement, the translational levels are uniformly spaced with a separation of $\hbar^v\omega_T$. In presence of small anharmonicities and rotation-translation coupling, the spacing is no longer uniform and each vibration-rotation-translation level $|v, J, N, L\rangle$ is split into a multiplet. The number of components of a given multiplet is

$$\#(J,N,L) = \begin{cases} \frac{(N+1)(N+2)}{2} \text{ if } J \geq N \\ \frac{(N+1)(N+2)-(N-L+1)^2}{2} - \text{ if } J < N \text{ and } N-J = \text{odd} \\ \frac{(N+1)(N+2)-(N-L+1)^2-1}{2} - \text{ if } J < N \text{ and } N-J = \text{even} \end{cases} \tag{3.73}$$

In the spherical approximation, each level in the multiplet has a degeneracy $g = 2\Lambda + 1$ depending only on the total orbital angular momentum. Each spherical level has a finer structure when the real icosahedral symmetry is taken into account according to the irreducible representations of the I_h group. In the homonuclear case ortho and para energy levels form separate manifolds. This situation is illustrated in figure 3.4 with reference to the lowest rotational energy level of ortho-hydrogen, $J = 1$.

The energy separations together with the splittings and the ordering of Λ for a given multiplet can be obtained by diagonalization of the translation-rotation Hamiltonian in the basis defined by equation (3.67). The numerical procedure is to build and diagonalize a finite-dimensional matrix representation of the Hamiltonian over the coupled basis with $J \leq J_{\max}$ and $N \leq N_{\max}$ for some chosen $J_{\max}$ and $N_{\max}$ and keep increasing the size of the basis until some convergence criteria are satisfied. The spherical symmetry reduces greatly the size of the ortho and para matrices to be evaluated: because of the degeneracy on M_Λ the size of the Hamiltonian coincides with the number of components of the multiplets. The Hamiltonian matrix reduces to block diagonal form, each block labeled by the total angular momentum of the states. For example, good starting values are $N_{\max} = 2$ with $J_{\max} = 3$ for ortho hydrogen and $J_{\max} = 2$ for para-hydrogen, respectively. Within such values there are 100 ortho states and 60 para states but the Hamiltonian matrices to diagonalize have reduced sizes 18×18 and 14×14 respectively. The ortho Hamiltonian is formed by six diagonal blocks, each with $\Lambda = 0, \ldots, 5$ and sizes $1, 5, 4, 5, 2, 1$ respectively; the para Hamiltonian has 5 diagonal blocks, each with $\Lambda = 0, \ldots, 4$ and sizes $3, 3, 5, 2, 1$ respectively.

In conclusion a given energy sublevel $|i, M_{\Lambda i}\rangle$ with angular momentum Λ_i is written

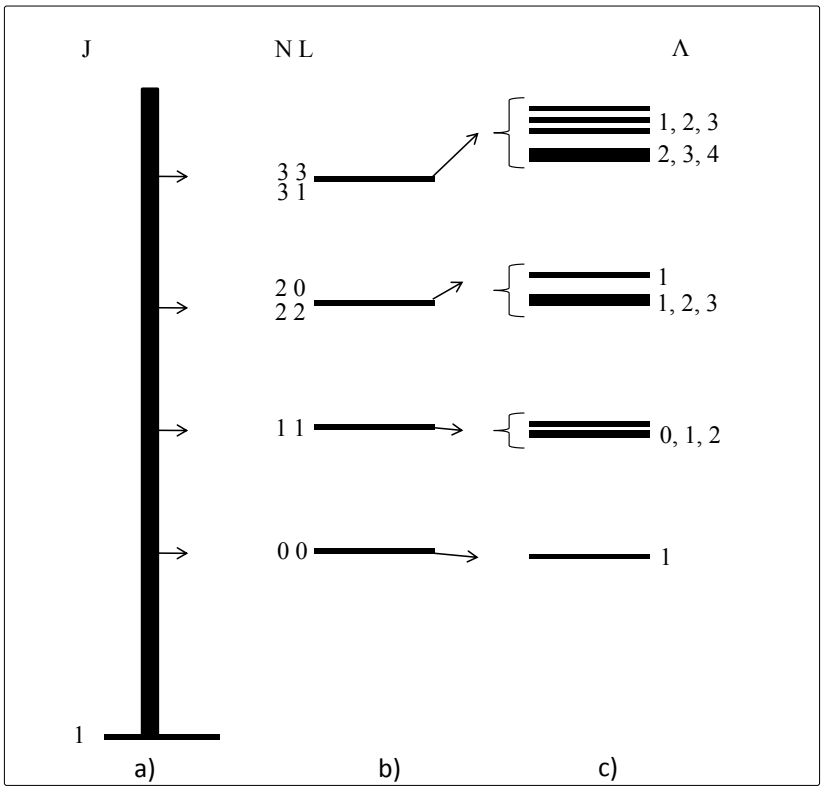

Figure 3.4: Increasing complexity in the structure of the energy levels of a confined hydrogen molecule. The figure refers specifically to the energy levels of ortho-H_2 in the rotational state $J = 1$. a) Free hydrogen: the continuum of (infinitely degenerate) translational levels is represented by a vertical line; b) Hydrogen in harmonic isotropic confinement: the quantized translational levels are labeled by the number of translational quanta N and the relative orbital angular momentum L. The energy of the lowest level is shifted upward because of the zero point energy of the confined state. The spacings between the levels is uniform. Each level is finitely degenerate; c) Translational states are split into multiplets when anharmonic terms and rotation-translation coupling are considered, according to equation (3.73). The levels in a multiplet are labeled by the total angular momentum Λ. The order of Λ in a given multiplet depends on the specific form of the coupling potential. The effect of icosahedral symmetry (not shown here) is to lift the degeneracy for levels with $\Lambda \geq 3$.

in the spherical basis as

$$|i, M_{\Lambda i}\rangle = \sum_{J_a,N_a,L_a} {}^{v}c_{J_a,N_a,L_a} |N_a, L_a, J_a, \Lambda_i, M_{\Lambda i}\rangle \tag{3.74}$$

where the sum extends up to $L \leq N \leq N_{\max}$ and $J \leq J_{\max}$. The coefficients ${}^{v}c_{J_a,N_a,L_a}$ are obtained by diagonalizing the translational-rotational Hamiltonian and are functions of the parameters specifying the dynamics in the vibrational state v. For homonuclear hydrogen in C_{60} these parameters are: ω_e, x_e, B_e, α_e, D_e, ${}^{v}V_{00}^{00;2}$, ${}^{v}V_{00}^{00;4}$, ${}^{v}V_{00}^{22;2}$, ${}^{v}V_{00}^{22;4}$ as explained in sections 3.3 and 3.3.1.

Chapter 4

Infrared spectroscopy of dihydrogen fullerenes

While heteronuclear diatomic molecules are infrared-active because of the permanent electric dipole moment it may be surprising that a homonuclear diatomic molecule like hydrogen is infrared-active at all. However, the interactions with atoms or molecules can produce small distortions of the molecular charge distribution so inducing a small dipole moment. For example IR activity is induced in molecular hydrogen in the gas phase [45] by collisions and in the condensed phase [46] by interactions between molecules. The theoretical background for the interpretation of collision-induced IR spectra in hydrogen has been laid by van Kranendonk et al. in several papers [47, 48, 49]. More recently, IR spectroscopy of H_2 intercalated in the the voids among the cages in crystalline C_{60} has been reported [50, 51, 52]. A rigorous treatment requires ab initio evaluation of three main induction mechanisms (dispersion, electron exchange, and electric multipolar) in a similar way to that done for H_2-noble gas systems [53, 54]. In the following section the attention will be focused on the electric dipole for hydrogen in C_{60}. Symmetry arguments will be combined with considerations about the mechanism inducing an electric dipole moment to determine selection rules and absorption coefficients in the homonuclear case.

4.1 Induced dipole moment in endohedral fullerene

A quantitative analysis of the induced IR activity can be performed by expanding the instantaneous dipole moment, which is a function of the configuration coordinates of the endohedral molecule, in terms of appropriate spherical multipoles as described below. Remaining in the spherical approximation of the C_{60} cage, symmetry arguments imply

an expansion of the dipole moment in terms of bispherical harmonics of rank one [55]:

$$\begin{aligned}\mu_q(\boldsymbol{R},\boldsymbol{r}) &= \frac{4\pi}{\sqrt{3}}\sum_{l,j} A^{lj}(R,r)\, F^{lj}_{1q}(\Theta,\Phi,\theta,\phi) \\ &= \frac{4\pi}{\sqrt{3}}\sum_{l,j}\sum_{n} A^{lj;n}(r)\, R^n F^{lj}_{1q}(\Theta,\Phi,\theta,\phi),\end{aligned} \tag{4.1}$$

independently of any microscopic fundamental mechanism inducing the dipole moment. In the second line an expansion of the coefficients A^{lj} in powers of R was used. There are restrictions on the allowed l, j and n values entering in the multipole expansion:

- in general n is a positive or null integer which is even for l even and odd for l odd;
- $j + l$ must be odd. More precisely $l = j \pm 1$ from the triangle relation;
- for homonuclear molecules $\mu_q(\boldsymbol{R},-\boldsymbol{r})$=$\mu_q(\boldsymbol{R},\boldsymbol{r})$ and only even j terms are allowed;
- it follows that only odd powers n are allowed in the expansion above for homonuclear molecules.

Let us note that $\mu_q(0,\boldsymbol{r}) = 0$ for a homonuclear diatomic molecule in C_{60} because of symmetry under inversion.

The dipole moment induced by the interaction of the hydrogen molecule with C_{60} can be thought as a sum, over all the 60 atoms, of the two body carbon-hydrogen induced dipole moment. In a system of reference with origin in the center of the fullerene the dipole moment induced by the $i-$th carbon atom can be written in terms of bispherical harmonics:

$$\mu_{i,q}(\boldsymbol{R},\boldsymbol{r}) = \frac{4\pi}{\sqrt{3}}\sum_{l,j} B_{lj}(|\boldsymbol{R}-\boldsymbol{s}_i|,r)\, F^{lj}_{1q}(\Omega_{\boldsymbol{R}-\boldsymbol{s}_i},\Omega_{\boldsymbol{r}}) \tag{4.2}$$

where $\boldsymbol{s}_i$ is the vector pointing to the given carbon atom and $\Omega_{\boldsymbol{R}-\boldsymbol{s}_i}$ and $\Omega_{\boldsymbol{r}}$ are the polar angles of the subscripted vectors (in the given reference frame), see figure 3.1. The sum runs over the integer indices l and j with the same restrictions given above for the full dipole moment. The induced dipole moment to first-order in the displacement R from

the center of the cage is

$$\begin{aligned}
\mu_q(\boldsymbol{R},\boldsymbol{r}) &= \sum_{i=1}^{60}\mu_{i,q}(\boldsymbol{R},\boldsymbol{r}) \approx \sum_{i=1}^{60}\frac{4\pi}{\sqrt{3}}\sum_{l,j}\boldsymbol{R}\cdot\nabla_{\boldsymbol{R}}\left[B_{lj}\left(|\boldsymbol{R}-\boldsymbol{s}_i|,r\right)F_{1q}^{lj}\left(\Omega_{\boldsymbol{R}-\boldsymbol{s}_i},\Omega_{\boldsymbol{r}}\right)\right]_{\boldsymbol{R}=0} \\
&= \frac{4\pi}{\sqrt{3}}\boldsymbol{R}\cdot\sum_{i=1}^{60}\sum_{l,j}\nabla_{-\boldsymbol{s}_i}\left[B_{lj}\left(|-\boldsymbol{s}_i|,r\right)F_{1q}^{lj}\left(\Omega_{-\boldsymbol{s}_i},\Omega_{\boldsymbol{r}}\right)\right] \\
&= \frac{4\pi}{\sqrt{3}}\sum_{l,j}\frac{60}{4\pi}\boldsymbol{R}\cdot\int \mathrm{d}\Omega_{\boldsymbol{s}}\,\nabla_{\boldsymbol{s}}\left[B_{lj}\left(|\boldsymbol{s}|,r\right)F_{1q}^{lj}\left(\Omega_{\boldsymbol{s}},\Omega_{\boldsymbol{r}}\right)\right] \\
&= \frac{4\pi}{\sqrt{3}}\sum_{j=0,2}\underbrace{20R\left[\frac{\partial B_{1j}(s,r)}{\partial s}+\frac{2}{s}B_{1j}(s,r)\right]_{s=R_{\mathrm{C}_{60}}}}_{A^{1j}(R,r)}.
\end{aligned} \tag{4.3}$$

having exchanged the gradient on $\boldsymbol{R}$ with the gradient on $-\boldsymbol{s}_i$ in the second step and having replaced the sum over the carbon atoms by an integral (spherical approximation) in the third equality. The last equality has been obtained using the spherical tensor formulation of the scalar product and the explicit form of the spherical components of the gradient of bispherical harmonics [29]. This derivation shows that the multipole expansion of the induced dipole moment at first-order in R contains only two terms: A^{1j} with $j = 0, 2$.

4.1.1 Selection rules and transition probabilities for electric dipole transitions

Electric dipole transitions are organized in vibrational bands labeled by the initial and final vibrational quantum numbers: v_f-v_i. The dipole moment for a transition in the band v_f-v_i is defined by

$$\mu_q^{v_f\text{-}v_i} \stackrel{\text{def}}{=} \langle v_f|\mu_q|v_i\rangle \tag{4.4}$$

and can be expanded as in equation (4.1) with the replacements

$$A^{lj} \to \overline{A}^{lj}_{v_f\text{-}v_i}(R) \stackrel{\text{def}}{=} \langle\psi^{v_f}_{\text{vib}}(r)|A^{lj}(R,r)|\psi^{v_i}_{\text{vib}}(r)\rangle \tag{4.5a}$$

$$A^{lj;n} \to \overline{A}^{lj;n}_{v_f\text{-}v_i} \stackrel{\text{def}}{=} \langle\psi^{v_f}_{\text{vib}}(r)|A^{lj;n}(r)|\psi^{v_i}_{\text{vib}}(r)\rangle \tag{4.5b}$$

The dependence on the internuclear distance is absorbed into a parametric dependence on the vibrational quantum numbers.

It is worth exploring how symmetry introduces selection rules based on the multipole expansion in the case of hydrogen confined in an isotropic harmonic potential. The

energy levels are written in the coupled spherical basis as

$$|a, m_a\rangle = |J_a, N_a, L_a, \Lambda_a, M_{\Lambda a}; v_a\rangle |I_a, M_{Ia}\rangle, \tag{4.6}$$

$$|b, m_b\rangle = |J_b, N_b, L_b, \Lambda_b, M_{\Lambda b}; v_b\rangle |I_b, M_{Ib}\rangle, \tag{4.7}$$

where I and M_I are explicit spin quantum numbers and the levels are degenerate in the projection quantum numbers $m = \{M_\Lambda, M_I\}$. The dependence on the vibrational quantum number is parametric. Using the Wigner-Eckart theorem the matrix element of the dipole moment, equation (4.4), can be written as

$$\langle a, m_a|\mu_q^{v_b\text{-}v_a}|b, m_b\rangle = \underbrace{\delta_{I_b,I_a}\delta_{M_{Ib},M_{Ia}}}_{\text{spin}}(-1)^{\Lambda_b - M_{\Lambda b}}\begin{pmatrix}\Lambda_b & 1 & \Lambda_a\\ -M_{\Lambda b} & q & M_{\Lambda a}\end{pmatrix} \times \langle N_b, L_b, J_b, \Lambda_b; v_b||\mu^{v_b\text{-}v_a}||N_a, L_a, J_a, \Lambda_a; v_a\rangle \tag{4.8}$$

where the reduced matrix element is

$$\langle N_b, L_b, J_b, \Lambda_b; v_b||\mu^{v_b\text{-}v_a}||N_a, L_a, J_a, \Lambda_a; v_a\rangle = \frac{4\pi}{\sqrt{3}}\sum_{l,j,n}\overline{A}^{lj;n}_{v_b\text{-}v_a}\underbrace{\langle N_b, L_b; v_b|R^n|N_a, L_a; v_a\rangle}_{\text{radial}} \times \underbrace{\langle L_b, J_b, \Lambda_b||F_1^{lj}||L_a, J_a, \Lambda_a\rangle}_{\text{angular}}. \tag{4.9}$$

The spin selection rule $\Delta I = 0$ follows from the independence of the multipolar expansion on spin operators. It states that electric dipole transitions between spin isomers are forbidden and IR spectroscopy can probe ortho and para species separately. The selection rule on the total angular momentum $\Delta\Lambda = 0, \pm 1$ is determined by the property of the 3-j symbol. It states that a maximum change of one unity is allowed for dipole transitions. The radial integral is a complicated algebraic expression, see equation (3.69). The angular integral in equation (4.9) is given by

$$\text{angular} = [3(2l+1)(2j+1)]^{\frac{1}{2}} \times \begin{Bmatrix} L_b & L_a & l\\ J_b & J_a & j\\ \Lambda_b & \Lambda_a & 1\end{Bmatrix}\langle L_b||T^l\left(\hat{Y}\right)||L_a\rangle\langle J_b||T^j\left(\hat{Y}\right)||J_a\rangle \tag{4.10}$$

according to equations (2.56) and (2.57). The selection rules $|\Delta L| =$ odd and $|\Delta J| =$ even for homonuclear molecules follows from the reduced matrix elements of spherical harmonics,equation (2.55), being l odd and j even. Since L is odd or even according to N being odd or even it follows also that $|\Delta N| =$ odd.

Using the expansion of the dipole moment at first-order in $\boldsymbol{R}$, the selection rules on L and J become more restrictive: $\Delta L = \pm 1$ and $\Delta J = 0, \pm 2$. The selection rule on the translation quantum number becomes $\Delta N = \pm 1$ if the translational frequencies in the initial and final vibrational states do not differ much. This can be seen from the fact that

the dipole coefficients are $\propto R$, equation (4.3), and the radial integral simplifies to

$$\langle N+\Delta N, L+\Delta L; {}^{v_f}\beta_T|R|N, L; {}^{v_i}\beta_T\rangle = \sqrt{\frac{1}{2^{v_i}\beta_T}}\Big[-\delta_{\Delta N\Delta L,1}\,(N+L+\Delta N+2)^{\frac{1}{2}} + \delta_{\Delta N\Delta L,-1}\,(N-L+\Delta N+1)^{\frac{1}{2}}\Big] \tag{4.11}$$

when ${}^{v_f}\beta_T \approx {}^{v_i}\beta_T$ [43].

In general anharmonic corrections to the translational potential and translational-rotational interactions imply that the energy levels are linear combination of the isotropic oscillator states. In spherical symmetry the energy levels are still spherical states and the total angular momentum is a good quantum number. The Wigner-Eckart theorem can be applied to evaluate vibrational transition probabilities. In particular the probability of transition between an initial level $|i\rangle$ and final level $|f\rangle$ is given by the sum of the square of the electric dipole matrix element over the projection quantum numbers and the polarization:

$$\sum_{\substack{q\\ M_{If},M_{Ii}\\ M_{\Lambda f},M_{\Lambda i}}} \left|\langle f; M_{\Lambda f}, M_{If}|\mu_q|i; M_{\Lambda i}, M_{Ii}\rangle\right|^2 = \delta_{I_f,I_i}\,(2I_i+1)\,|\langle f||\mu||i\rangle|^2 \tag{4.12}$$

where

$$|\langle f||\mu||i\rangle|^2 = \left|\sum_{\substack{N_b,L_b,J_b\\ N_a,L_a,J_a}} {}^{v_f}c^*_{N_b,L_b,J_b}\,{}^{v_i}c_{N_a,L_a,J_a}\langle N_b, L_b, J_b, \Lambda_f; v_f||\mu^{v_f\text{-}v_i}||N_a, L_a, J_a, \Lambda_i; v_i\rangle\right|^2 \tag{4.13}$$

The transition probability for unpolarized light does not have any specific directional dependence as expected from the complete spherical symmetry of the system.

4.1.2 Integrated absorption for endohedral hydrogen fullerene

In this section the integrated absorption for infrared optical transitions in endohedral hydrogen fullerene is derived. In the following discussion the incident light will be supposed to be unpolarized and the sample to be a homogeneous dielectric characterized by a frequency-independent refraction index η.

In a typical infrared experiment the intensity of a light beam passing through a sample, intended as the energy falling on the detector in the unit of time, is compared to that of the incident beam: at specific frequencies the amount of light passing through the sample is reduced owing to absorption phenomena in the material. Such a reduction is quantified by the absorbed intensity I^{abs}, defined as the difference between the intensity of the incident beam and that of the through beam. For a thin layer of material the absorption coefficient is rewritten in terms of fraction of absorbed intensity (over the

incident beam intensity) divided by the sample thickness δ:

$$\alpha(\omega) \stackrel{\text{def}}{=} -\frac{1}{\delta}\ln\frac{I_\delta(\omega)}{I_0(\omega)} \approx \frac{1}{\delta}\frac{I_0(\omega)-I_\delta(\omega)}{I_0(\omega)} = \frac{1}{\delta}\frac{I_\delta^{\text{abs}}(\omega)}{I_0(\omega)}. \tag{4.14}$$

Here I_δ is the intensity of light reaching the detector after passing through the sample. Obviously the intensity of the beam incident on the sample coincides with the zero thickness intensity $I_0(\omega)$. In any experimental situations broadening mechanisms ensures that absorption peaks are not infinitely narrow but have a finite width. The physical quantity of interest is the integrated absorption, i.e. the integral of the absorption coefficients over a specified frequency interval R containing the peak of interest

$$S_R = \int_R \mathrm{d}\omega\,\alpha(\omega). \tag{4.15}$$

The absorption process can be understood at a microscopic level by considering the detailed energy transfers under stationary conditions: 1) some energy is absorbed by the sample at frequencies which correspond to transitions between energy levels of the system and 2) some energy is re-emitted by the sample with the same characteristic of the incident beam (stimulated emission). The energy removed from the beam is given by the difference of the two processes above and at last is either radiated out by spontaneous emission or absorbed by the material through non-radiative processes. Einstein coefficients link the microscopic description of light-matter interaction to the macroscopic absorption coefficients. Consider two energy levels, i and a final f, of the material quantum system with energy $E_f > E_i$. Observing that the amount of energy per unit of time lost by the through beam coincides with the intensity of absorbed light one has [56]

$$I_\delta^{\text{abs}}(\omega_{fi}) = \left(B_{f\leftarrow i}N_i^V - B_{i\leftarrow f}N_f^V\right)W(\omega_{fi})\hbar\omega_{fi} \tag{4.16}$$

where N_i^V (N_f^V) are the number of particles contained in the volume $V = s\,\delta$ that are in the quantum state i (f) and $\hbar\omega_{fi} = E_f - E_i$ is the energy of the absorbed photon. $B_{f\leftarrow i}$ and $B_{i\leftarrow f}$ are the Einstein coefficients, absorption and stimulated emission, for the transition between the given energy levels, $W(\omega)$ is the energy density per unit of frequency of the radiation in the dielectric: their product gives the number of transitions per unit of time. The energy density in the incident beam is $W_0(\omega)$=$W(\omega)/\eta$. Assuming for sake of simplicity that the incident beam has a constant intensity I_0 over the spectral region $\Delta\omega$ larger than the extension of the peak, the energy density of the incident beam is $W_0(\omega) = I_0/(cs\Delta\omega)$. $N_f^V << N_i^V$ for all the transitions involved in the IR experiments discussed later and stimulated emission is completely negligible. It follows that the absorbed intensity for the considered transition can be written as

$$I_\delta^{\text{abs}}(\omega_{fi}) = \delta\,\frac{N_i^V}{V}B_{f\leftarrow i}\frac{I_0}{c\eta\Delta\omega}\hbar\omega_{fi}. \tag{4.17}$$

Consequently the absorption area $S_{f,i}$ is

$$S_{f,i} = \frac{d_N}{c\eta} P_i(T) B_{f\leftarrow i} \hbar\omega_{fi} \tag{4.18}$$

where it is assumed that the peak is narrow and where $d_N = N/V$ is the numeric density of absorption centers and $P_i(T)$ is the equilibrium thermal population of the energy level i (g_i being its degeneracy):

$$P_i(T) = \frac{g_i e^{-\frac{E_i}{k_B T}}}{\sum_m g_m e^{-\frac{E_m}{k_B T}}}. \tag{4.19}$$

The Einstein coefficients depend on the physical mechanism determining the absorption of light. They determine how well a pair of energy level of the system is coupled to a resonant electromagnetic field. For dipole transitions between a g_i-fold degenerate initial level and a g_f-fold degenerate final level [57]

$$B_{f\leftarrow i} = \frac{\pi}{3\varepsilon_0\hbar^2} \sum_q \sum_{m_f,m_i} \frac{|\langle f, m_f|\mu_q|i, m_i\rangle|^2}{g_i} \tag{4.20}$$

where μ_q is the $q = -1, 0, 1$ spherical component of the electric dipole moment in the SI system. The indices m_f and m_i represents a set of quantum numbers distinguishing the states in the degenerate levels. All these states contribute to the line at the frequency ω_{fi}. The sum over the components q depends on the fact that the light is supposed to be unpolarized. Finally the matrix element of the electric dipole moment determines which transitions are IR active.

Using equations (4.19), (4.20) and (4.12) the theoretical absorption area, equation (4.18), for a vibrational transition in endohedral fullerene can be written as

$$S^k_{f,i} = \delta_{I_f,I_i} \frac{\pi d_N}{3\varepsilon_0\hbar c\eta} n_k \omega_{fi} \frac{e^{-\frac{E_i}{k_B T}}}{\sum_m (2\Lambda_m + 1) e^{-\frac{E_m}{k_B T}}} |\langle f||\mu||i\rangle|^2 \tag{4.21}$$

where the index k is used to distinguish between ortho and para transitions in the homonuclear case. n_k is the fraction of the specified spin isomer in the sample which, in absence of ortho-para conversion, is determined by its preparation history. Note that only the spatial factor $g = 2\Lambda_m + 1$ is retained in equation (4.21). The reduced matrix element of the dipole moment is given by equation (4.13). $d_N = 1.48 * 10^{-27}\mathrm{m}^3$ is the numeric density of absorbing centers in solid C_{60}. In the mid infrared region the refractive index of C_{60} can be assumed to frequency independent and approximatively equals to 2 [58].

In the experiments presented later the measured transmittance $T = I_\delta(\omega)/I_0(\omega)$ is con-

verted to $\alpha(\omega)$ by means of

$$\alpha(\omega) = -\frac{1}{\delta} \ln \left[\frac{T(\omega)}{(1-R)^2} \right], \tag{4.22}$$

where the reflection index $R = [(1-\eta)/(1+\eta)]^2$ accounts for the amount of light lost by reflection. For well-resolved peaks the integrated absorptions are obtained by integrating the absorbance equation (4.22) over non overlapping regions. When the peaks are partly overlapping a deconvolution procedure is used to obtain the individual absorptions. Each experimental integrated absorption is then compared to the integrated area, equation (4.21), considering all the transitions whose frequencies fall within the width of the experimental peak.

4.2 Experimental results

The infrared (IR) spectroscopy of endohedral hydrogen fullerenes has been performed in collaboration with the research group of Toomas Rõõm and coworkers at KFBI in Tallinn, Estonia. All the experimental findings and the analysis of the IR spectroscopy of $H_2@C_{60}$ reported in the following have been published [59, 60].

Transmission spectra were obtained using a Bruker interferometer Vertex 80v equipped with a halogen lamp as source, KBr beam splitter and a HgCdTe or an InSb detector. The apodized resolution was typically 0.3 cm^{-1} or better. Two identical vacuum tight chambers with Mylar windows were employed in the IR measurements. The chambers were put inside an optical cold finger type cryostat with KBr windows. In the low temperature measurements, the chamber containing the sample for analysis was filled with He exchange gas while the empty chamber served as a reference. The temperature of the sample could be set anywhere in the range from 300 K down to 6 K.

Two samples were used for IR study: a normal endohedral hydrogen fullerene was prepared at Kyoto University by the molecular surgery method [22, 23] and a para enriched sample prepared at Columbia University using molecular oxygen as a spin catalyst for ortho-para conversion [61, 62]. Briefly, the $H_2@C_{60}$ adsorbed on the external surface of a NaY zeolite was immersed in liquid oxygen at 77 K for 30 minutes, thereby converting the incarcerated H_2 spin isomers to the equilibrium distribution at 77 K (ortho to para ratio 1:1). The oxygen was pumped away before the endofullerene-NaY complex was brought back rapidly to room temperature. The para enriched $H_2@C_{60}$ was extracted from the zeolite with CS_2 and the solvent was evaporated by continuously flowing argon on it. Both of the samples were in powder form. For IR measurements the powder was pressed into thin pellets under vacuum. The diameter of the sample pellets was 3 mm and their thickness $\Delta x = 0.25$ mm (H2@C60) or $\Delta x = 0.12$ mm (para enriched $H_2@C_{60}$).

The analysis of the temperature dependence of the IR spectra leads to the identifica-

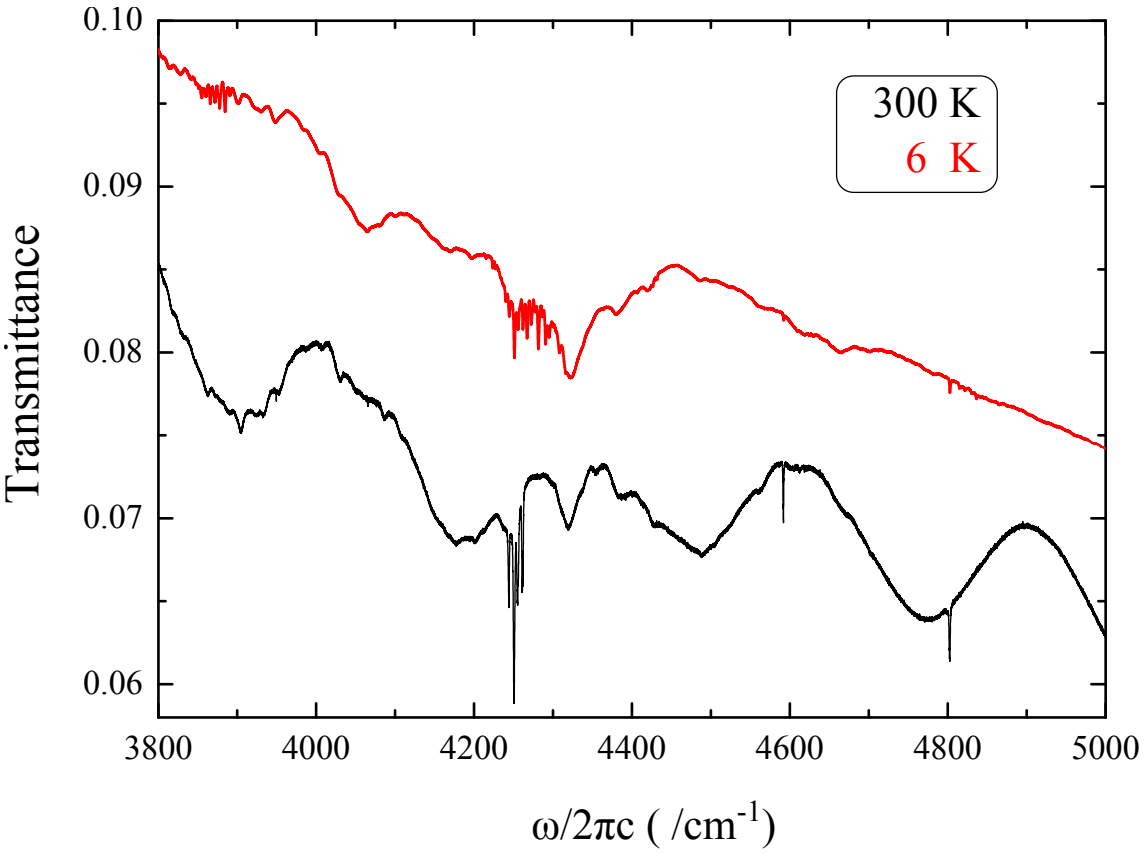

Figure 4.1: Infrared spectra of $H_2@C_{60}$ at 300 K (upper, red) and at 6 K (lower, black) in the 3800-5000 cm^{-1} region. Narrow peaks around 4250, 4600 and 4800 cm^{-1} are related to transitions in the hydrogen-fullerene system, see text and figure 4.2. The low frequency oscillations with a period of 300 cm^{-1} are caused by a difference in the optical length between the sample and the reference chambers.

tion of the peaks in terms of transitions between energy levels of endohedral hydrogen. Temperature and spin isomer enrichment can be used as editing tools for the experimental spectra giving some control on the enhancement/reduction of the intensity of specific sets of peaks. The temperature determines the population of the levels in the ortho and para manifolds while spin enrichment is helpful in solving ambiguities in the assignment since at a fixed temperature the line intensity is proportional to the relative abundance of ortho and para molecules.

Infrared transmittance spectra of $H_2@C_{60}$ at 300 K and 6 K are reported in figure 4.1. Sharp peaks are evident in the regions around 4250, 4600 and 4800 cm^{-1}. They are more pronounced in the 6 K spectrum. Some less intense set of peaks are visible at the base of the 4250 cm^{-1} sharp peak at 300 K. A similar 'brush' of less intense lines are visible around 3800 cm^{-1} in the 300 K spectrum only.

IR spectra were recorded at intermediate temperatures between 300 K and 6 K and inspected for peaks by scrolling through suitable rescaled horizontal windows. All the peaks appeared to be gathered in four narrow spectral regions around the frequencies discussed above. The only exceptions consisted of two weak peaks at approximately

4065 and 4070 cm^{-1} (both observable only at low temperatures). Baseline corrected absorption spectra are reported in figure 4.2 for four representative temperatures. For clarity only the regions containing IR peaks are extracted from the full spectral window. At this scale the richness of details is apparent. Many peaks with widths of 1-2 cm^{-1} or less are visible. The peaks are narrow because of the homogeneity of the confinement in the sample. Fewer peaks are observed at 6 K: when the temperature increases their intensity is reduced and several less intense peaks emerge. The intensity of the IR absorption lines is related to the thermal distribution of particles in the energy levels of the system. The IR spectra at low temperatures are less congested because the observed transitions involve only few macroscopically populated levels as initial states. For the same reason the intensity of the lines is high resulting in enhanced spectroscopic sensitivity. When the temperature increases more levels become populated, each of them with lower fractional population, resulting in more numerous but less intense lines. There is no appreciable shift in the frequency of the lines with temperature. Few peaks in the region around 4420-4440 cm^{-1} appear only at high temperature in correspondence of strong background absorption, are reported successively in figure 4.6

The frequency of the observed lines is too high to be attributed to the vibrational modes (fundamental and combination modes) of solid C_{60} which span the region from 270 to 3500 cm^{-1} [63]: the accurate detection of IR-active C_{60} combination modes at high frequency is feasible on large single C_{60} crystals but is very difficult on powder samples. The observed peaks are at higher frequency compatible with transitions in the first vibrational band of endohedral hydrogen: they can be described as combinations of the forbidden vibrational transition $v = 0 \rightarrow v = 1$ with the IR allowed translational-rotational modes.

4.3 Analysis of the IR spectra

IR spectra of $H_2@C_{60}$ are analyzed using the information obtained from the simpler low temperature case to understand the more complex high temperature spectra. In this section the energy levels are labelled by the sequence of quantum numbers $|vNLJ\Lambda\rangle$ defining the related zero-order spherical state. Transitions will be defined by the initial and final set of quantum numbers of the levels involved. Since the rotational quantum number J is an approximately good quantum number, the standard notation for IR transitions in diatomic molecules is used [3]: for example transitions with $\Delta J = 0$ and 2 are denoted as $Q(J_i)$ and $S(J_i)$ respectively, where J_i is the value for the initial state. Selection rules play a fundamental role in the assignment process: for homonuclear hydrogen in spherical trap these are $\Delta\Lambda = 0, \pm 1$, $\Delta J = 0, \pm 2$, $\Delta N = \pm 1$, see section 4.1.1.

The computational method for the analysis of infrared spectra is the following. First the extent of the translational-rotational spherical basis in each of the two vibrational manifolds of interest has to be chosen. Then the reduced dipole moment equation (4.9)

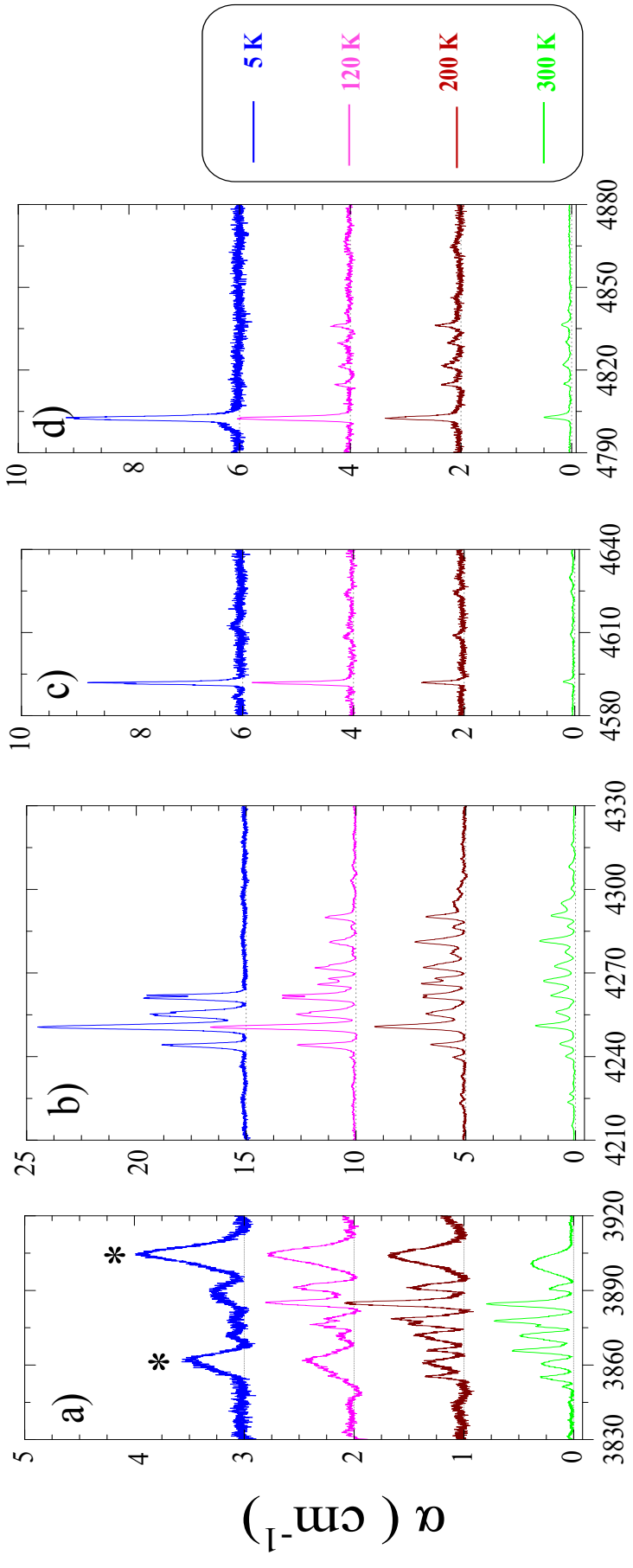

Figure 4.2: IR experimental absorption spectra of (non enriched) $H_2@C_{60}$ at four different temperatures: absorption, α in cm^{-1}, is plotted versus frequency, ω in cm^{-1}. Spectra have corrected baseline and are shifted for clarity. Note that the vertical scale is different from panel to panel. The peaks are concentrated in four main regions, panel a)-d). In each panel from top to bottom, 6 K spectra are in blue, 120 K spectra in magenta, 200 K spectra in brown and 300 K spectra in green. Broad features, labeled by an asterisk in the 6 K spectrum in panel a), does not correspond to endohedral hydrogen transitions but to background absorption.

between all the spherical states in the initial and final vibrational manifolds is evaluated and stored. Specifically the radial integral is given by equation (3.69) or in first approximation by equation (4.11). After diagonalizing the effective translational-rotational Hamiltonian in the vibrational manifolds of interest the energy E and the coefficients ${}^{v}c_{JNL}$ are found, refer to section 3.3.2. The reduced matrix element of the dipole operator, equation (4.13) may be then evaluated for any choice of the coefficients $\overline{A}^{lj;n}_{v_f\text{-}v_i}$. A simulated stick spectrum is obtained by plotting the absorption area between all the initial and final energy levels versus their frequency. In the fitting procedure the simulated spectrum is compared to high-resolution experimental spectra at different temperatures by changing the parameters in the Hamiltonian and the coefficients in the dipole expansion to match the positions and the intensities of the lines.

4.3.1 Low temperature

The experimental low temperature IR absorption spectra of $H_2@C_{60}$ at 6 K are reported in figure 4.3 together with the scheme of the involved energy levels. In panel a) two weak lines are visible just above the noise. In panel b) one can distinguish clearly four separate peaks. The line at 4255 cm^{-1} is broader with a shoulder suggesting the presence of more than one component while the line at 4161 cm^{-1} is split into two peaks. In each of the panel c) and d) only one line is visible with some asymmetry/shoulder in the shape of the 4590 cm^{-1} line and a broad feature at the base of the 4802 cm^{-1} line. In the analysis presented below the interest is focused on the gross structure of the spectra and these finer details are neglected. At low temperature only the ground vibrational-rotational-translational ortho and para states are populated: the initial levels of all the observed transitions are either $|00011\rangle$ for ortho-H_2 or $|00000\rangle$ for para-H_2. The two very weak peaks at 4065.4 and 4071.4 cm^{-1} are assigned be the fundamental vibrational transitions for ortho ($Q(1)$, $|01001\rangle \rightarrow |11001\rangle$) and para ($Q(0)$ $|00000\rangle \rightarrow |10000\rangle$) species, respectively. Both transitions are redshifted by about 90 cm^{-1} with respect to free H_2 at 4155.0 and 4161.2 cm^{-1}. These transitions are forbidden according to the selection rule ΔL = odd. Their activity must follow from solid-state effects since, due to the real icosahedral symmetry of C_{60}, *pure* vibrational transitions of $H_2@C_{60}$ are not allowed. The assignment of the lines to fundamental transitions is based on the following observations. Firstly vibrational transition with comparable redshifts have been observed in interstitial hydrogen in solid C_{60} [50]). Secondly the difference between the two pure vibrational frequencies, ≈ 6 cm^{-1}, is simlar to that of free hydrogen. This is expected since this difference is mainly determined by the first-order vibration-rotation coupling α_e which is not affected much by the confinement. Finally this assignment is consistent with the analysis of high temperature spectra as discussed below.

The four lines in the 4250 cm^{-1} region are intense and must correspond to the lowest allowed IR-active transitions in the observed vibrational band. The transitions from the ground states to the lowest excited translational states account for the four observed

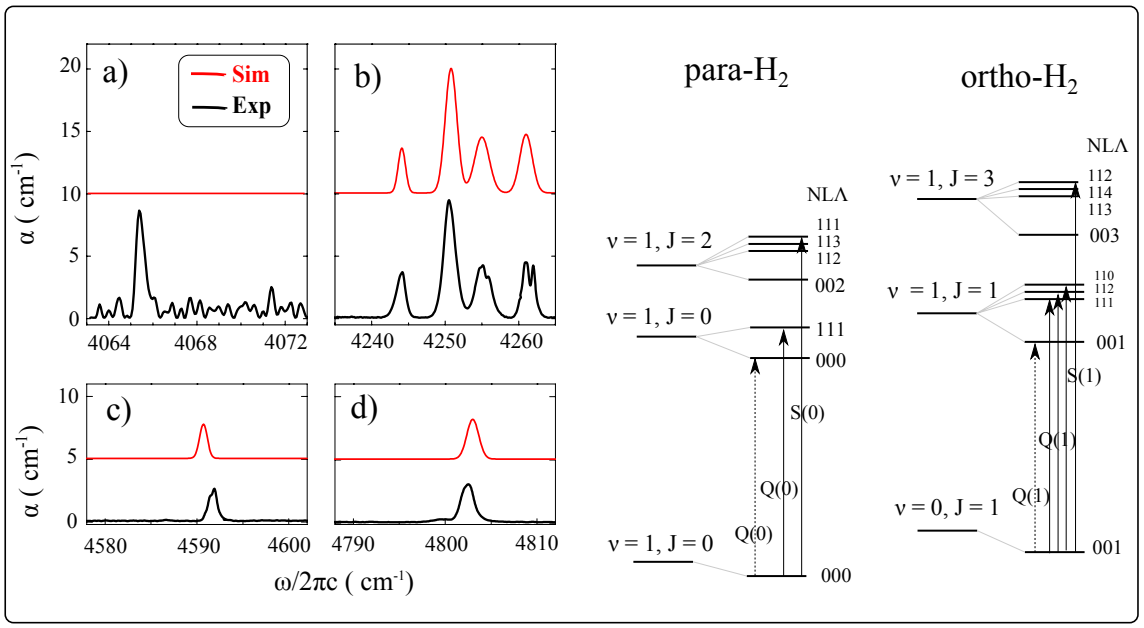

Figure 4.3: Experimental baseline-corrected IR absorption spectra of $H_2@C_{60}$ at 6 K (black) and the best fit simulated theoretical spectrum (red, shifted) in panels a)-d). a) Fundamental vibrational transitions; these are forbidden in theory and the simulated spectrum contains no peaks. Note that the experimental spectrum has been scaled by a factor 40. b) Q transitions with $\Delta J = 0$ and $\Delta N = 1$. c) Para-H_2 and d) ortho-H_2 S transitions with $\Delta J = 2$ and $\Delta N = 2$. For clarity the relevant energy levels are shown beside. The energy levels were refined against low-T IR data as explained in the text. The energy levels of free H_2 are shown on the left while the effect of confinement by C_{60} is shown on the right, separately for para- and ortho-H_2. The arrows show transitions corresponding to the observed low-T IR peaks. All transitions are from the vibrational state $v = 0$ to $v = 1$. The letter indicates the change in J: Q for $\Delta J = 0$ and S for $\Delta J = 2$ and the number in parentheses is the initial J value. The fundamental vibrational transitions, marked by dashed lines, are dipole forbidden.

peaks, see figure 4.3. The excited translational state $v = 1$, $N = 1$, $L = 1$ is split into three levels with Λ =0, 1, 2 in the ortho manifold where $J = 1$ because of the translational-rotational coupling; in the para manifold where $J = 0$ there is only one excited translational state with $\Lambda = 1$. These lines are Q transitions, $\Delta J = 0$, with $\Delta N = 1$, in which the vibrational excitation is accompanied by the excitation of one translational quantum.

The two lines in the 4600 and 4800 cm^{-1} regions fall at frequencies about 6 and 10 times the rotational constant for H_2 above the 4250 cm^{-1} region. These lines correspond to IR transitions in which the vibrational mode is accompanied by the excitation of one translational quantum and two rotational quanta. These are S lines, $\Delta J = 2$, with $\Delta N = 1$. Because of the selection rule on the total angular momentum Λ only one para $S(0)$ transition is expected to be active within the set of levels with $J = 2$ and $N = 1$ and only ortho $S(1)$ transition is expected to be active in the set of levels with $J = 3$ and $N = 1$, see figure 4.3.

A quantitative interpretation of the low temperature IR spectroscopy follows from the study of the effective Hamiltonian equation (3.56) in $v = 1$ to first-order in pertur-

	$NLJ\Lambda$		ΔE	$\frac{\lvert\langle f\rVert\mu\rVert i\rangle\rvert^2}{2\Lambda_i+1}$
	Initial $v=0$	Final $v=1$		
$Q(0)$	$\lvert 00000\rangle$	$\lvert 10001\rangle$	0	0
$Q(1)$	$\lvert 00011\rangle$	$\lvert 10011\rangle$	$-2\alpha_e$	0
$Q(1)$	$\lvert 00011\rangle$	$\lvert 11111\rangle$	$\hbar{}^1\omega_T\left(1+{}^1\Delta_{\text{An}}-5{}^1\Delta_{\text{R-T}}\right)-2\alpha_e$	$\frac{1}{3}\left(\rho^{10}+\frac{\rho^{12}}{\sqrt{2}}\right)^2 n_{\text{o}}$
$Q(1)$	$\lvert 00011\rangle$	$\lvert 11112\rangle$	$\hbar{}^1\omega_T\left(1+{}^1\Delta_{\text{An}}+{}^1\Delta_{\text{R-T}}\right)-2\alpha_e$	$\frac{5}{9}\left(\rho^{10}-\frac{\sqrt{2}\rho^{12}}{10}\right)^2 n_{\text{o}}$
$Q(0)$	$\lvert 00000\rangle$	$\lvert 11101\rangle$	$\hbar{}^1\omega_T\left(1+{}^1\Delta_{\text{An}}\right)$	$\left(\rho^{10}\right)^2 n_{\text{p}}$
$Q(1)$	$\lvert 00011\rangle$	$\lvert 11110\rangle$	$\hbar{}^1\omega_T\left(1+{}^1\Delta_{\text{An}}+10{}^1\Delta_{\text{R-T}}\right)-2\alpha_e$	$\frac{1}{9}\left(\rho^{10}-\sqrt{2}\rho^{12}\right)^2 n_{\text{o}}$
$S(0)$	$\lvert 00000\rangle$	$\lvert 11121\rangle$	$\hbar{}^1\omega_T\left(1+{}^1\Delta_{\text{An}}+5{}^1\Delta_{\text{R-T}}\right)+6\left(B_e-\frac{3}{2}\alpha_e\right)$	$\left(\rho^{12}\right)^2 n_{\text{p}}$
$S(1)$	$\lvert 00011\rangle$	$\lvert 11132\rangle$	$\hbar{}^1\omega_T\left(1+{}^1\Delta_{\text{An}}+4{}^1\Delta_{\text{R-T}}\right)+10\left(B_e-\frac{17}{10}\alpha_e\right)$	$\frac{3}{5}\left(\rho^{12^2}\right)n_{\text{o}}$

${}^1\omega_T=\sqrt{\frac{{}^1V_{00}^{00;2}}{2\pi M}}$; ${}^1\beta_T=\frac{\hbar}{M{}^1\omega_T}$; ${}^1\Delta_{\text{An}}=\frac{5}{2}\frac{{}^1V_{00}^{00;4}}{{}^1\beta_T{}^1V_{00}^{00;2}}$; ${}^1\Delta_{\text{R-T}}=\frac{\sqrt{5}}{20}\frac{{}^1V_{00}^{00;2}}{{}^1V_{00}^{22;2}}$

$\rho^{lj}=\overline{A}_{0\text{-}1}^{lj;1}\langle N=1,L=1;{}^1\beta_T|R|N=0,L=0;{}^0\beta_T\rangle$

Table 4.1: Analytical expressions for the line positions and intensities in first-order pertubation theory for the low temperature IR specta of endohedral molecular hydrogen fullerene. From left to right the columns represent the type of transition, the quantum numbers for the initial and final states involved, the energy shift and the intensity factor. The energy shifts are referred to the fundamental vibrational transition and the corresponding frequency shifts in cm^{-1} are obtained dividing by hc. α_e represents the strength of vibration-rotation coupling, B_e is the rotational constant, ${}^1\omega_T$ is the translational frequency, ${}^1\Delta_{\text{R-T}}$ and ${}^1\Delta_{\text{An}}$ are first-order corrections to the energy, due to the rotation-translation coupling and the anharmonic potential. The relationships with the potential parameter are at the bottom of the table. The integrated absorption is obtained by multiplying the intensity factor in the last column by $d_N\pi/(3\eta\epsilon_0 hc)$. n_{o} and n_{p} represents the ortho and para fractional abundance ($n_{\text{o}}+n_{\text{p}}=1$). ρ^{lj} represents the quantum average of the radial electric dipole coefficents A^{lj} over the vibrational and translational wavefunctions, see bottom of the table for the explicit definiton.

bation theory, table 4.1. The relative position of the fundamental vibrational transitions fixes α_e. The position of the remaining lines depends on the combination of harmonic and anharmonic terms $\hbar{}^1\omega_T(1+{}^1\Delta_{\text{An}})$: the low temperature data does not allow one to establish the contribution of the anharmonic corrections to the translational excitation energy. Interestingly the ortho to para ratio can be estimated from the ratio of the intensity factor of the $S(1)$ and $S(0)$ lines, see the last two rows of table 4.1.

The indications of the perturbative approach have been extended by numerical diagonalization of the full roto-translational Hamiltonian over a spherical basis set with $N\leq 2$, $J\leq 2$[59]. Three potential parameters ${}^1V_{00}^{00;2}$, ${}^1V_{00}^{00;4}$ and ${}^1V_{00}^{22;2}$, the rotational constant B_e, the dipole coefficients ρ^{10} and ρ^{12} and the ortho/para ratio $n_{\text{o}}/n_{\text{p}}$ were fitted to match 12 experimental values, 6 frequencies and 6 intensities. The position of the fundamental vibrational transitions was used as input in the fit procedure. Only one set of values is found to reproduce quite accurately the experimental line positions and intensities. The best values for the potential parameters in the first vibrational state were ${}^1V_{00}^{00;2}=(27\pm 6)\,\text{J}\,\text{m}^{-2}$, ${}^1V_{00}^{22;2}=(1.5\pm 0.2)\,\text{J}\,\text{m}^{-2}$ and ${}^1V_{00}^{00;4}=(-2\pm 20)10^{20}\,\text{J}\,\text{m}^{-4}$. The

Experimental			Calculated			$JNL\Lambda$		
ω (/cm^{-1})	S (cm^{-1})	σ (cm/molecule)	ω (cm^{-1})	S (cm^{-1})	σ (cm/molecule)	Initial $v = 0$	Final $v = 1$	
4065.44	0.09	6.3×10^{-23}	4065.44*	0	0	0000	0001	$Q(0)$
4071.39	0.01	7.4×10^{-24}	4071.39*	0	0	0011	0011	$Q(1)$
4244.5	18.8	3.8×10^{-21}	4244.1	4.9	3.0×10^{-21}	0000	1111	$Q(1)$
4250.7	4.9	1.3×10^{-20}	4250.7	20.0	1.4×10^{-20}	0011	1112	$Q(1)$
4255.0	10.9	7.1×10^{-21}	4255.5	11.2	7.6×10^{-21}	0011	1101	$Q(0)$
4261.0	8.7	5.9×10^{-21}	4261.0	10.0	6.8×10^{-21}	0011	1110	$Q(1)$
4591.5	3.1	2.1×10^{-21}	4590.7	2.9	2.0×10^{-21}	0000	1121	$S(0)$
4802.5	5.6	3.8×10^{-21}	4803.0	5.1	3.4×10^{-21}	0011	1132	$S(1)$

Table 4.2: Experimental and calculated center frequencies ω, integrated absorption area S and cross sections σ for the IR-active transitions in the vibrational band $v = 0 \rightarrow v = 1$ of $H_2@C_{60}$ at 6 K. The experimental data refers to the non-enriched sample. The quantum numbers N, L, J, Λ are needed to identify the initial and final energy levels. The integrated cross section is obtained by dividing the absorption area by the numeric density, $d_N = 1.48 \times 10^{-21}\text{cm}^{-3}$. The first two rows correspond to the experimental fundamental vibrational transitions for ortho and para hydrogen, respectively. The intensity of these transitions is null in the spherical model used for the fit but their frequency was used as reference in the fitting procedure (labeled by a *).

low temperature data are insufficient to derive accurately the anharmonic corrections which are poorly defined by transitions involving only $N = 0$ and $N = 1$. This is reflected in the large uncertainty on ${}^1V_{00}^{00;4}$. The fitted rotational constant is $B_e = 59.3 \pm 0.2$ cm^{-1} while $\alpha_e = 2.98 \pm 0.10$ cm^{-1} is obtained directly by the difference in the fundamental vibrational frequencies. The ratio between the induced dipole coefficients is $\rho^{12}/\rho^{10} = -2 \pm 0.2$. The ortho to para ratio $n_o/n_p = 2.8 \pm 0.2$ is consistent with an equilibrium temperature warmer than 120 K, suggesting negligible spin conversion during the duration of the experiment. Further discussion relative to the best fit parameters is postponed after the analysis of the high temperature data.

Experimental data and best fit results are summarized in table 4.2. The best fit simulated spectrum is in good agreement with experimental one in figure 4.3: in the simulated spectrum the line were artificially broadened maintaining the value of the integrated absorption. The numerical analysis solved the ambiguity in the assignment of the Q lines in the 4250 cm^{-1} region: the line at 4255 cm^{-1} are para transition and the lines at 4244 4250 and 4261 cm^{-1} are ortho transitions with Λ =1, 2 and 0, respectively. The relative disposition of the Q lines depends on the sign of the roto-translation coupling, compare rows 3-6 in table 4.1.

The low temperature assignment was confirmed later when para enriched samples became available [62]. In figure 4.4 the para peaks, as assigned above, are more intense than in the non-enriched sample. At the time of the experiment the ortho/para ratio was estimated to be $n_o/n_p = 1.4$ from the ratio of the area $S(1)/S(0)$ and $Q(1)/Q(0)$ in the enriched and non-enriched sample.

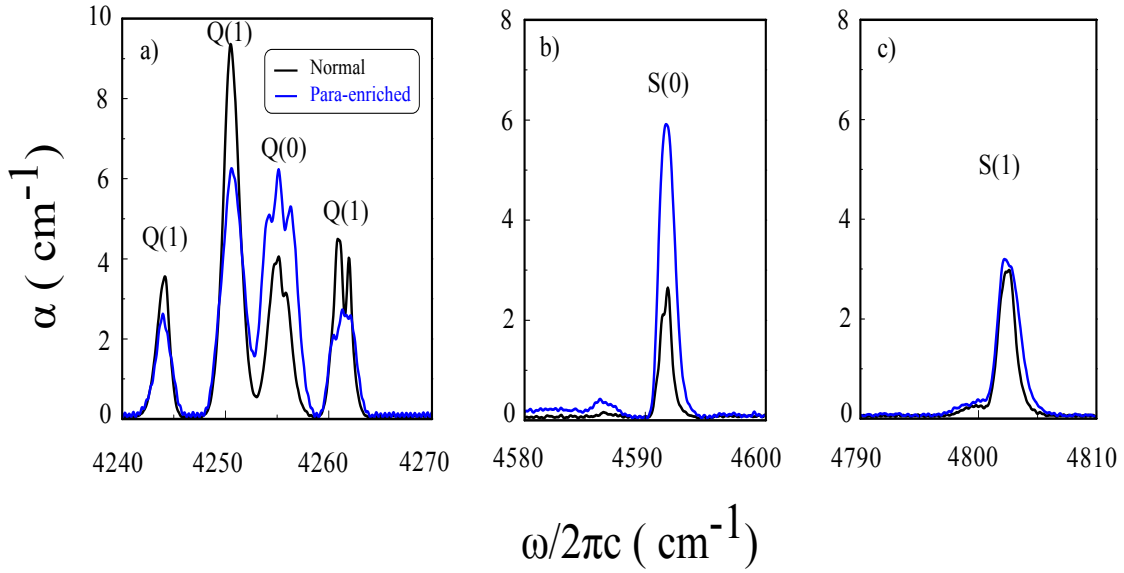

Figure 4.4: Comparison of the low temperature infrared Q and S transitions of $H_2@C_{60}$ for the non-enriched sample recorded at 6 K (black) and the para-enriched sample recorded at 20 K (red). Note that the para lines $Q(0)$ and $S(0)$ are more intense in the enriched sample than in the non-enriched one.

4.3.2 High temperature

The availability of a para-enriched sample is even more appreciated for line assignment at higher temperatures when the number of observed peaks increases as a consequence of excited translational levels becoming populated. For example figure 4.5 shows two spectra of para-enriched $H_2@C_{60}$ at 300 K in the region 4220-4310 cm^{-1}: the first spectrum (black line) was recorded four days after the para enrichment process and the second one (red line) was recorded after leaving the same sample at room temperature for a further 19 days. During this period some of the para molecules converted back to ortho. The intensity of para lines decreased while the intensity of ortho lines increased and most of the lines could be assigned to either ortho or para transitions.

The spectrum at 200 K was chosen for extensive study because it provides the best compromise between spectroscopic detail and sensitivity. At this temperature lines originating from excited translational states with $N = 1$ and $N = 2$ are visible. At higher temperatures no new details appear and the signal to noise ratio for the observed lines is reduced since the intensity spreads over many levels, see figure 4.2. From the analysis of the 200 K spectrum the parameters for the confining potential in the ground vibrational state $v = 0$ can be determined and the values in $v = 1$, obtained from the 6 K data, can be improved as well. The computational methodology for the analysis of the IR spectra has been discussed in 3.3.1 and at the beginning of 4.3. The basis has been extended up to $N = 7$ and $J = 3$ for a total 192 para and 292 ortho states in each of the two vibrational manifolds $v = 0$ and $v = 1$. In the specific case the parameters determining the position and the intensity of the lines are the potential parameters ${}^{v}V_{00}^{00;2}$,

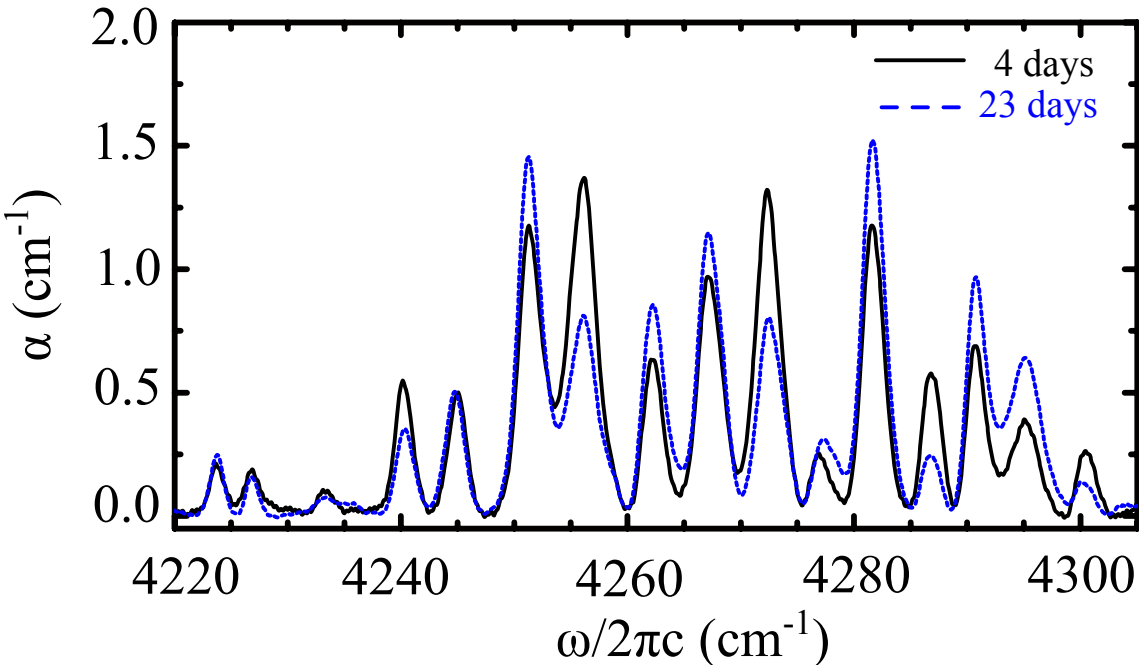

Figure 4.5: IR spectra of para-enriched $H_2@C_{60}$ at 300 K in the region around 4250 cm^{-1}. The black line corresponds to the spectrum collected 4 days after enrichment and the red line to the spectrum collected after a further 19 days. Para to ortho spin conversion is evident. Some lines did not change their intensity appreciably: they correspond to overlapping transitions. Using the information about line intensity from the non-enriched sample the ortho to para ratio was estimated to be $n_o/n_p \approx 1.36$ (black line) and $n_o/n_p \approx 2.89$ (red line).

${}^{v}V_{00}^{00;4}$, ${}^{v}V_{00}^{22;2}$, ${}^{v}V_{00}^{22;2}$ with $v = 0$ and $v = 1$; the vibrational and rotational parameters $\omega_0 = \omega_e(1 - 2x_e)$, B_e, α_e, D_e and the dipole coefficients $\overline{A}_{1\text{-}0}^{10;1}$, $\overline{A}_{1\text{-}0}^{12;1}$ and the ratio n_o/n_p. The values of the parameters and the assignment at low temperature are used as starting input for the fitting procedure of the high temperature data.

The best fit spectrum along with the experimental spectrum at 200 K is displayed in figure 4.6. The agreement is good for most of the lines. For clarity the variations in the rotational and translational quantum numbers are reported for each spectral region. Panels figure 4.6b), d) and e) shows transitions with $\Delta N = 1$. These panels correspond to the same kind of transitions observed at 6 K. The lines spread over larger intervals because the spacing between successive N is not uniform due to anharmonicity in the confining potential. In addition allowed transitions with $\Delta N = -1$ become observable: these are shown in figure 4.6a) and in figure 4.6c). The former region contains Q lines ($\Delta J = 0$). The latter region contains ortho $S(1)$ lines ($\Delta J = 2$) but in the experimental spectrum only the line at 4431.9 cm^{-1} is recognizable since strong background absorption covers the remaining ones. The splittings observed in the experimental spectrum at 4255, 4261, 4267 cm^{-1} cannot be understood within the spherical approximation for the fullerene cage. They may be related to crystal field effects or inhomogeneity in the sample. In any case it is not clear why and how a mechanism may affect so visibly only these lines but not any others. The experimental line positions and intensities together

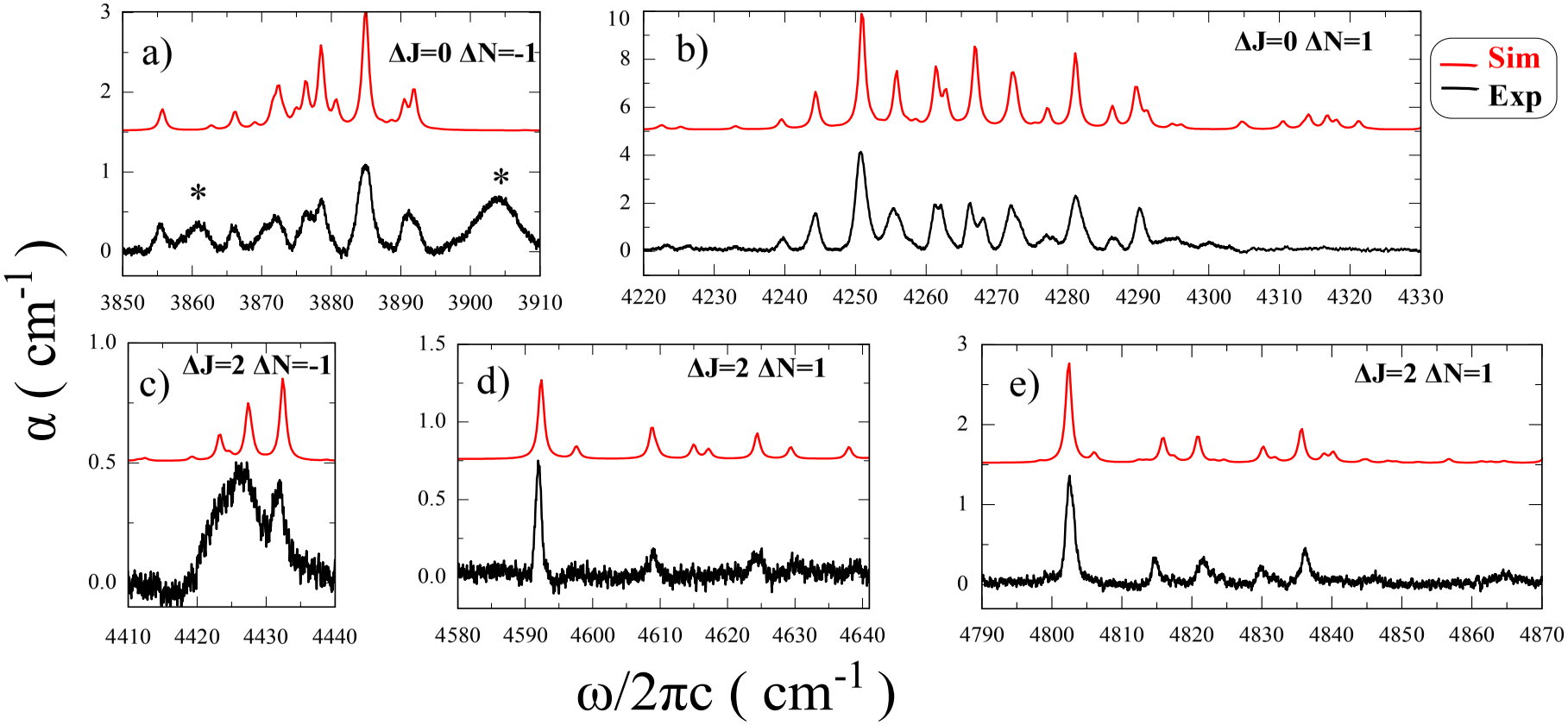

Figure 4.6: IR absorption spectra of (non-enriched) $H_2@C_{60}$ at 200 K: experimental spectra are in black and best fit simulated spectra are in red. For clarity the variation of the rotational and translational quantum numbers is reported in each panel.

with their theoretical values are reported in table 4.3. Here the transitions are identified giving the relevant quantum numbers for the initial and the final states involved. Table 4.4 report the energy levels identified by the quantum numbers of the spherical state which has the highest probability $|^{v}c_{JNL}|^2$.

The validity of the model used so far is confirmed by the analysis of the temperature dependence of the integrated absorptions: for a given transition S is proportional to the population of the initial level according to equation (4.21), assuming that the ortho/para ratio remains constant, i.e. that there is negligible spin conversion during the experimental session. Figure 4.7 shows a comparison between the normalized experimental absorption area of some selected transitions and the predicted normalized populations (normalization to one at their respective maxima). The agreement between the experimental normalized integrated absorptions and the theoretical normalized population is good below 220 K. Above such temperature there is not a perfect agreement although experiments and theory shows a similar decrease in intensity with temperature. The reason for such deviations are not clear in the theoretical framework developed so far. Note that the temperature dependence of the populations can be evaluated only after the energy of all the levels is determined and that the comparison can be done only after assigning the experimental lines.

4.3.3 Comments

The values for the best fit parameters are reported in the table 4.5. The potential parameters depend on the vibrational state. The harmonic terms correspond to translational oscillations with frequency equal to ${}^{0}\omega_T$ =138.4 and ${}^{1}\omega_T$ =146.1 cm^{-1}, see equation (3.60). Anharmonic corrections contribute to 22% of the separation between translational states with $N = 0$ and $N = 1$, which are respectively 179.5 and 184.4 cm^{-1}, see table 4.4. In particular the calculated values of the separation between the para translational states $N = 0$ and $N = 1$ in the ground vibrational state is in agreement with the findings (179.9 cm^{-1}) of neutron scattering experiments [64]. The potential parameters ${}^{v}V_{lj}^{00;n}$ show a characteristic dependence on the vibrational quantum number v. The coefficients of the quadratic terms with $n = 2$ increase and the coefficient of the quartic terms ($n = 4$) decrease on passing from $v = 0$ to $v = 1$. Also for n =2, 4 the absolute value of the variations of the best fit coefficients with $j = l = 0$ are larger than the corresponding coefficient with $j = l = 2$. The fact that all the coefficients are positive is consistent with a positive value of the coefficients F_0, H_0, J_0 in the spherical potential $V_{\mathrm{S}}^{\mathrm{C_{60}-H}}(\boldsymbol{x})$, as reported in equation (3.24). The increase in the quadratic coefficients could be anticipated from equation (3.23). Indeed the vibrational averaged values for r^2 and r^4 increase with the vibrational quantum number. Also the absolute value of the variation of ${}^{v}V_{00}^{00;2}$ could be anticipated to be between 8 and 10 times larger than ${}^{v}V_{00}^{22;2}$.

Experimental		Calculated		$JNL\Lambda$		
ω (/cm^{-1})	S (cm^{-1})	ω (cm^{-1})	S (cm^{-1})	Initial v = 0	Final v = 1	
3855.6	0.77	3855.6	0.41	1201	1112	ortho-Q(1)
3866.0	0.47	3866.0	0.09	0200	0111	para-Q(0)
		3866.1	0.27	1201	1110	ortho-Q(1)
3872.2	1.18	3873.2	0.16	2113	2002	para-Q(2)
		3871.6	0.38	1221	1111	ortho-Q(1)
3876.0	1.13	3874.9	0.27	1333	1222	ortho-Q(1)
		3876.3	0.85	1110	1001	ortho-Q(1)
3878.6	1.22	3878.4	0.35	0333	0222	para-Q(0)
		3884.9	1.88	1112	1001	ortho-Q(1)
3884.9	2.80	3884.7	0.64	0222	0111	para-Q(0)
		3884.9	1.88	1112	1001	ortho-Q(1)
3891.3	1.49	3890.5	0.50	1111	1001	ortho-Q(1)
		3891.8	0.77	0111	0000	para-Q(0)
4223.3	0.28	4222.2	0.07	0111	2002	para-S(0)
		4222.7	0.24	3003	3114	ortho-Q(3)
4226.2	0.21	4233.1	0.22	3003	2112	ortho-Q(3)
4233.1	0.22	4233.1.	0.22	2002	2113	ortho-Q(3)
4239.8	0.64	4239.6	0.64	2002	2113	para-Q(2)
4244.4	2.54	4244.5	0.47	2002	2111	para-Q(2)
		4244.4	1.95	1001	1111	ortho-Q(1)
4250.7	7.83	4252.5	0.20	2112	2223	para-Q(0)
		4250.9	7.71	1001	1112	ortho-Q(1)
4255.6	4.29	4255.8	3.65	0000	0111	para-Q(0)
		4257.3	0.22	1112	1222	ortho-Q(1)
4261.3	4.11	4261.4	3.74	1001	1110	ortho-Q(1)
		4261.8	0.08	2111	2220	ortho-Q(2)
4263.0		4262.8	2.10	1111	1222	ortho-Q(1)
4272.1	3.70	4272.1	2.78	0111	0222	para-Q(0)
		4272.7	1.77	1111	1221	ortho-Q(1)
4281.2	4.33	4281.2	4.90	1223	1334	ortho-Q(1)
4286.5	0.89	4286.4	1.41	0222	0333	para-Q(0)
		4289.9	0.49	0111	0200	para-Q(0)
4290.2	2.72	4289.7	2.13	1112	1201	ortho-Q(1)
		4291.3	0.90	1201	1312	ortho-Q(1)
4294.8	1.08	4294.8	0.28	0200	0311	para-Q(0)
		4296.2	0.26	1221	1311	ortho-Q(1)
4300.0	0.30	4298.3	0.001	1334	1444	ortho-Q(1)
4306.7	0.92	4305.2	0.19	1222	1311	ortho-Q(1)
4316.4	1.37	4316.8	0.84	1334	1445	ortho-Q(1)
		4318.4	0.51	1332	1443	ortho-Q(1)
4407.4	0.05	4407.2	0.07	1201	3112	ortho-S(1)
4426.8	0.35	4427.4	0.34	1223	3114	ortho-S(1)
		4428.0	0.06	1222	3113	ortho-S(1)
4431.9	0.44	4432.5	0.53	1112	3003	ortho-S(1)
4592.0	0.90	4592.4	0.79	0000	2111	para-S(0)
4608.9	0.37	4608.9	0.31	0111	2221	para-S(0)
4624.3	0.27	4624.5	0.25	0111	2202	para-S(0)
4630.0	0.10	4629.4	0.12	0222	2331	para-S(0)
4802.6	1.80	4802.5	1.94	1001	3112	ortho-S(1)
4814.8	0.39	4815.5	0.16	1112	3222	ortho-S(1)
		4816.2	0.32	1110	3221	ortho-S(1)
4821.6	0.49	4821.0	0.52	1111	3222	ortho-S(1)
4829.7	0.26	4830.3	0.30	1111	3221	ortho-S(1)
4836.2	0.55	4835.8	0.66	1112	3203	ortho-S(1)
4846.4	0.23	4845.2	0.05	1222	3331	ortho-S(1)
		4848.1	0.03	1223	3133	ortho-S(1)
4864.5	0.17	4862.9	0.02	1212	3312	ortho-S(1)
		4864.8	0.03	1333	3444	ortho-S(1)

Table 4.3: Experimental and calculated center frequencies ω and integrated absorption areae S and cross sections σ for the IR-active transitions in the vibrational band $v = 0 \rightarrow v = 1$ in $H_2@C_{60}$ at 200 K. The experimental data refers to the non enriched sample. The quantum numbers N, L, J, Λ are needed to identify the initial and final energy levels. The last column identifies the type of transition.

para-H_2@C_{60}

$v = 0$						$v = 1$					
ΔE	$JNL\Lambda$	$\lvert c\rvert^2$	ΔE	$JNL\Lambda$	$\lvert c\rvert^2$	ΔE	$JNL\Lambda$	$\lvert c\rvert^2$	ΔE	$JNL\Lambda$	$\lvert c\rvert^2$
0.0	0000	0.97	730.0	2220	0.87	0.0	0000	0.98	723.2	2220	0.89
179.5	0111	0.93	741.5	2202	0.72	184.4	0111	0.94	732.6	2202	0.74
347.9	2002	0.95	815.3	0444	0.84	330.3	2002	0.97	823.2	0444	0.85
371.1	0222	0.85	878.1	0422	0.67	380.3	0222	0.89	877.4	0422	0.70
389.7	0200	0.81	906.4	0400	0.61	398.1	0200	0.84	901.8	0400	0.65
523.5	2112	0.94	914.1	2333	0.78	509.7	2112	0.95	909.4	2334	0.85
528.5	2113	0.91	914.4	2334	0.82	516.2	2113	0.93	909.4	2333	0.80
532.7	2111	0.92	921.6	2332	0.71	521.1	2111	0.94	917.1	2332	0.72
573.2	0333	0.92	924.7	2335	0.81	586.2	0333	0.83	920.4	2335	0.83
601.9	0311	0.68	933.3	2331	0.80	613.2	0311	0.72	929.1	2331	0.82
713.6	2223	0.88	943.9	2312	0.60	704.6	2223	0.90	937.8	2312	0.62
714.7	2222	0.80	956.7	2313	0.63	705.8	2222	0.80	950.3	2313	0.67
721.2	2224	0.87	963.1	2311	0.66	713.3	2224	0.89	956.5	2311	0.70
724.8	2221	0.87				717.0	2221	0.89			

ortho-H_2@C_{60}

$v = 0$						$v = 1$					
ΔE	$JNL\Lambda$	$\lvert c\rvert^2$	ΔE	$JNL\Lambda$	$\lvert c\rvert^2$	ΔE	$JNL\Lambda$	$\lvert c\rvert^2$	ΔE	$JNL\Lambda$	$\lvert c\rvert^2$
0.0	1001	0.97	943.0	3224	0.88	0.0	1001	0.98	922.2	3224	0.90
174.9	1111	0.94	950.5	3222	0.87	179.0	1111	0.95	930.0	3222	0.89
180.4	1112	0.93	952.5	3225	0.86	185.6	1112	0.94	933.0	3225	0.88
189.1	1110	0.92	958.9	3221	0.78	196.0	1110	0.94	940.0	3221	0.75
363.7	1222	0.89	971.5	3203	0.71	372.4	1222	0.90	950.8	3203	0.72
372.4	1223	0.88	1038.2	1555	0.83	382.0	1223	0.89	1046.0	1555	0.84
372.8	1221	0.68	1064.6	1556	0.80	382.2	1221	0.65	1068.1	1556	0.80
395.3	1201	0.62	1066.3	1554	0.75	404.7	1201	0.61	1071.6	1554	0.77
562.8	1333	0.83	1127.9	1533	0.57	547.5	3003	0.98	1123.0	1533	0.48
575.0	1332	0.68	1141.0	3334	0.79	575.6	1333	0.85	1124.6	3334	0.81
575.1	1334	0.81	1144.9	3335	0.82	588.3	1334	0.84	1128.3	3335	0.84
577.2	3003	0.97	1146.1	3333	0.67	588.6	1332	0.69	1130.4	3333	0.52
591.9	1331	0.70	1152.2	3332	0.29	603.6	1311	0.74	1137.4	3332	0.81
609.8	1312	0.56	1154.8	1532	0.51	621.2	1312	0.59	1142.8	3336	0.79
623.6	1310	0.65	1158.4	3336	0.78	634.6	1310	0.70	1143.5	3331	0.81
752.0	3113	0.94	1158.7	3331	0.76	726.4	3113	0.95	1146.3	1532	0.43
758.7	3114	0.93	1163.4	3330	0.81	734.5	3114	0.94	1147.7	3330	0.83
761.0	3112	0.93	1166.3	1534	0.35	737.1	3112	0.94	1151.7	1534	0.34
799.0	1444	0.85	1173.2	3313	0.59	808.1	1444	0.86	1155.2	3313	0.62
819.6	1445	0.84	1185.1	1511	0.47	826.6	1445	0.85	1170.3	3312	0.67
819.7	1443	0.76	1188.6	3312	0.63	827.8	1443	0.77	1173.4	1511	0.53
860.2	1422	0.69	1195.9	3314	0.40	862.1	1422	0.72	1177.8	3314	0.39
875.9	1421	0.39	1248.7	1512	0.33	876.0	1421	0.41	1221.6	1512	0.38
892.8	1423	0.58	1277.5	1510	0.47	888.8	1423	0.61	1244.5	1510	0.51
933.1	1401	0.31	1379.7	3445	0.83	921.2	3223	0.79	1359.1	3445	0.84
942.1	3223	0.79	1383.0	3444	0.80	922.2	1401	0.31	1362.3	3444	0.81

Table 4.4: Calculated energies in cm^{-1} for para-H_2@C_{60} up to $JNL\Lambda = 2311$ and ortho-H_2@C_{60} up to $JNL\Lambda = 3444$ in the vibrational states $v = 0$ and $v = 1$. The energies are referenced with respect to the ground rotational-translational *para* state $JNL\Lambda = 0000$. Explicitly ${}^0E_{0000} = 2390.6$ cm^{-1} for $v = 0$ and ${}^1E_{0000} = 6456.0$ cm^{-1} for $v = 1$. The levels are identified by giving the set of quantum numbers $JNL\Lambda$ of the spherical state with the largest probability ${}^v c_{JNL}$.

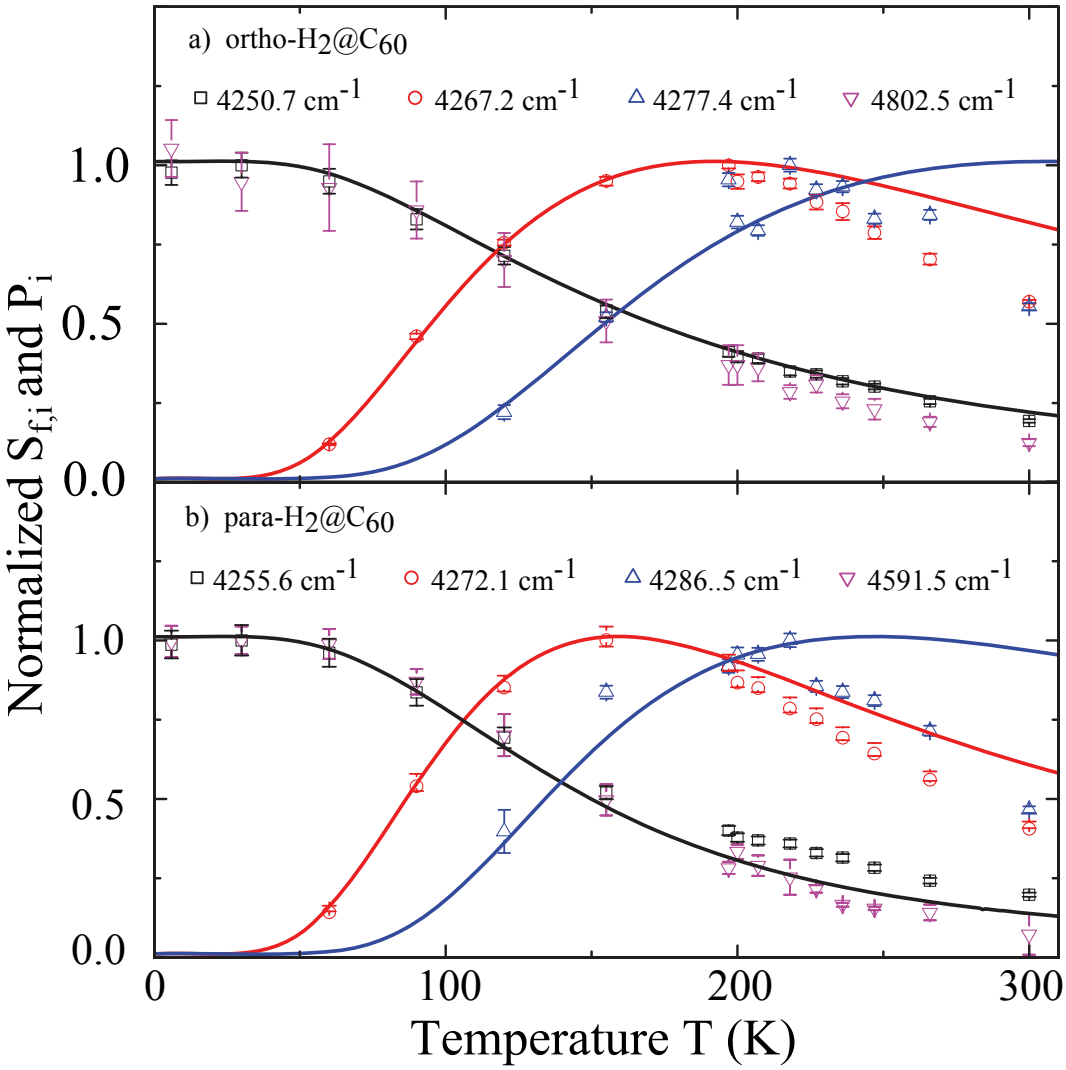

Figure 4.7: Temperature dependence of selected IR absorption line area of ortho-H_2 in (a) and para-H_2 in (b) of transitions starting from states with $N = 0$ (squares □ and down triangles ▽), $N = 1$ (circles ○) and $N = 2$ (up triangles, △). Solid lines are calculated thermal populations of the corresponding initial states, equation (4.19) as obtained from the theoretical model with the best-fit parameters at 200 K. $S_{f,i}$ and $P_i(T)$ have been normalized to one at their maxima.

The decrease of the coefficient for the quartic corrections with $n = 4$ is surprising. This can be related to a slight over-estimate of the corresponding coefficients with $n = 2$.

The best fit value for the vibrational transition $\omega_0/2\pi c = 4062.4$ cm^{-1} is not equal to the observed fundamental para frequency, ${}^{0\text{-}1}\omega_V/2\pi c$ =4071.4 cm^{-1} because of the small difference in the zero-point translational energy in different vibrational levels. The harmonic zero-point translational energy $\frac{3}{2}\hbar({}^1\omega_T - {}^0\omega_T)$ contributes about 8 cm^{-1} to the difference between the two fundamental vibrational frequencies. The remaining 2 cm^{-1} comes from the anharmonic terms. The fundamental vibrational transition ω_0 in H_2@C_{60} is redshifted approximately 100 cm^{-1} from that in free H_2, 4159.4 cm^{-1}, compare equation (3.46) and table 3.1. This redshift has two contributions: the zero-point vibrational energy related to ω_e and anharmonic corrections to the vibrational energy

	$v = 0$	$v = 1$	Unit
${}^{v}V_{00}^{00;2}$	14.27 ± 0.03	15.95 ± 0.03	$\mathrm{J\,m^{-2}}$
${}^{v}V_{00}^{22;2}$	0.562 ± 0.006	1.20 ± 0.01	$\mathrm{J\,m^{-2}}$
${}^{v}V_{00}^{00;4}$	$(2.21 \pm 0.01)10^{21}$	$(2.192 \pm 0.009)10^{21}$	$\mathrm{J\,m^{-4}}$
${}^{v}V_{00}^{22;4}$	$(2.21 \pm 0.02)10^{20}$	$(1.03 \pm 0.009)10^{21}$	$\mathrm{J\,m^{-4}}$
$\omega_0/2\pi c$	4062.3 ± 0.3		$\mathrm{cm^{-1}}$
$B_e/2\pi c$	59.86 ± 0.07		$\mathrm{cm^{-1}}$
$\alpha_e/2\pi c$	2.974 ± 0.025		$\mathrm{cm^{-1}}$
$D_e/2\pi c$	$(4.83 \pm 0.05)10^{-2}$		$\mathrm{cm^{-1}}$
$\overline{A}_{1\text{-}0}^{10;1}$	$(9.1 \pm 0.3)10^{-22}$		C
$\overline{A}_{1\text{-}0}^{10;1}$	$(-4.3 \pm 0.4)10^{-22}$		C
n_o/n_p	2.89 ± 0.05		

Table 4.5: Best fit parameters from the analysis of the infrared spectra of $H_2@C_{60}$ at 200 K.

related to x_e, see section 3.3. Since the observed lines involve only two vibrational states $v = 0$ and $v = 1$ it is not possible to evaluate separately their contributions to the observed redshift. The rotational constant B_e for $H_2@C_{60}$ is slightly reduced relative to free H_2 for which $B_e = 60.8\mathrm{cm}^{-1}$, signalling an increase of 0.8% in the internuclear distance, table 3.1. This increase is consistent with the observed redshift of the fundamental vibrational frequency: according to equation (3.31a) the theoretical shift is expected $-120\mathrm{cm}^{-1}$, when the values of f_e and g_e from equations (3.27a) and (3.27b) are used. The longer internuclear distance and the redshift of the vibrational frequencies are consistent with an attractive interaction between the hydrogen atoms and the cage.

The ratio of the dipole coefficients $\overline{A}_{1\text{-}0}^{12}1/\overline{A}_{1\text{-}2}^{12}1 = -2.1 \pm 0.3$ is consistent with the low temperature one. Only the relative sign of the coefficients can be determined from the experimental data since the intensity of the lines does not depend on sign exchange. The absolute signs and values of the dipole coefficients in C_{60} can be determined from the pair-wise H_2-C induced dipole, equation (4.2). A first principles study of B_{jl} for the $H_2 - C$ pair is out of the scope of this work. Anyway the obtained values are consistent with the theoretical analysis of the pair-wise induced dipole moment in $H_2 - He$ where B_{10} and B_{12} have opposite sign and the latter has the smaller absolute value [53].

The magnitude of the induced dipole moment can be estimated for the absorption area $S = 10.6$ of the ortho line at 4255 cm^{-1} at 6 K: $\mu = 9.8 \times 10^{-3}$ D. This corresponds to an effective charge of 6×10^{-3} C considering that the vibrational average of $\langle R \rangle_{10}$ is 0.36 Å. For comparison the dipole moment of free HD in a $J \rightarrow J + 1$ transition is $5\,10^{-5}$ D. The IR activity originates from the displacement of such a small charge when translational excited H_2 bounces off the center of cage.

4.4 Conclusions and final remarks

In this chapter the infrared spectroscopy of $H_2@C_{60}$ has been presented and analyzed. The experimental spectra are very informative since the lines are narrow and well-resolved compared to hydrogen confined in other environments. The interpretation of this high-quality spectroscopic data allows one to obtain information about carbon-hydrogen interactions in nanocarbons. The high symmetry of the confinement has been exploited to obtain selection rules and transition probabilities. Infrared spectra have been simulated in terms of a few parameters describing the confining potential, the induced dipole moment and the ortho to para ratio. The agreement between the experiments and the simulations, at optimized value of the parameters, is very good both at low and high temperature, figure 4.3 and 4.6. The roto-translational potentials in the ground and first vibrational state and the dipole moment for the dipole transitions in the first vibrational band have been obtained. The redshift in the vibrational frequency and the longer internuclear separation (compared to the free molecule) are consistent with an attractive interaction between C_{60} and each of the atoms in H_2.

The data reported here and their interpretation constitute a benchmark for any first-principles calculations addressing the full six-dimensional quantum dynamics and for induced dipole moment study in $H_2@C_{60}$. In any case the obtained results stand independently of the detailed interactions between the endohedral hydrogen and the cage. In perspective it would be convenient to analyze the high temperature data directly in terms of fundamental parameters defining the carbon-hydrogen interaction. One of such potentials optimized on $H_2@C_{60}$ IR data at 6 K[2] was used to study hydrogen trapped in more complex structures[65].

A final remark is due in regard of the evidence of solid state effects in $H_2@C_{60}$. Ortho and para fundamental transitions have integrated absorptions of the same order of magnitude. The mechanism responsible for the infrared activity of such modes must be identical for the two lines. Although a quadrupole moment may be responsible for the ortho fundamental transition, it is worth noting that the fundamental para transition is absolutely forbidden in spherical approximation since any two levels with $\Lambda_f = \Lambda_i = 0$ cannot be connected by any electric multipole operator. Group theoretical arguments prove that in isolated C_{60} with real icosahedral symmetry the fundamental para line can not be active. In each para-H_2 vibrational manifold the rotational-translational ground state correlates with the total symmetric representation of the icosahedral group A_g: a necessary condition for a mode to be active is that the product of the irreducible representation of the initial state, final state and electric multipole operator contains the total symmetric representation A_g. Electric dipolar and electric quadrupolar operators belong to the representation T_{1u} and H_g of the symmetry group I_h of C_{60} and the product with an A_g state is T_{1u} or H_g, respectively. The most plausible mechanism refers to a local field with reduced symmetry at the center of C_{60}. The local field can originate from molecular packing in the solid, from impurities or from the distribution of ortho/para molecules in nearby cages. In particular a small field allowing non-zero matrix ele-

ments between spherical states with $\Delta\Lambda = 1, \Delta N = 1$ can mix the ground translational states, $N = 0$, with the first excited translational states $N = 1$: the mixing coefficient is proportional to the magnitude of the field divided by the translational frequency. IR activity of the fundamental vibrational line is consistent with a local field of few tenth of cm^{-1}, by comparing the absorption area of the fundamental para vibrational line at 4071.4 cm^{-1} and the para line at 4250 cm^{-1}. Such a local field may be relevant for the lineshape of the proton nuclear magnetic resonance at cryogenic temperature.

Chapter 5

Nuclear magnetic resonance

Nuclear magnetic resonance (NMR) is a widespread spectroscopic tool in scientific research where it is mainly used for the characterization of molecular systems in the solid, liquid and gas phases. The power of the technique lies in the extreme sensitivity of the nuclear spins to the local environment and in the possibilty to modify the coherent spin dynamics almost at will by applying specifically designed sequences of radiofrequency pulses. Structural and dynamical information is encoded in the nuclear spin spectra and spin relaxation times. Here a study of the NMR of $H_2@C_{60}$ in the solid phase is reported. The aim is to use molecular hydrogen as probe to determine if the icosahedral symmetry of C_{60} is reduced in powder samples of endohedral fullerenes. The chapter is organized as follows. First a quick introduction to the NMR dynamics (at level of Bloch equations) and to the used pulse sequences is given. Then the proton NMR lineshape and spin-lattice relaxation of two $H_2@C_{60}$ samples is compared between room temperature and 1.8 K. The two samples have similar NMR spectra and relaxation times with some remarkable but not yet understood differences. Finally lineshapes and spin-lattice relaxations times have been studied between 2 and 0.1 K. The low-temperature data presented here show that the local symmetry is lower than cubic, at least in part of the sample and point out the importance of the history of the sample (preparation, storage, etc.) in the NMR of solid $H_2@C_{60}$.

5.1 Basics of NMR

In a sample placed in a static magnetic field the nuclear spins tend to get oriented parallel to the field giving rise to a tiny magnetization $\mathbf{M}_E$. Assuming that the static field is directed along the Z axis of the laboratory frame, $\mathbf{B}_0 = \mathrm{B}_0 \boldsymbol{n}_Z$, the interaction of the nuclear spin $\hbar\hat{\boldsymbol{I}}$ with the field is described by the Zeeman Hamiltonian:

$$\mathcal{H}_Z = -\gamma \mathbf{B}_0 \cdot \hat{\boldsymbol{I}} = \hbar\omega_0 \hat{I}_Z \tag{5.1}$$

where γ is the gyromagnetic ratio, which is specific to the nuclear species considered, and $\omega_0 = -\gamma \mathrm{B}_0$ is the Larmor frequency. For example $\gamma_\mathrm{H} = 267.513\,\mathrm{MHz\,T^{-1}}$ for hydrogen and $\gamma_\mathrm{D} = 41.065\,\mathrm{MHz\,T^{-1}}$ for deuterium. Larmor frequencies falls in the radio frequency (rf) region of the electromagnetic spectrum in typical laboratory fields of a few T. The energy levels of the Zeeman Hamiltonian are the eigenstates $|I, M_I\rangle$ of the spin angular momentum operator $\hat{I}_Z$ with energy $\hbar\omega_0 M_I$. The separation between consecutive energy levels $\hbar\omega_0$ is uniform and proportional to the applied magnetic field.

At thermal equilibrium at a temperature T, the nuclear magnetization $\mathbf{M}_E = \mathrm{M}_0 \boldsymbol{n}_Z$ points along the field direction and is proportional to the number of spins N in the sample

$$\mathrm{M}_0 = N\gamma\langle\hat{I}_Z\rangle = N\gamma\frac{I(I+1)}{3}\frac{\hbar\omega_0}{k_B T} \tag{5.2}$$

having assumed for simplicity the high temperature limit $\hbar\omega_0 << k_B T$. In typical laboratory conditions where the maximum field attainable is order of 20 T, the high temperature condition is satisfied for any temperature greater than a few millidegrees K.

The equilibrium magnetization can be flipped by a resonant pulse applied at the nuclear Larmor frequency $\omega_{RF} = \omega_0$. For example, a radio frequency field pointing along an axis making an angle ϕ with the X axis in the XY plane

$$\mathbf{B}_1(t) = 2\mathrm{B}_1\left[\boldsymbol{n}_X\cos\phi + \boldsymbol{n}_Y\sin\phi\right]\cos(\omega_0 t) \tag{5.3}$$

can flip $\mathbf{M}_E$ to

$$\mathbf{M}(\tau) = \mathrm{M}_0\left[\boldsymbol{n}_Z\cos(\omega_1\tau) + \boldsymbol{n}_X\sin(\omega_1\tau)\sin(\phi) - \boldsymbol{n}_Y\sin(\omega_1\tau)\cos(\phi)\right] \tag{5.4}$$

at the end of the time interval of duration τ during which the field is on. Here $\omega_1 = \gamma\mathrm{B}_1$. The flipping angle is given by $\theta = \omega_1\tau$ and the pulse is usually denoted as θ_ϕ. For $\theta = \pi/2$ the magnetization is flipped by $\pi/2$ on the XY plane. After the pulse the transverse XY-magnetization precesses at the nuclear Larmor frequency:

$$\mathrm{M}_{XY}(t) = \mathrm{M}_0\sin(\omega_1\tau)\left[\boldsymbol{n}_X\sin(\omega_1 t)\sin(\phi) - \boldsymbol{n}_Y\cos(\omega_1 t)\cos(\phi)\right]. \tag{5.5}$$

The transverse magnetization produces an oscillating magnetic field which in turn induces an oscillating electric potential in a receiving inductance. The induced potential is proportional to the transverse magnetization and retains the same time dependence so that the NMR signal oscillates at the Larmor frequency.

Relaxation aspects are missing in this simplified vectorial model discussed so far. Without relaxation the Fourier transform of the NMR signal would be an infinitely narrow line and the Z-magnetization would never recover to the thermal equilibrium value: the NMR experiment could not be repeated twice. The Bloch equations keep into account relaxation phenomenologically by the introduction of two time constants

T_1 and T_2:

$$M_Z(t) = e^{-t/T_1}\,[M_Z(0) - M_0] + M_Z(0), \tag{5.6a}$$

$$M_{XY}(t) = M_{XY}(0)e^{-t/T_2}\,[\boldsymbol{n}_X \cos(\omega_0 t\phi) + \boldsymbol{n}_Y \sin(\omega_0 t - \phi)]\,. \tag{5.6b}$$

The spin lattice relaxation time T_1 is related to the interactions with the other degrees of freedom which bring the magnetization back to the equilibrium value along the Z axis. The spin-spin relaxation time T_2 is related to the interaction between neighboring spins which is ultimately responsible for the loss of coherence and the consequent line broadening of the NMR signal.

The basic spin dynamics of a system can be understood by using the Bloch equations for the free evolution period and the flip pulse equation for the evolution under strong short pulses. Although the Bloch equations are correct only for a system of non interacting spins with $I = 1/2$, they can be used for a semiquantitative understanding of the NMR experiments discussed below. The more exact treatment of the spin dynamics requires the knowledge of the spin Hamiltonian and the formalism of the density operator [66, 67].

5.2 Used sequences

The pulse sequences in figure 5.1 have been used for observing the NMR of endohedral hydrogen fullerenes.

(a) One-pulse sequence. A single $\pi/2$ pulse is followed by the acquisition of the NMR signal, i.e. $\pi/2-$acq. The main limitation of this pulse sequence is that the signal acquisition cannot start immediately after the pulse. The high power pulses used to excite the nuclear spin have not ideal rectangular shape and the hardware needs some extra time beyond the nominal pulse duration to reduce the power to zero. The receiver is very sensitive and can be damaged if it is opened before the exciting pulse is extinguished. This extra time is called the dead time and it is usually few μs in modern spectrometer. Also ring-down of the probe can be collected if the acquisition is started too close to the end of a strong pulse. These delays may lead to signal distortions in the case of rapidly decaying NMR signals. In such cases, spin echoes may be useful (see below). ^{1}H NMR spectra of static powders are often broad and uninformative, due to the anisotropic dipole-dipole couplings. However, $H_2@C_{60}$ displays well defined and informative static proton lineshapes due to the relative isolation of the endohedral H_2 molecules.

(b) Solid echo [68]: $(\pi/2)_0-\tau/2-(\pi/2)_{\pi/2}-\tau/2-$acq. This pulse sequence generates a spin echo for isolated spin-1/2 pairs, which is the approximate situation for the endohedral ortho-H_2 molecules. The second pulse reverses the rapid signal decay caused by the intra-pair dipole-dipole coupling, leading to a dipolar spin echo. The delay $\tau/2$ is chosen to be larger than the dead time to reduce distortion of the lineshape. Fourier

transformation of the signal is usually performed from the top of the echo to avoid a large first-order phase correction. This pulse sequence was used to check the lineshapes of the endohedral H_2 molecules at low temperatures.

(c) Saturation-recovery (SR): $\pi/2 - d_1 - \pi/2 \ldots - d_1 - \pi/2 - \tau - \pi/2$–acq. The longitudinal magnetization is reduced to zero by a train of $\pi/2$ pulses, separated by a small delay d_1. The magnetization partially recovers through spin-lattice relaxation during the interval τ, and is converted into transverse magnetization by the final $\pi/2$ pulse. The NMR signal after the final pulse is monitored as a function of the recovery delay τ, in order to determine the spin-lattice relaxation time constant T_1. Saturation recovery experiments can be repeated without waiting for several T_1 as in inversion recovery experiments. This is a definitive advantage at cryogenic temperatures when the T_1 becomes long.

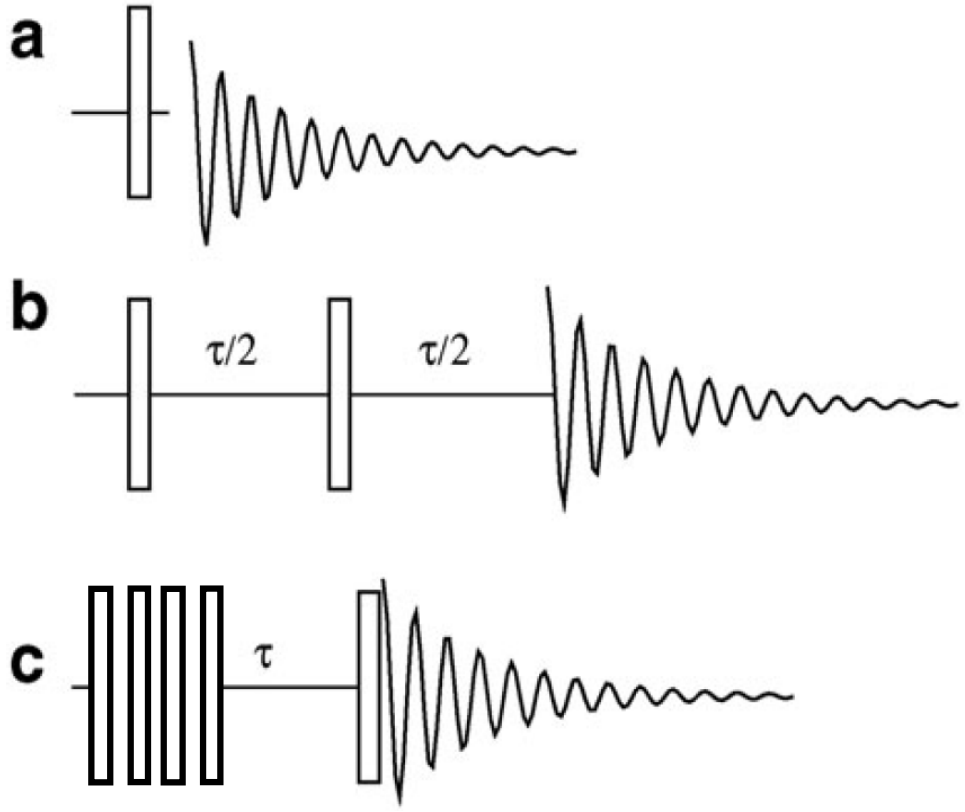

Figure 5.1: Pulse sequences used for the NMR experiments on endohedral hydrogen fullerenes. (a) One-pulse sequence; (b) Solid echo sequence. (c) Sequence for saturation recovery experiment.

5.3 NMR on $H_2@C_{60}$

A comparative NMR spectroscopy study has been conducted on two samples of $H_2@C_{60}$. Both samples were prepared following a multi-step molecular surgery procedure [22,

23]. The first sample, labeled I henceforth, was synthesized by the group of Komatsu and Murata at Kyoto University. The second sample, labeled II henceforth, was synthesized by the group of Turro at Columbia University in New York. After insertion of H_2 and reclosure of the fullerene, sample II was dissolved in CS_2 and then left under vacuum pumping for several days. $H_2@C_{60}$ recrystallized in the form of 1 cm long black 'needles' in contrast to normally prepared fullerene samples which look like a brownish powder. A small amount of $H_2@C_{60}$, 1.1 mg for sample I and 0.3 mg for sample II, was packed in standard zirconia Varian 4 mm rotors for magic-angle spinning (MAS) NMR experiments. For static NMR experiments low-proton content pyrex glass tubes were filled with approximately 3-5 mg of material.

5.3.1 ^{1}H NMR spectra

Magic angle spinning (MAS) spectra were recorded to establish the amount of protonated impurities in the two samples. figure 5.2. MAS is useful to clearly distinguish the endohedral proton signal from exohedral protons. Endohedral atoms/molecules have a characteristic negative chemical shift due to the shielding of the fullerene cage [22, 69]. The spectra were referenced setting the proton signal of adamantane at 1.8 ppm. In the figure the main peaks correspond to endohedral hydrogen while the other peaks correspond to occluded protonated solvents, likely toluene, which are repeatedly used in the synthesis of the material. In sample II the broad background comes from the protons in the rotor. MAS spectra proved that both samples contained a limited amount of occluded protonated impurities and that the NMR signal in static experiments is determined almost exclusively by endohedral hydrogen.

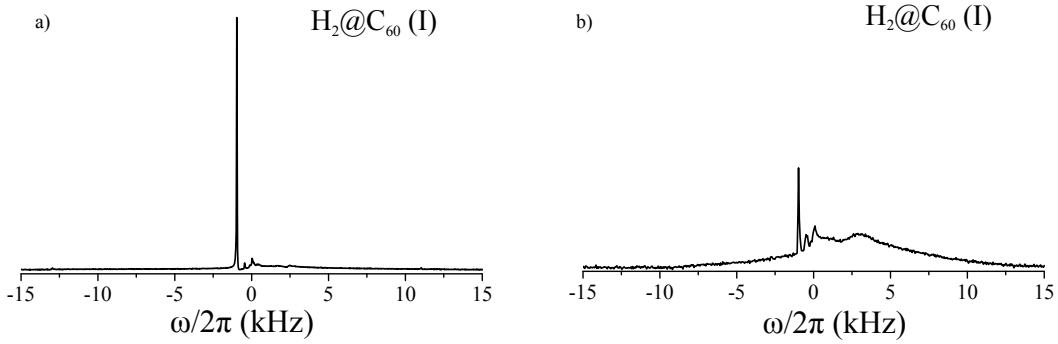

Figure 5.2: Room temperature ^{1}H MAS spectra of the two $H_2@C_{60}$ samples (I and II) at 9.4 T: the spinning speed was 12 kHz in both experiments. The spectrum for sample I, on the left, is an average of 64 scans while the spectrum for sample II, on the right, is an average of 512 scans. The vertical scale is arbitrary. The highest peaks at -0.71 kHz are from endohedral hydrogen. The other peaks correspond to occluded protonated impurities. The broad peak in sample II is originated from the protons of the rotor: the background is visible because only ≈ 0.3 mg were used for sample II in comparison to 1.1 mg for sample I.

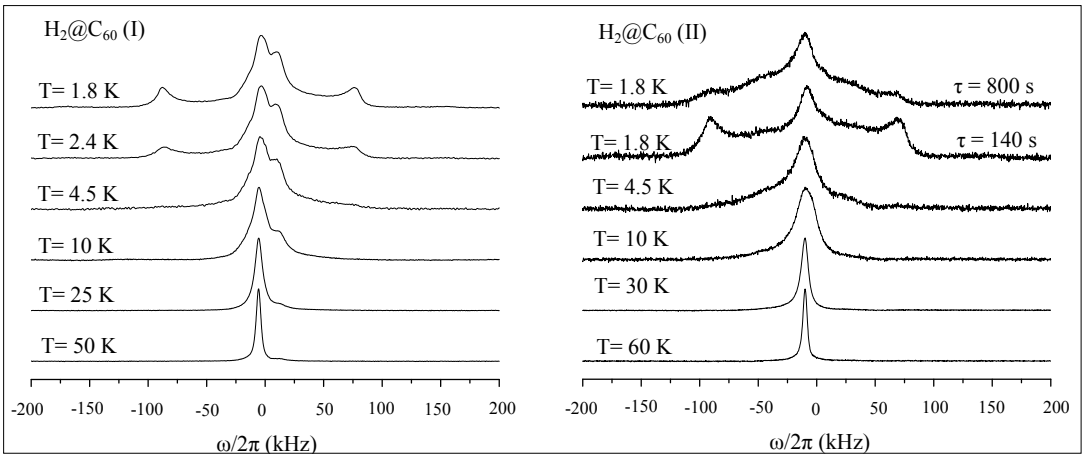

Figure 5.3: Temperature dependence of ^{1}H spectra in $H_2@C_{60}$ (sample I and II) at 14.1T under static conditions (no MAS). In all the experiments the center frequency is 600.435033 MHz. The dead time before acquisition was 5 μs and the dwell time was 1 μs. For sample I the spectra are averages of 2 scans. The duration of the flip pulse was 3.1 μs for temperatures above 10 K, corresponding to a flip angle of $\pi/2$ radians. Below 10 K the duration of the flip pulse was reduced to 0.6 μs corresponding to a flip angle of $\approx \pi/6$ radians. For sample II one scan spectra are displayed. The spectra were collected using flip pulses of $\pi/2$ with a duration of the pulse 2.5μs. For sample II two spectra are shown at 1.8 K: they were acquired after a delay from the saturation pulses of 140 s and 800 s, respectively.

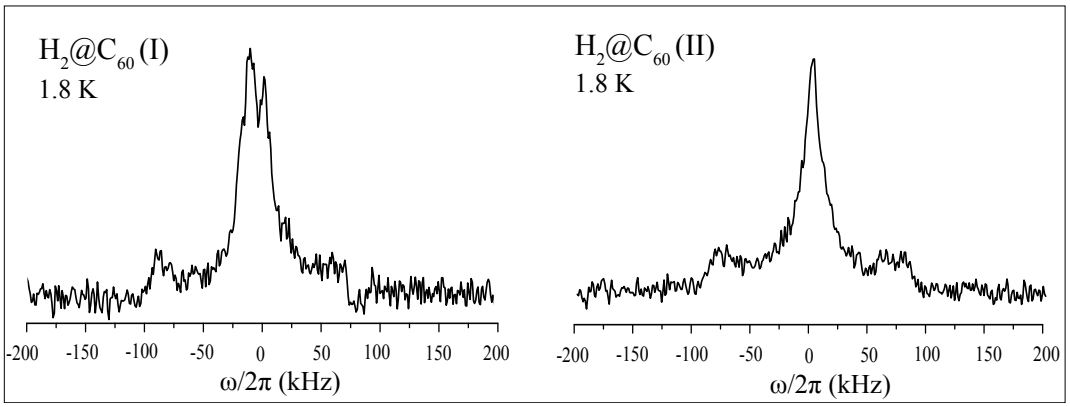

Figure 5.4: Solid echo ^{1}H spectra (on bottom) of $H_2@C_{60}$ at 14.1T and 1.7 K under static conditions (no MAS) for sample I and II. For sample I just one scan was acquired: the duration of the echo pulses was 3.1μs separated by $\tau/2 = 65\mu$s. The spectrum for sample II is an average of four scans with recycle time 20 s: the duration of the echo pulses was 2.1μs separated by $\tau/2 = 160\mu$s.

Static proton spectra of $H_2@C_{60}$ were collected from room temperature to 1.8 K using a 14.1 T FT-spectrometer with cryogenic capability, see figure 5.3. For both samples the ^{1}H spectra consist of a single narrow line at any temperature down to 10 K. The line fitted a Gaussian shape. The half width at half height (HWHH) of the line increases when the temperature is reduced: from approximately 3 kHz at 300 K to 15 kHz at 10 K. Below 10 K the NMR behavior of the two samples shows some substantial differences. In sample I at 10 K a shoulder appears on the right of the central main peak, shifted at a frequency 11 kHz higher. The shoulder becomes more

and more evident at lower temperatures while the intensity of the central peak spreads over a wider region. At temperatures below 2.4 K the broad region at the bottom of the spectrum gets more defined: the line is symmetric with respect to the main central peak and 164 kHz peak to peak wide. At 1.7K two very weak wings twice as large are barely visible. These features are associated with a dipolar Pake pattern for ortho-hydrogen in the rotational ground state J=1. This topic will be discussed in more detail after introducing the ortho-H_2 spin Hamiltonian. In the spectra of sample II there is no evidence of any shoulder beside the central peak at any temperature. Below 10 K the spectra in sample II are slightly broader than in sample I. At 1.8 K a Pake pattern emerged at the bottom of the central peak with the same characteristics as for sample I. For delays longer than 200 s the most prominent part of the lineshape is a very broad component emerging in the center part of the spectrum. It must be noted that below 10 K a complete recovery of part of the NMR signal is achieved for delays exceeding 1000 s. Quadrupolar echo sequence [68] confirmed that the 1.8 K lineshapes, described above, were related to nuclear magnetic resonance rather than to instrumental artifacts. In the solid echo spectra, figure 5.4, the most prominent feature is given by a central peak. In sample I the shoulder observed by one-pulse experiment is still clearly visible. As expected the dipolar pattern was refocused by the echoes and is evident in both samples.

5.3.2 ^{1}H spin-lattice relaxation: analysis and results

A detailed experimental study of the spin-lattice relaxation time in $H_2@C_{60}$ at various magnetic field and over a wide temperature range has been published [69]. The scope of the present study was not to reproduce previous results but to determine if the nuclear spins relax homogeneously through the sample or wether more components can be identified and eventually related to any specific features in the low temperature spectra.

Spin lattice relaxation times were obtained from the analysis of saturation recovery experiments. According to equation (5.6a), after a delay τ from the end of the train of pulses the z-magnetization recovers following the law

$$M_Z(\tau) = c + \sum_i M_{0,i}(1 - e^{-\frac{t}{T_{1,i}}}). \tag{5.7}$$

The sum is over the different components of the spin system in the sample, each with its own relaxation time $T_{1,i}$. The constant $c = \sum_i M_{Z,i}(0)$ takes into account the possibility of a small residual magnetization due to incomplete saturation. The observed NMR signal is proportional to the recovered magnetization $M_Z(\tau)$. When the components fall in distinct resonances of the NMR spectrum, the relaxation times can be obtained by matching the recovery of the intensity of each peak to a single exponential. In practice some components may resonate at the same frequency or very close to each other and

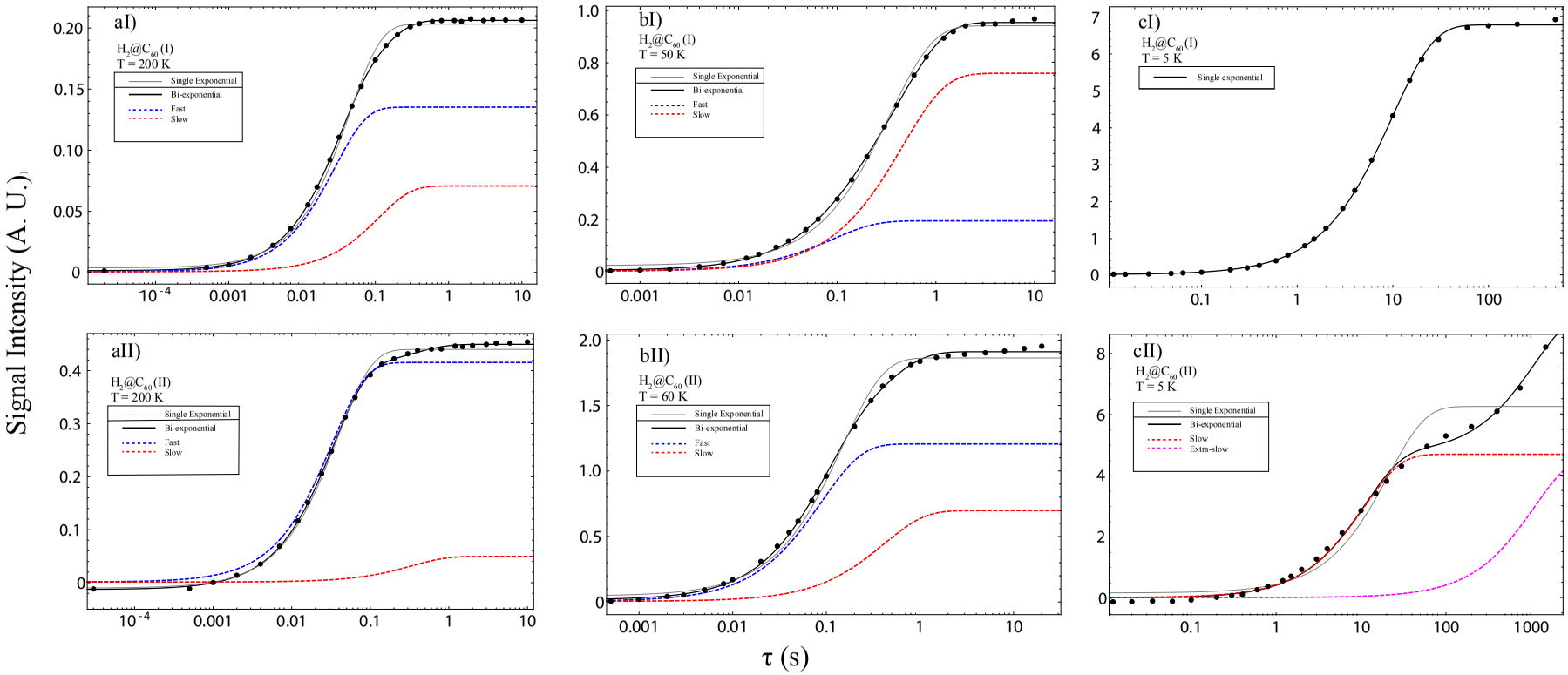

Figure 5.5: Examples ^{1}H saturation recovery curves for $H_2@C_{60}$ samples at 14.1 T and at three different temperatures: sample I is on the top, panels aI) to cI), and sample II is on the bottom, panels aII) to cII). Experimental peak areae are represented by black circles and the best fit to an exponential recovery is represented by a black solid line. Whenever the fit is to a multi -exponential recovery with $n > 1$ components, each component of the best fit is reported as dashed line. Also the best fit to a multi exponential with $n - 1$ components is reported for comparison as gray solid line. The intensity units on the vertical axis are arbitrary but the vertical scale is the same in plot aI) to cI) and aII) to cII) respectively.

then fall under one peak because of instrumental limitations or intrinsic line broadening effects. In such a case the number of components can be established by matching the recovery curve of the resonance to a multi-exponential recovery. The reliability of the relative intensities and relaxation times obtained from analysis of the recovery curve depends on the quality of the experimental data.

Figure 5.5 shows typical saturation recovery curves of the proton signal for samples I and II at three different temperatures. Sample I shows a bi-exponential recovery from 300 down to 50 K with a fast relaxing component (T_1 order of tens of ms) and a slightly slower one (T_1 order of hundreds of ms). The ratio of the signal is in favor of the short component for high temperatures but the situation is reverted below 100 K. At lower temperatures the fast component is decreasingly important and the recovery becomes single exponential. Sample II has a similar relaxation behavior between 300 and 50 K: a fast and a slow component are present with relaxation times consistent with the ones in sample I. The ratio of the equilibrium magnetization of the short component to that of the long component in sample II is different than in sample I but it follows the same temperature trend: it is reduced when the temperature lowers. Most importantly a very slow relaxing component appears at around 30 K and gets increasingly larger below. The presence of a large component with very long relaxation time hampered the exact measurements of spin lattice relaxation times at low temperature in our experimental setup where only a limited supply of helium was available per experimental session. The situation is particularly evident at 4.8 K, in figure 5.5IIc). Here two components, a slowly relaxing component and an extremely slow relaxing component can be discerned. From the analysis of the partially recovered signal at 4.8 K the estimated T_1 of the extra-slow component is $\approx$ 2000s, i.e. two orders of magnitude longer than the other component present. A general consideration about saturation recovery experiments needs to be done here. According to equation (5.2) the equilibrium magnetization depends linearly on the inverse of the temperature (Curie law). $H_2@C_{60}$ makes no exception as it has been observed experimentally [69]: since the rate of ortho-para conversion is very small (in absence of paramagnetic impurities) there is no deviation of the NMR signal from the Curie law during a few-days-long experimental session. For each of the $H_2@C_{60}$ samples studied here the experimental conditions were kept homogeneous at different temperatures. One of the criteria used to establish when the magnetization was fully recovered at low temperatures was to compare the integrated intensity of the NMR signal with that expected from the high temperature spectra. In sample I the signal was found to have recovered almost completely to the expected value at any temperatures within less than 100 s after the saturation pulses. If the slow relaxing component was missed for sample I because the recovery delay was not extended sufficiently, its contribution could estimated to be less than 10% of the total NMR signal. The temperature dependence of spin-lattice relaxation times from the analysis of saturation recovery experiments is summarized in figure 5.6.

It is worth comparing the recovery of the ^{1}H NMR signal at 1.8 K for the two

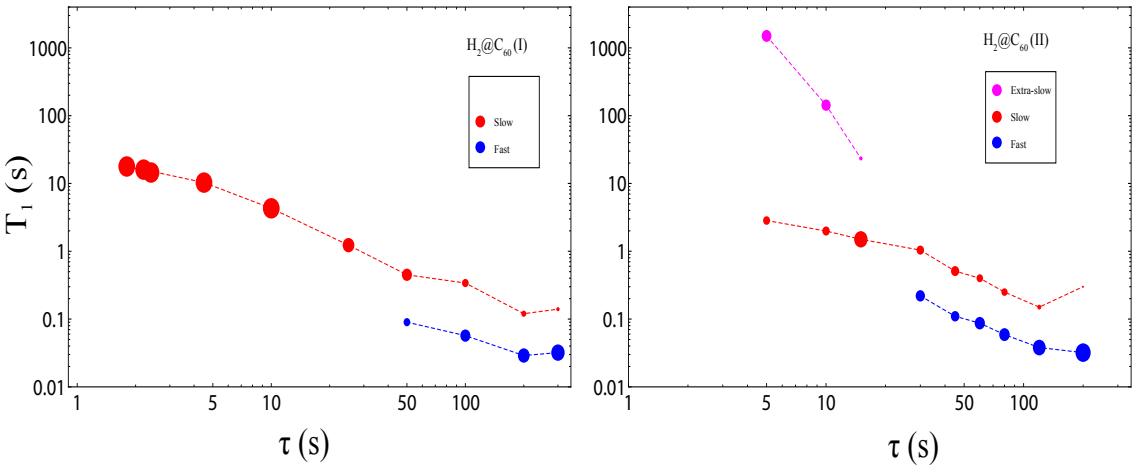

Figure 5.6: Temperature dependence of ^{1}H spin lattice relaxation time T_1 in $H_2@C_{60}$ at 14.1 T under static conditions (no MAS): sample I is on the left and sample II is on the right. The dots are experimental points. The size of the points is proportional to relative weight of the component in the NMR signal. For sample I between 1.7 and 10 K the relaxation times seem to follow a simple power law dependence $T_1 \propto T^{-0.7}$ (dashed line). At higher temperature the analysis of the saturation recovery curve indicate that there are two components, a fast relaxing (blue dots) and a slow relaxing one (red dots). For sample II the situation is similar at high temperature but at low temperature the most relevant part of the signal comes from an extremely slow relaxing component (magenta dots).

samples, figure 5.7. In sample I the recovery is still single exponential with a relaxation time of 18 s: the main central peak, the smaller side peak and the dipolar pattern recover at the same rate. In sample II the recovery is only partial and the relaxation times can not be established with certainty. However it can be observed that the Pake pattern and the central peak grow at a similar rate up to 50 s and then only the central peak keeps increasing in intensity. A broader feature appears clearly below the central peak using 240 s delay. The slow relaxing part of the NMR signal is linked to this broader feature. The Pake pattern structure seems to have the same relaxation rate as in sample I (~20 s). These observations suggests that the local environment around each H_2 is homogeneous in sample I while in sample II there at least two components. Another possibility is that spin diffusion in sample I is more effective in leading to a common relaxation rate for the nuclear spins.

In conclusion the two samples behave similarly between 300 K and 50 K when there are two components with comparable relaxation rates. The relaxation behavior is different at low temperature where the relaxation of sample I can be described by a single exponential while in sample II there is evidence of a second extremely slow relaxing component. The analysis of the recovery curves at 1.8 K shows that the dipolar pattern relaxes at the same rate in both samples while the extra slow component in sample II relates to a broad feature visible in the center of the spectrum at long recovery delays.

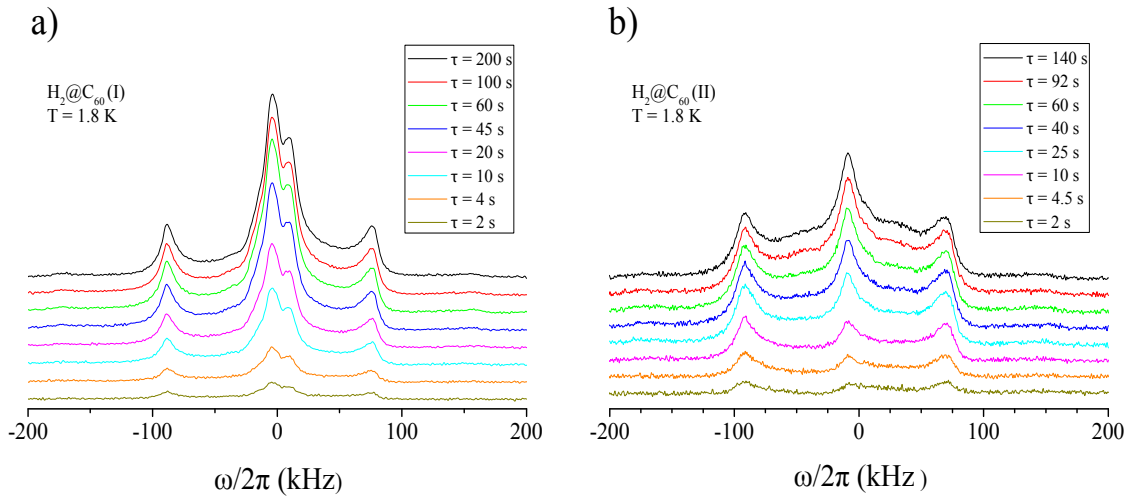

Figure 5.7: Saturation recovery ^{1}H NMR lineshapes of $H_2@C_{60}$ at 14.1T and 1.7 K under static conditions (no MAS) for various delays: sample I is on the left and sample II is on the right. In sample I the lineshape relaxes uniformly and the recovery is single exponential with a T_1 of 18 s ca. In sample II the lineshape relaxes with two different rates at the side of the Pake Pattern and at the center, respectively. The Pake pattern relaxes with a time constant of 20 s ca. The time constant of the broad peak could not be evaluated properly since recovery is not reached within 200 s but it is expected to exceed 2000 s.

5.4 mK experiments on $H_2@C_{60}$

The NMR spectroscopy of $H_2@C_{60}$ was studied at temperatures below 2 K using a FT-NMR spectrometer equipped with a mK refrigerator made available by John Owers-Bradley at the University of Nottingham, UK. The hardware and the electronic for NMR at mK temperatures are similar to the ones used in 'high' temperatures FT-NMR spectroscopy. Temperatures between few mK and 2 K are achieved by using a ^{3}He-^{4}He dilution refrigerator whose working principle is based on the phase diagram of the helium mixture. The experimental setup is described in [70]. The experimental apparatus was a KelvinoxLTM Oxford Instrument refrigerator with a top loading probe and equipped with cryogenic solenoids. The solenoids could provide a magnetic field from 2.5 up to 15 T. All the measurements reported here were performed at 2.9 T. Low temperatures were maintained for a long time by operating the closed cooling system cyclically. The temperature was monitored using a calibrated RuO_2 resistor placed in the maxing chamber near the sample. A 2mm glass tube open on one side was filled with 5mg of $H_2@C_{60}$ from the batch labeled II. The open side was covered with teflon tape to avoid dispersing the sample during measurements in liquid He.

The NMR spectra were obtained using one-pulse sequence and the spin lattice relaxation times were obtained using a saturation recovery sequence. In all the experiments the center frequency of the spectrometer was kept at 123.720 MHz, the dead time was 2-4 μs and the dwell time for acquisition was 0.25 μs. The power of the resonant field was calibrated so to reach a flip angle of $\pi/2$ with a pulse of 20 μs. Observe pulses 1 μs

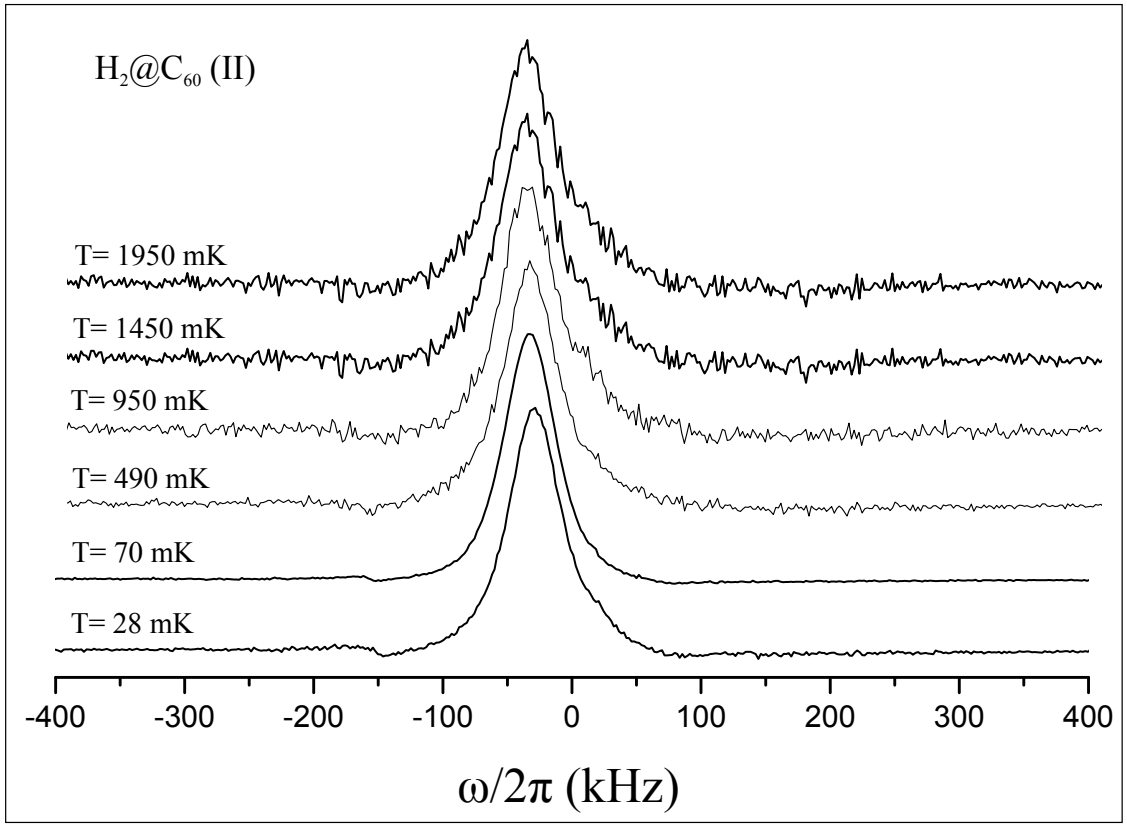

Figure 5.8: Temperature dependence of ^{1}H line shape in $H_2@C_{60}$, sample II, at 2.90 T. No change is observable in the line shape. The width of the line at half height is 50 kHz.

long have been used, corresponding to a tipping angle $\theta \approx 5°$.

Due to the very long relaxation time at low temperatures it was impractical to wait for the magnetization to equilibrate before repeating the measurements. Spectra were recorded sequentially by repeating several times a basic cycle of excitation-acquisition-delay with T_2«delay«T_1. The amplitude of the signal diminished slowly but continuously from one experiment to the next and more than 100 excitation pulses were necessary to reduce it to half of its initial value. The lineshape did not show appreciable changes during the continuous acquisition experiment. Figure 5.8 show representative spectra, average of 32 consecutive acquisitions, from 2 K to 28 mK. Only a single line 50 kHz broad is visible at all temperatures down to 28 mK. Interestingly there is no evidence of any dipolar powder pattern in the spectra.

Spin-lattice relaxation times were obtained in a similar manner. The recovery of the signal was monitored at successively longer delays saturating the longitudinal magnetization only once at the beginning of the experiment. For small tipping angle of the observe pulse the magnetization at the $i-th$ delay measured in this way is scaled by factor $(\cos\theta)^{i-1}$ with respect to the one obtained in a regular saturation recovery experiment. The integrals of the experimental spectra were corrected to take into account

this factor and then fitted to a single exponential recovery, equation (5.7). Major deviations from exponential behavior were not observed and the contributions of minor components could not be assessed properly due to the reduced signal to noise ratio for one scan acquisitions. The temperature dependence of the spin-lattice relaxation times is summarized in figure 5.9. As expected the relaxation time gets longer at lower temperatures: for temperature higher than 1 Kelvin the relaxation time is few minutes but it is longer than 1 day below 100 mK. Using a log-log representation the relaxation times appeared aligned according to an inverse power law with different exponents for the low and the high temperature end, respectively. A least chi-square fit of the data to the model $1/\mathrm{T}_1(T) = A\,T^{n_1} + B\,T^{n_2}$ gave the following values $n_1 = 1.0 \pm 0.3$, $n_2 = 3.0 \pm 0.2$, $A = (2.0 \pm 1.5) \times 10^{-5}\mathrm{s}^{-1}$, $B = (14 \pm 2) \times 10^{-5}\mathrm{s}^{-1}$. At temperatures higher than 0.9 K the relaxation times are proportional to T^{-3}. At lower temperatures the relaxation times are consistently shorter than what expected according to T^{-3} law and below 200 mK are proportional to T^{-1} .

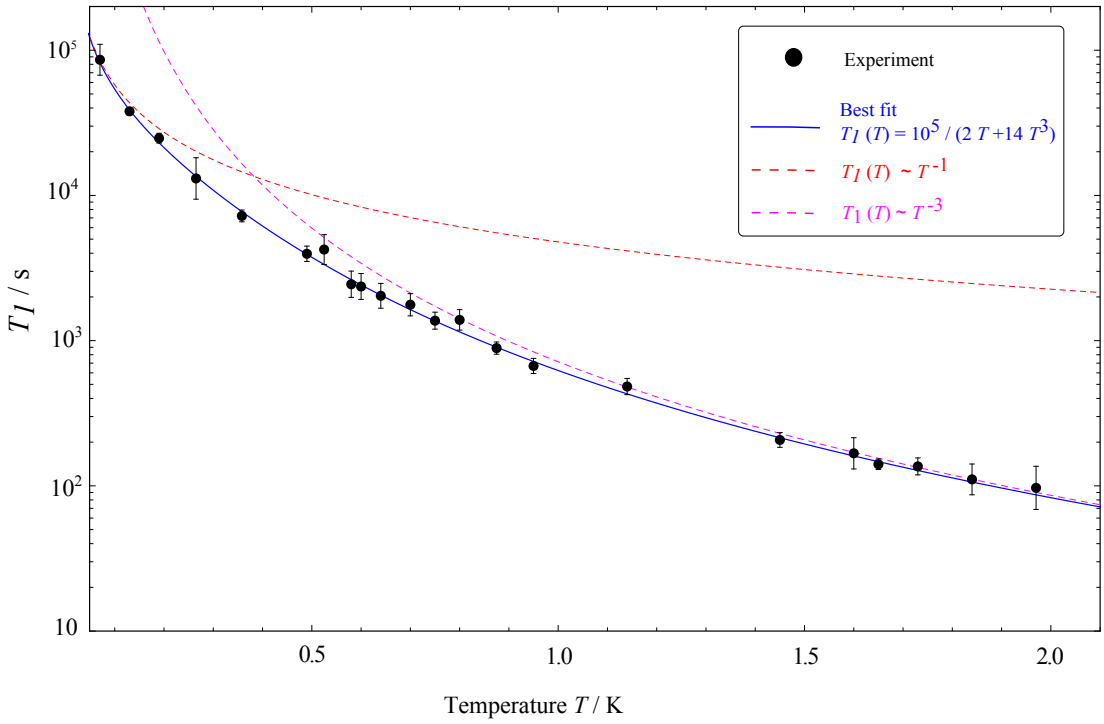

Figure 5.9: Temperature dependence of ^{1}H spin lattice relaxation time in $H_2@C_{60}$, sample II, at 2.90 T. The black points are experimental data and the blue line is the best fit to $1/\mathrm{T}_1(T) = A\,T^{n_1} + B\,T^{n_2}$. The relaxation times T_1 follow a T^{-1} power law on the low temperature side (red dashed line) and T^{-3} power law on the high temperature side (magenta dashed line).

The results reported in this section are consistent with the observations at higher magnetic field. The lineshape observed in the experiments at 2.9 T reminds of the broad slow-relaxing bump observed at 14.1 T, figure 5.7(II). The measured $\mathrm{T}_1 = 110$s at 2.9 T and 1.8 K is consistent with the estimated $\mathrm{T}_1 \sim 2000$ s for the slow-relaxing component

at 14.1 T and at the same temperature assuming that the relaxation times scale with the square of the magnetic field. However the absence of an observable dipolar pattern in the mK spectra is surprising. Indeed the dipolar pattern observed in the lineshape in a field of 14.1 T and 1.8 K should become more definite at lower temperatures due to a larger population difference among the sublevels in the ground state of ortho-H_2. The asymptotic signal intensity at long delays is shown to follow the Curie law, equation (5.2), implying no evident spin conversion during the experimental session.

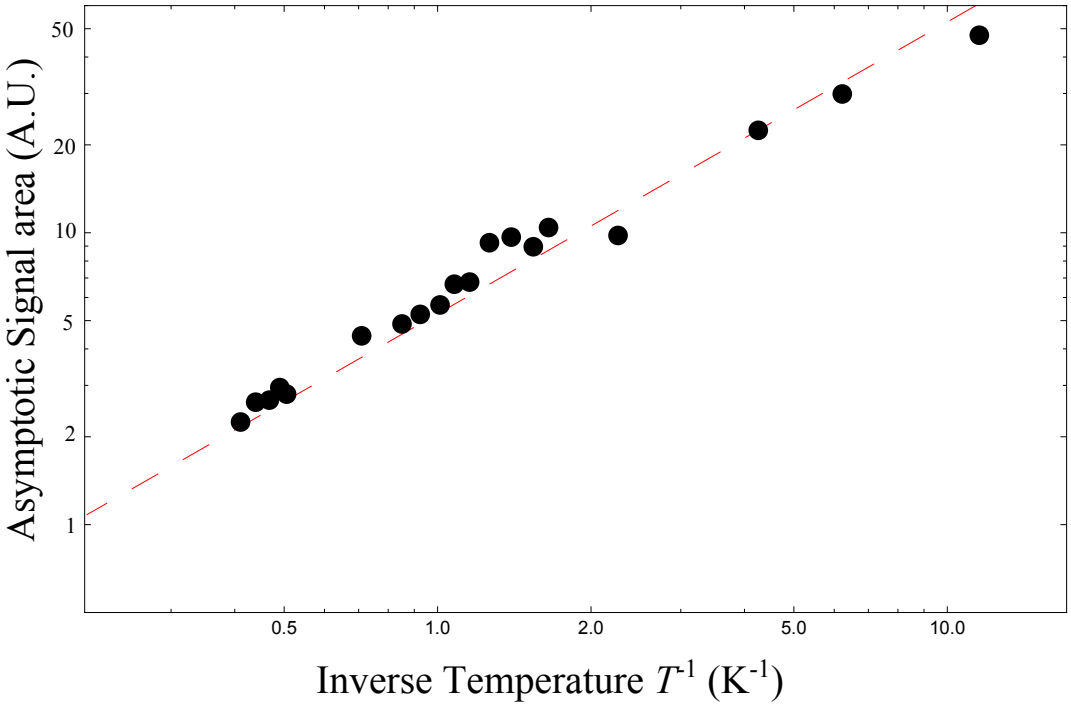

Figure 5.10: Temperature dependence of the NMR signal intensity for $H_2@C_{60}$ between 2 and 0.1 K at 2.9 T. The points represent the asymptotic value $M(+\infty)$ from the analysis of saturation recovery experiments, compare equation (5.7). The dotted line is the Curie law $M_0 \propto 1/T$.

5.5 Conclusions

The NMR spectra and spin-lattice relaxation times of two $H_2@C_{60}$ samples with different preparation history were studied at various temperatures in a field of 14.1 T. The two samples show a similar response between 300 and 10 K: spectra consist of a narrow line and relaxation times are order of 10 ms. Below 5 K a powder Pake pattern becomes apparent at the base of the prominent narrow peak in the spectra of both samples. The presence of such a pattern proves that the degeneracy of the ground state of ortho-H_2 is lifted at least in part of the sample. At low temperature the different relaxation behavior of the two samples is striking. In sample I all the observed features in the NMR line

relax uniformly according to a single exponential law with a characteristic time of ≈ 20 seconds. In sample II there are two components with different relaxation rates. The largest part of the signal comes from a slow relaxing component, $T_1 \cong 2000$s associated to a broad feature visible in the NMR spectrum at 1.8 K. These differences have not been understood yet. They may be related to impurities trapped in the voids between cages during the synthesys or later manipulations of the material. For example it has been observed that solid C_{60} intercalates easily oxygen at normal conditions particularly under illumination with UV/VIS light [71, 72]. The NMR of $H_2@C_{60}$ in sample II was then studied at 2.9 T between 0.02 and 2K. In this range of temperatures the spectrum consists a 50 kHz broad line with no other evident feature, the relaxation is single exponential and $1/T_1(T) \propto (AT + BT^3)$.

Chapter 6

Nuclear spin dynamics for $H_2@C_{60}$

6.1 NMR Hamiltonian

In this section the ^{1}H NMR Hamiltonian for ortho-H_2 in its vibrational-rotational-translational ground state will be discussed. The starting point is the molecular beam Hamiltonian of ortho-H_2 in the rotational state $J = 1$ in a magnetic field B_0. As shown by Ramsey and coworkers [73, 74], the Hamiltonian contains four terms: one Zeeman term for the nuclear spin $\boldsymbol{I}$ and one Zeeman term for the rotational angular momentum $\boldsymbol{J}$ describing the respective coupling with the magnetic field; a term describing the spin-rotation interaction and a term describing the dipolar interaction between the two protons. In spherical tensor notation that is:

$$\mathcal{H}_{\boldsymbol{I}-\boldsymbol{J}} = \omega_{\mathrm{H}} T_0^1(\boldsymbol{I}) + \omega_{\mathrm{J}} T_0^1(\boldsymbol{J}) + \omega_c T^1(\boldsymbol{I}) \cdot T^1(\boldsymbol{J}) + \frac{3}{5}\omega_d T^2(\boldsymbol{I}) \cdot T^2(\boldsymbol{J}) \tag{6.1}$$

where spherical tensors and scalar product are defined in 2.3. The Larmor frequencies are $\omega_{\mathrm{H}} = -\gamma_{\mathrm{H}} B_0$, $\omega_{\mathrm{J}} = -\gamma_{\mathrm{J}} B_0$ and the gyromagnetic ratios are $\gamma_{\mathrm{H}} = 267.513\,\mathrm{MHz\,T^{-1}}$, $\gamma_{\mathrm{J}} = -42.200\,\mathrm{MHz\,T^{-1}}$, respectively. The spin-rotation coupling is $\omega_c \approx -715.680\,\mathrm{kHz}$. The dipolar coupling is $\omega_d = \mu_0 \gamma_{\mathrm{H}}^2 \hbar/(4\pi r^3)$ with an approximate value of $\omega_d \approx 1.8623$ MHz for $r = 0.74$ Å [74]. The molecular beam Hamiltonian in equation (6.1) describes two interacting spins-1: the nuclear spin $\boldsymbol{I}$ and the *molecular* spin $\boldsymbol{J}$ associated with molecular rotations. In high magnetic field the spin-rotation and the dipolar Hamiltonians are smaller than the Zeeman part and the full Hamiltonian can be truncated for the purpose of finding the eigenvalues of the system

$$\mathcal{H}_{\boldsymbol{I}-\boldsymbol{J}} \approx \omega_{\mathrm{H}} T_0^1(\boldsymbol{I}) + \omega_{\mathrm{J}} T_0^1(\boldsymbol{J}) + \omega_c T_0^1(\boldsymbol{J})\, T_0^1(\boldsymbol{I}) + \frac{3}{5}\omega_d T_0^2(\boldsymbol{J})\, T_0^2(\boldsymbol{I}) \tag{6.2}$$

The eigenvectors are the Zeeman eigenstates in the laboratory frame $|M_I, M_J\rangle$ with energies

$$E(M_I, M_J) = M_I\omega_{\mathrm{H}} + M_J\omega_{\mathrm{J}} + \omega_c M_I M_J + \frac{1}{10}\omega_d\left(3{M_I}^2 - 2\right)\left(3{M_J}^2 - 2\right) \tag{6.3}$$

The single quantum nuclear spin resonance can be found as transitions with $\Delta M_J = 0$ and $\Delta M_I = 1$. For each $M_J = -1, 0, 1$ there are two transitions at frequency $\omega(M_J)/(2\pi)$ for a total of six resonances:

$$\frac{\omega(M_J)}{2\pi} - \frac{\omega_{\mathrm{H}}}{2\pi} = \frac{\omega_c}{2\pi}M_J \pm \frac{3}{10}\frac{\omega_d}{2\pi}\left(3{M_J}^2 - 2\right). \tag{6.4}$$

In high field approximation the position of the resonances in the ^{1}H NMR molecular depends on ω_c and ω_d. A simulated spectrum with the corresponding energy level structure is reported in figure 6.1. Such a spectrum has been actually observed in molecular beam experiments on hydrogen [74]. The resonances are narrow because collisions between molecules in collimated molecular beams are infrequent (on the NMR time scale). A spectrum like the molecular beam one is expected to be observed also for H_2 confined in highly symmetric environments when broadening effects and rapid exchange among the rotational sublevels, characterized here by M_J, are negligible.

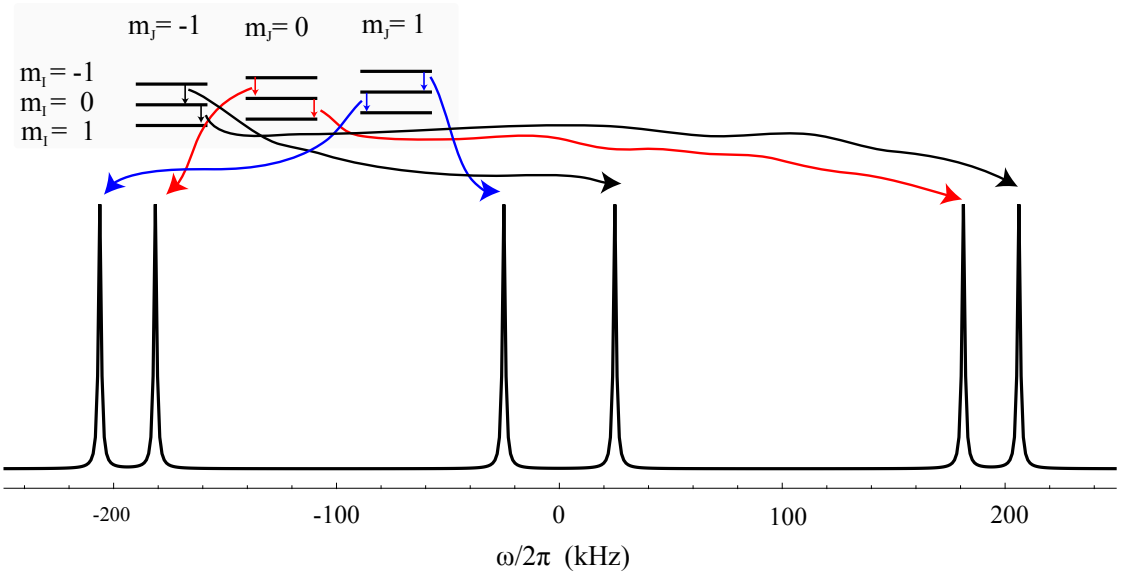

Figure 6.1: Simulated ^{1}H spectrum for H_2 in molecular beam nuclear resonance experiment at high field. The lines represents the energy level structure. Each single quantum resonance is assigned to a specific transitions with $\Delta M_I = -1, \Delta M_J = 0$. The lines were artificially broadened by multiplying the time domain signal by an exponential decay. The spectrum is centered at the proton Larmor frequency ω_{H}.

6.1.1 Hamiltonian in the confined case

In the isolated $H_2@C_{60}$ molecule the energy levels are not labeled by the rotational quantum number J but by the values of the total orbital angular momentum Λ. The rotational J and orbital L quantum numbers are still good quantum numbers for the levels because of the smallness of anisotropic interactions compared to the rotational and translational energies so that at lowest order the wavefunction is

$$\Psi_{N,JL}^{\Lambda,M_\Lambda} \approx \psi_{\text{tran}}^{N} F_{JL}^{\Lambda M_\Lambda} \tag{6.5}$$

neglecting the dependence on the vibrational quantum number v. These energy levels are degenerate in the quantum number M_Λ and have definite parity $(-1)^{L+J}$ under inversion.

The NMR Hamiltonian in the state with definite angular momentum equation (6.5) may be obtained from the molecular beam Hamiltonian replacing the rotational angular momentum $\boldsymbol{J}$ with $\boldsymbol{\Lambda}$ according to equation (2.38) with the use of equations (2.40) and (2.44):

$$\mathcal{H}_{\boldsymbol{I}-\boldsymbol{\Lambda}} = \omega_{\text{H}} T_0^1(\boldsymbol{I}) + \omega_\Lambda T_0^1(\boldsymbol{\Lambda}) + c_1 T^1(\boldsymbol{I}) \cdot T^1(\boldsymbol{\Lambda}) + c_2 T^2(\boldsymbol{I}) \cdot T^2(\boldsymbol{\Lambda}) \tag{6.6}$$

where

$$\omega_\Lambda = \alpha_{JL\Lambda 1}\omega_{\text{J}} \tag{6.7a}$$

$$c_1 = \alpha_{JL\Lambda 1}\omega_c \tag{6.7b}$$

$$c_2 = (-1)^J \alpha_{JL\Lambda 2} \frac{3}{(2J+3)(2J-1)} \omega_d \tag{6.7c}$$

and

$$\alpha_{JL\Lambda k} = (-1)^{J+L+\Lambda+k}(2\Lambda+1) \begin{Bmatrix} J & \Lambda & L \\ \Lambda & J & k \end{Bmatrix} \tag{6.8}$$

The important point is that the various interactions are scaled by a factor α depending on their rank and the angular momenta quantum numbers. In endohedral hydrogen fullerene the couplings, spin-rotation and dipolar, are rescaled according to the three angular quantum numbers in equation (6.7). Also the thermal distribution of the particles in excited states is clearly affected by quantization of the translational motion. In the ground roto-translational state of ortho-hydrogen ($J = 1, L = 0, \Lambda = 1$) there is no harm in replacing the rotational angular momentum $\boldsymbol{J}$ with $\boldsymbol{\Lambda}$ directly in equation (6.1) since the scaling factor is $\alpha_{101k} = 1$ independent of the rank of the operator. Scaling factors are relevant only for the analysis of nuclear spin relaxation at high temperature, when excited translational energy levels become populated. In the remaining of the chapter only the spin dynamics of the ground state will be considered.

In the solid state there are electric field gradients depending on the microscopic

packing of the molecules. Hydrogen molecules with non zero angular momentum have a quadrupole moment which is sensitive to such gradients. In undiluted endofullerene samples the distribution of ortho and para molecules is also relevant owing to the electric field generated by hydrogen molecules with non-null quadrupole moments in the nearby cages. In solid hydrogen the distribution of spin isomers determines essentially the rotational spin dynamics [75]. However the influence of the local fields on the dynamics of confined hydrogen can be described by a simple effective Hamiltonian independently of its fundamental physical origin. In solid $H_2@C_{60}$ the local field may reduce the symmetry of the Hamiltonian compared to the isolated molecule case. This can induce splittings of the sub-rotational energy levels which are directly observable by infrared or neutron scattering spectroscopy. Low and high temperature IR experiments [59, 60] and inelastic neutron scattering experiments [64] show that the splittings induced by crystal field on the energy levels of $H_2@C_{60}$ in the solid phase is no more than 2 cm^{-1} (60 GHz). This is confirmed also by specific heat studies on $H_2@C_{60}$ [76]. Such observations put an upper limit on the magnitude of the local fields. The local fields can be treated as small perturbation of the confining potential of the fullerene and can be expanded in multipoles $F_{lj}^{\lambda m}$. Since in ortho-$H_2@C_{60}$ the lower energy levels are composed essentially by states with $\Lambda = 1$ the only spherical multipoles that are relevant in the study of the spin dynamics can be effectively replaced by rank 2 spherical operators in the angular momentum $\mathbf{\Lambda}$. The effective local field Hamiltonian has the standard form of the interaction of a quadrupolar nuclei with an electric field gradient:

$$\mathcal{H}_{Q_\Lambda} = \delta \left\{ T_0^2 (\mathbf{\Lambda}_P) + \eta \left[T_2^2 (\mathbf{\Lambda}_P) + T_{-2}^2 (\mathbf{\Lambda}_P) \right] \right\} \tag{6.9}$$

where $\mathbf{\Lambda}_P$ correspond to the angular momentum in the principal axis frame of the interaction and $\Omega_{L\to P}$ is the set of three Euler angles determining the orientation of principal axis frame of the interaction with respect to the laboratory frame. The principal axis frame is defined as the frame where the only non null Cartesian component $V_{XX}^{\text{C.-F.}}, V_{YY}^{\text{C.-F.}}, V_{ZZ}^{\text{C.-F.}}$ are on-axes. The parameter $\delta = V_{ZZ}^{\text{C.-F.}}$ is related to the size of the crystal field and the parameter $\eta = (V_{YY}^{\text{C.-F.}} - V_{XX}^{\text{C.-F.}})/V_{ZZ}^{\text{C.-F.}}$ is related to the deviation from the axial symmetry. $0 \leq \eta \leq 1$ with the choice of the axes such that $|V_{XX}^{\text{C.-F.}}| \leq |V_{YY}^{\text{C.-F.}}| \leq |V_{ZZ}^{\text{C.-F.}}|$. In terms of the angular momentum operator in the laboratory frame the spherical tensors in equation (6.9) are expressed by

$$T_m^2 (\mathbf{\Lambda}_P) = \sum_{m'=-2}^{2} T_{m'}^2 (\mathbf{\Lambda})\, D_{m',m}^2(\Omega_{L\to P}). \tag{6.10}$$

The full Hamiltonian for ortho-$H_2@C_{60}$ in its ground spatial state is

$$\begin{aligned}\mathcal{H}_{\boldsymbol{I}-\boldsymbol{\Lambda}}(\delta,\eta,\Omega_{L\to P}) = &\underbrace{\omega_{\mathrm{H}} T_0^1(\boldsymbol{I})}_{\mathcal{H}_{Z_{\boldsymbol{I}}}} + \underbrace{\omega_c T^1(\boldsymbol{I})\cdot T^1(\boldsymbol{\Lambda})}_{\mathcal{H}_{SR}} + \underbrace{\frac{3}{5}\omega_d T^2(\boldsymbol{I})\cdot T^2(\boldsymbol{\Lambda})}_{\mathcal{H}_{DD}} \\ &+ \underbrace{\omega_\Lambda T_0^1(\boldsymbol{\Lambda})}_{\mathcal{H}_{Z_{\boldsymbol{\Lambda}}}} + \underbrace{\delta\left[T_0^2(\boldsymbol{\Lambda}_P) + \frac{\eta}{\sqrt{6}}\left(T_2^2(\boldsymbol{\Lambda}_P) + T_{-2}^2(\boldsymbol{\Lambda}_P)\right)\right]}_{\mathcal{H}_{Q_\Lambda}}.\end{aligned} \tag{6.11}$$

For $H_2@C_{60}$ the spin system consists of the nuclear spin $\boldsymbol{I}$ coupled to the molecular rotational degrees of freedom of H_2 which in turn interact with the fullerene modes. $\boldsymbol{\Lambda}$ plays the role of an effective molecular spin. Figure 6.2 shows the various interactions in $H_2@C_{60}$. The nuclear spin $\boldsymbol{I}$ and the molecular spin $\boldsymbol{\Lambda}$ are interacting with the external magnetic field through the Zeeman Hamiltonians, $\mathcal{H}_{Z_I}$ and $\mathcal{H}_{Z_\Lambda}$. The molecular spin is subject to a local field $\mathcal{H}_{Q_\Lambda}$ which depends on the orientation of the crystalline frame with respect to the static magnetic field. The nuclear and molecular spin communicate through the dipolar $\mathcal{H}_{DD}$ and the spin-rotation $\mathcal{H}_{SR}$ interactions. In pure $H_2@C_{60}$ there is no obvious direct interaction between the nuclear spin and the fullerenes. The spin system interacts with the fullerene modes (lattice) only through the molecular spin.

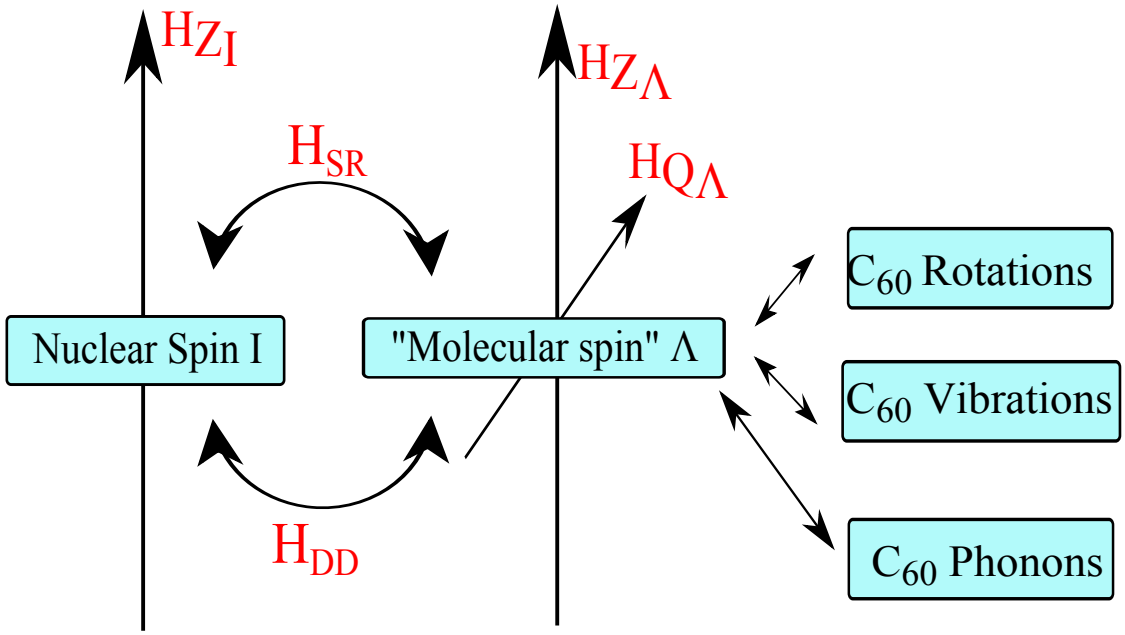

Figure 6.2: The cartoon shows the NMR interactions in $H_2@C_{60}$. The nuclear spin $\boldsymbol{I}$ of H_2 is subject to a Zeeman interaction $\mathcal{H}_{Z_I}$ with the magnetic field and is coupled to $\boldsymbol{\Lambda}$ by a smaller dipolar and spin rotation Hamiltonian. The molecular spin $\boldsymbol{\Lambda}$ is subject to a Zeeman interaction and a local field interaction and it is coupled to the C_{60} lattice (intramolecular vibrations, rotations, phonons).

6.2 NMR line

The NMR spectrum of H_2 in condensed phase is the result of the rotational energy level structure as determined by the crystal field, their thermal populations and the transition rates among these levels. At high field the NMR Hamiltonian is truncated in $\hat{\boldsymbol{I}}$ by the Zeeman Hamiltonian as

$$\mathcal{H}_{\boldsymbol{I}-\boldsymbol{\Lambda}} \approx \omega_{\mathrm{H}} T_0^1(\boldsymbol{I}) + \omega_c T_0^1(\boldsymbol{I})\, T_0^1(\boldsymbol{\Lambda}) + \frac{3}{5}\omega_d T_0^2(\boldsymbol{I})\, T_0^2(\boldsymbol{\Lambda}) + \underbrace{\omega_\Lambda T_0^1(\boldsymbol{\Lambda}) + \kappa\omega_\Lambda\left[T_0^2(\boldsymbol{\Lambda}_P) + \frac{\eta}{\sqrt{6}}\left(T_2^2(\boldsymbol{\Lambda}_P) + T_{-2}^2(\boldsymbol{\Lambda}_P)\right)\right]}_{\mathcal{H}_\Lambda} \tag{6.12}$$

where the adimensional parameter $\kappa = \delta/\omega_\Lambda$ has been introduced. A quantitative analysis can be performed diagonalizing the rotational Hamiltonian $\mathcal{H}_\Lambda$ and studying the dependence of the eigenvalues and eigenstates on the parameters κ and η. The energy levels are determined by the weight of the crystal field $\mathcal{H}_{Q_\Lambda}$ with respect to the Zeeman rotational Hamiltonian. The task is complicated by the fact that there is also an orientational dependence on the Euler angle set $\Omega_{L\to P}$. For any orientation there are three eigenstates, denoted $|n_i(\Omega_{L\to P})\rangle, i = 1,2,3$ with energy $E_i(\Omega_{L\to P})$. In the following the dependence of n_i and E_i on $\Omega_{L\to P}$ will be understood. For each of the three rotational eigenstates there are two spin resonances:

$$\frac{\omega_\pm}{2\pi}(n_i) - \frac{\omega_{\mathrm{H}}}{2\pi} = \frac{\omega_c}{2\pi}\langle n_i|T_0^1(\boldsymbol{\Lambda})|n_i\rangle \pm \frac{3}{10}\frac{\omega_d}{2\pi}\langle n_i|T_0^2(\boldsymbol{\Lambda})|n_i\rangle \tag{6.13}$$

The two limiting cases $\eta = 1$ and $\eta = 0$ and large $|\kappa| >> 1$ can be discussed analytically. In the biaxial case η is exactly 1 and each of the $|n_i\rangle$ is also an eigenstate (with null eigenvalue) of the angular momentum operator projected along each of the three orthogonal axes in the quadrupolar Hamiltonian PAF, respectively. The expectation values of the projection of the angular momentum $\boldsymbol{\Lambda}$ along any direction on the $|n_i\rangle$ basis are null (angular momentum quenching) and the resonances are at:

$$\frac{\omega}{2\pi}(\beta_i) = \frac{\omega_{\mathrm{H}}}{2\pi} + \pm\frac{3}{10}\frac{\omega_d}{2\pi}(3M_{J_P}^2 - 2)\left(\frac{3\cos^2\beta_i - 1}{2}\right) \tag{6.14}$$

where $\beta_i, i = 1,2,3$ are the angles between the Z-axis of the laboratory frame and the orthogonal axes in the PAF of $\mathcal{H}_{Q_I}$. In the uniaxial case η is exactly 0 and the Z-axis of the principal axis frame of the quadrupolar interaction is the quantization axis for the $\hat{J}$ angular momentum so that $|n_i\rangle = |M_{JP}\rangle$. The resonances are at:

$$\frac{\omega}{2\pi}(\beta) = \frac{\omega_{\mathrm{H}}}{2\pi} + \frac{\omega_c}{2\pi}M_{JP}\cos\beta \pm \frac{3}{10}\frac{\omega_d}{2\pi}(3M_{J_P}^2 - 2)\left(\frac{3\cos^2\beta - 1}{2}\right), \tag{6.15}$$

where β is the angle between the Z-axis in the PAF of $\mathcal{H}_{Q_I}$ and the Z-axis in the laboratory frame.

The nuclear spin lineshape depends strongly on the dynamics of the rotational motion. For example when the external fluctuations induce slow relaxation of the rotational levels, the intensity of NMR lines at frequency $\frac{\omega_\pm}{2\pi}[n_i(\Omega_{L\to P})]$ is proportional to the population of the rotational level

$$p_{n_i}(T) = \frac{1}{Z(T)} \mathrm{e}^{-\frac{E(n_i)}{k_B T}}, \tag{6.16}$$

where

$$Z(T) = \sum_{i=1}^{3} \mathrm{e}^{-\frac{E(n_i)}{k_B T}} \tag{6.17}$$

is the partition function. The dependence of the intensity on the temperature T is small except when $T \leq E_i$. On the other side when the relaxation among the rotational level is fast, the three pairs of resonance blend into an average pair $\overline{\omega}_\pm$

$$\frac{\overline{\omega}_\pm}{2\pi}(\Omega_{L\to P}, T) - \frac{\omega_{\mathrm{H}}}{2\pi} = \frac{\omega_c}{2\pi} \sum_{i=1}^{3} \langle n_i | T_0^1(\mathbf{\Lambda}) | n_i \rangle p_{n_i}(T) \pm \frac{3}{10} \frac{\omega_d}{2\pi} \sum_{i=1}^{3} \langle n_i | T_0^2(\mathbf{\Lambda}) | n_i \rangle p_{n_i}(T) \tag{6.18}$$

It should be noted that at high temperature when the population are distributed uniformly over the subrotational levels, $p_{n_i}(T) = 1/3$, the NMR resonances collapse into a single line since the trace of the spherical operators is null. This corresponds to the classical view of the molecular hydrogen tumbling isotropically inside the cage. At lower temperature the difference in population is reflected into a lineshape with residual non null anisotropic interactions. Fast and slow exchange refers to the timescale of rotational relaxation compared to the timescale of the evolution of the NMR signal which in $H_2@C_{60}$ is order of μs.

In a solid powder the NMR spectrum is given by the superposition of the signal coming from a large number of crystallites covering all possible orientations. Assuming random orientations the spectrum is simulated by an average over the set of angles and weights that reproduce the NMR signal from a uniform distribution of crystallites over the sphere.

6.2.1 Lineshape simulations

The upper limit of 60 GHz for the size of the crystal field translates into a an upper limit of $|\kappa| < 600$ in a magnetic field of 14.1 T where $\omega_J \approx 100$ MHz. The space of parameters $|\kappa| < 600$ and $0 \leq \eta \leq 1$ is then divided into three zones. In the region $\kappa \leq 0.2$ and the quadrupolar Hamiltonian has negligible effects for any value of the biaxiality parameter η. The resonances show a very weak dependence on $\Omega_{L\to P}$ and

the spectrum is expected to be the similar to the molecular beam one, equation (6.4) and figure 6.1. In the intermediate band $0.2 \leq |\kappa| \leq 20$ the Zeeman and quadrupolar Hamiltonian have comparable size. In this region the rotational energy levels show a strong dependence on the crystallite orientation with interlevel crossing and the NMR resonances can not be predicted from analytical expressions. Finally the quadrupolar Hamiltonian is dominant in the region $|\kappa| > 20$. In any case the low-temperature spectra can be obtained by simulation. Figures 6.3 and 6.4 report simulations at 2 K of ^{1}H NMR spectra for $H_2@C_{60}$ in the slow and fast exchange limit. In all the simulations with $\eta = 0$ powder averaging was obtained by using the angular set GQβ8191 (Gaussian quadrature in beta), composed by 2048 β-orientations; in all the remaining simulations with $\eta \neq 0$ the set ROSELEB10100 (Regularized Octahedral Symmetry Expansion Lebedev), composed by 10100 $\{\alpha, \beta\}$ orientations, was used [77, 78].

In the slow exchange limit spin resonances for all the crystallites form a broad and rich lineshape. The influence of temperature on the populations of the rotational levels is more pronounced in the spectra with $\eta = 0$. The NMR lineshape is narrower in the fast exchange limit when thermal averaging among the subrotational levels is effective except for large local fields at $|\kappa| >> 1$. The uniaxial spectrum, $\kappa >> 1$ and $\eta = 0$, has been observed in NMR experiments on H_2 intercalated in solid C_{60}: hydrogen is trapped in octahedral voids, which at low temperatures have axial symmetry S_3 [79, 80]. The asymmetric spectrum, $\kappa >> 1$ and $\eta = 1$, is typical of H_2 trapped in low symmetry sites and it has been observed in low temperature NMR experiments on solid H_2 [81] and on H_2 encased in an asymmetric open cage fullerene [82]. In the former case the asymmetry in the quadrupolar field is related to the local distribution of ortho and para molecule while in the latter case it is related to the low symmetry of the confining molecular field. The powder spectrum associated to the NMR transitions in equation (6.14) is characteristic of dipolar interaction in the solid phase as observed by Pake for the first time [83]: neglecting broadening effects the spectrum extends in frequency for a value double the dipolar constant and a peak to peak separation given by one dipolar constant. In ortho-H_2 the quantum average over the rotational state with $J = 1$ reduces effectively the dipolar constant by a factor 3/5.

From the simulations it is not clear which situation represent the experimental NMR spectra observed at low temperatures in $H_2@C_{60}$, figure 5.3 and 5.8. The observed low-temperature spectra may be related to large anisotropies in the fast exchange limit or moderate anisotropies in the slow exchange limit. When the temperature is lowered the slow exchange limit is expected to become more and more significant. Interestingly the simulated spectra with small local field ($|\kappa| = 2$ and large biaxiality $\eta = 0.66, 1$) in figure 5.3 display a definite central peak with a clear shoulder for $\eta < 1$ and look similar to the experimental ones at 14.1 T, figure 5.3. So the presence/absence of a shoulder in the low-temperature experimental spectra of the two $H_2@C_{60}$ may be related to slightly different local fields depending on the different amount or type of occluded impurities. Anyway the broad pattern at the base of the simulated spectra has not been observed even in the quadrupolar echo experimental spectra, figure 5.4. In the real sample the

situation may be complicated by a distribution of local fields and rotational rates. It is also likely that the observed spectra are in an intermediate dynamical regime. At the moment none of the possible scenarios should be ruled out without further experimental and theoretical analysis.

6.3 Spin-lattice relaxation

In this section the theory of nuclear spin-lattice relaxation in $H_2@C_{60}$ is presented. Although the discussion is not complete, the reported results represent a reference for future theoretical developments aiming to the interpretation of the experimental data in solid endohedral hydrogen fullerenes.

The nuclear spin relaxation for hydrogen in solid non magnetic host was studied by Fedders [84, 85] in the high temperature limit $k_B T > \hbar\delta$. Within such limitation his results can be extended directly to the ground state of $H_2@C_{60}$ without any consideration of the translational motion. In this section the theory is extended beyond the high temperature approximation in order to be able to discuss experimental observations in $H_2@C_{60}$ below 2 K.

In high magnetic field the spin-rotation and the dipolar interaction are small compared to the nuclear Zeeman Hamiltonian. The nuclear spins are affected by the lattice dynamics, however fast that is, through the bottleneck of spin-rotation and intramolecular dipolar interaction. The study of nuclear spin relaxation can be reduced into two steps: first determine the influence of the lattice dynamics on the molecular spin and then transfer this information on the nuclear spin. The spin-lattice relaxation time of a nuclear spin $I = 1$ with the Hamiltonian of equation (6.11) is

$$\begin{aligned}(\mathrm{T}_1)^{-1} &= \omega_c^2 \sum_{q=-1}^{1} q^2\, J^1_{qq}(q\omega_\mathrm{H}) + \frac{9\omega_d^2}{50} \sum_{q=-2}^{2} q^2\, J^2_{qq}(q\omega_\mathrm{H}) \\ &= 2\omega_c^2 J^1_{11}(\omega_\mathrm{H}) + \frac{9\omega_d^2}{25}\left[J^2_{11}(\omega_\mathrm{H}) + 4J^2_{22}(2\omega_\mathrm{H})\right]\end{aligned} \tag{6.19}$$

in the assumption that the nuclear spin has a negligible influence on the molecular spin dynamics [84]. This result follows directly from Redfield relaxation theory at second-order [86], assuming no cross-correlation between spherical operators with different spherical rank. The influence of the lattice on the spin system is conveyed by spectral densities J^k_{qq} which are Fourier transforms of the correlation functions of spherical

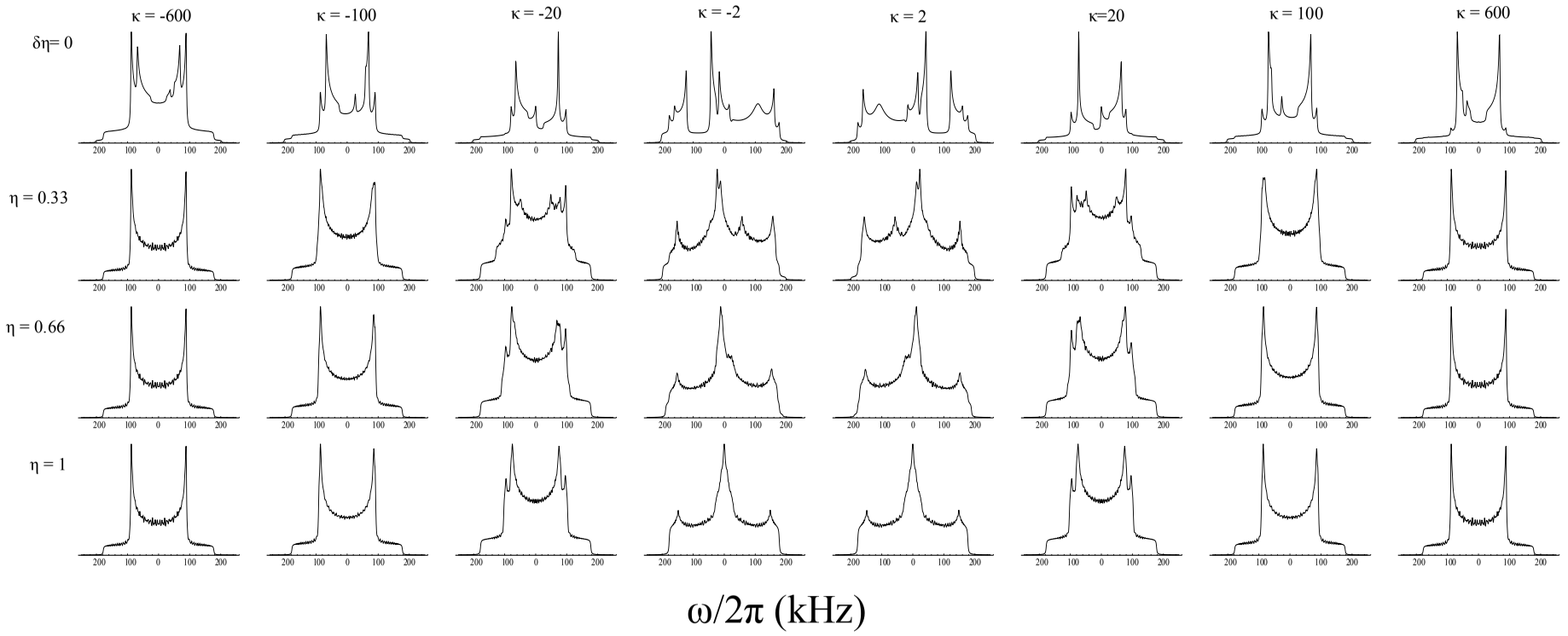

Figure 6.3: Simulated powder ^{1}H spectra for $H_2@C_{60}$ at 14.1 T field and 2K in presence of quadrupolar field acting on the molecular spin Λ in the slow exchange limit. The panels show the dependence of the NMR spectrum with respect to the anisotropy δ and biaxiality η of the quadrupolar Λ-Hamiltonian, equation (6.9). The effective value of the anisotropy is obtained using $\delta = \kappa\omega_J$ with $\omega_J \approx 100$MHz at 14.1 T.

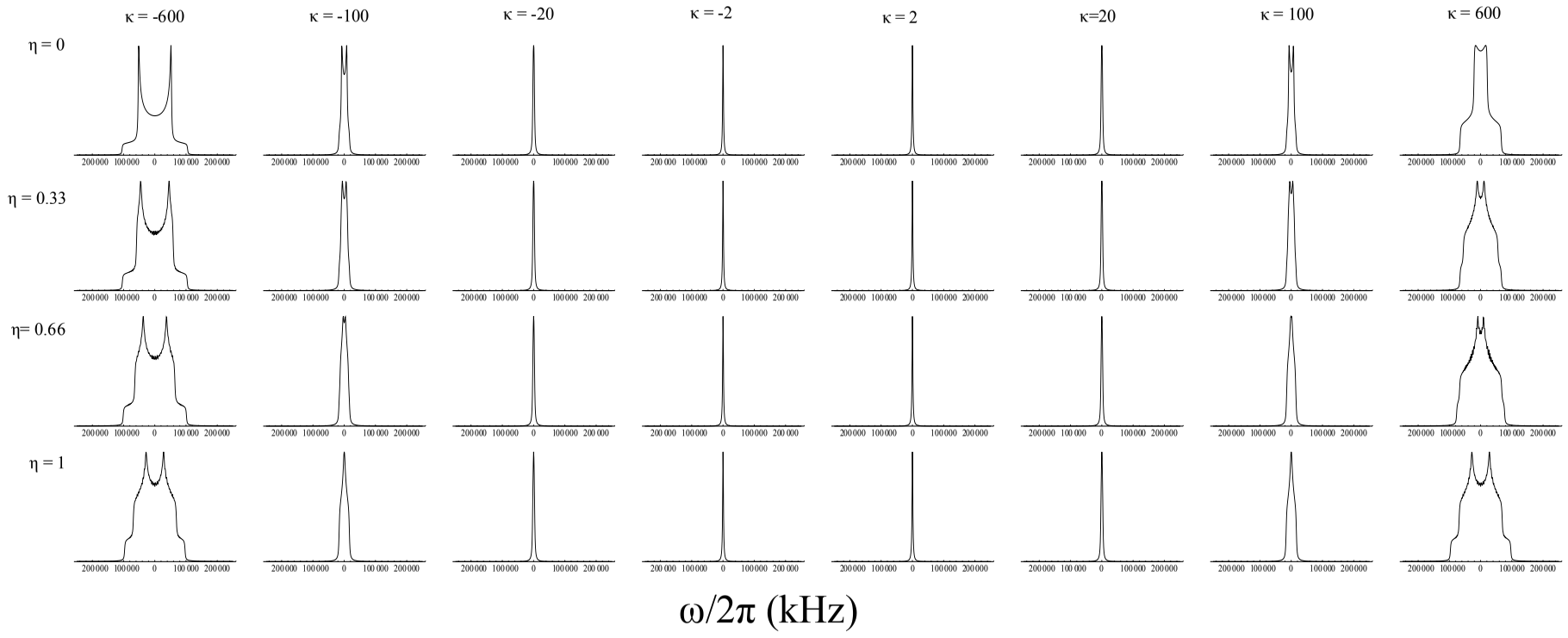

Figure 6.4: Simulated powder ^{1}H spectra for $H_2@C_{60}$ at 14.1 T field and 2K in presence of quadrupolar field acting on the molecular spin Λ in the fast exchange limit. The panels show the dependence of the NMR spectrum with respect to the anisotropy δ and biaxiality η of the quadrupolar Λ-Hamiltonian, equation (6.9). The effective value of the anisotropy is obtained using $\delta = \kappa\omega_J$ with $\omega_J \approx 100$MHz at 14.1 T.

operators

$$J^k_{q_1q_2}(\omega) = \mathrm{Re}\int_0^\infty G^k_{q_1q_2}(t)\,\mathrm{e}^{-\mathrm{i}\omega t}\mathrm{d}\,t \tag{6.20a}$$

$$G^k_{q_1q_2}(t) = \langle\left[T^k_{q_1}(\mathbf{\Lambda})\right]^\dagger T^k_{q_2}(\mathbf{\Lambda})(-t)\rangle = \mathrm{Tr}_{M_\Lambda}\left[\left[T^k_{q_1}(\mathbf{\Lambda})\right]^\dagger T^k_{q_2}(\mathbf{\Lambda})(-t)\rho_{\mathbf{\Lambda}}(T)\right] \tag{6.20b}$$

where

$$\rho_{\mathbf{\Lambda}}(T) = \frac{\mathrm{e}^{\frac{\hbar\mathcal{H}_\Lambda}{k_BT}}}{\mathrm{Tr}_{M_\Lambda}\mathrm{e}^{\frac{\hbar\mathcal{H}_\Lambda}{k_BT}}} \tag{6.21}$$

is the molecular spin density at thermal equilibrium. The time dependence of the spherical operators is determined by the Liouvillian of the molecular spin, see below.

When the quadrupolar interaction $\mathcal{H}_{Q_\Lambda}$ is larger than the Zeeman interaction it is convenient to work with the correlation functions and the spectral densities in the principal frame of the former Hamiltonian. The correlation functions in the principal frame are denoted by a bar and are obtained by replacing $\mathbf{\Lambda}$ by $\mathbf{\Lambda}_P$ in equation (6.20) and in equation (6.27). The correlation functions in the laboratory frame and in the principal frame are related by Wigner matrices. For example

$$J^k_{qq}(\omega) = \sum_{q_1,q_2}\left[D^k_{q,q_1}(\alpha,\beta,\gamma)\right]^* D^k_{q,q_2}(\alpha,\beta,\gamma)\overline{J}^k_{q_1q_2}(\omega). \tag{6.22}$$

The idea is that at large local field the angular dependence of $\overline{J}$ is weak and J depend on the orientation mainly through the Wigner matrices. To simplify the treatment only the dependence on β is considered in the following, i.e. α=γ=0. When the relaxation time depends on the orientation of the local field with respect to the static magnetic field the orientation-averaged rate

$$(\mathrm{T}_{1a})^{-1} = \frac{1}{2}\int\left[\mathrm{T}_1(\beta)\right]^{-1}\sin\beta\mathrm{d}\beta \tag{6.23}$$

determines the recovery of the signal for $t << \mathrm{T}_{1a}$:

$$s(t) = \frac{1}{2}\int\mathrm{e}^{-t/\mathrm{T}_1(\beta)}\mathrm{d}\beta \approx \mathrm{e}^{-t/\mathrm{T}_{1a}}. \tag{6.24}$$

The discussion will be now be divided according to the local symmetry at the H_2 site. To simplify the notation we introduce the Lorentz function

$$\mathcal{J}(\omega,\Gamma) = \frac{\Gamma}{\omega^2+\Gamma^2}, \tag{6.25}$$

which is recurring frequently in the evaluation of spectral densities and the parameters

$$\delta' = \sqrt{3/2}\delta, \tag{6.26a}$$
$$x = \hbar\delta'/(k_B T). \tag{6.26b}$$

6.3.1 Cubic symmetry

In an environment with cubic symmetry $\mathcal{H}_{Q_\Lambda}$=0. At any temperature of interest the high temperature approximation holds: $\hbar\mathcal{H}_{Z_\Lambda}/k_B T << 1$. As a consequence $\rho_{\mathbf{\Lambda}}(T) \approx 1/3$ and the evolution of the spherical tensors in Λ is determined by the equation of motion [84]

$$\frac{\mathrm{d}T_q^k(\mathbf{\Lambda})}{\mathrm{d}t} = -\mathrm{i}\left[T_q^k(\mathbf{\Lambda}), \mathcal{H}_\Lambda\right] - \Gamma_k T_q^k(\mathbf{\Lambda}) \tag{6.27}$$

Γ_k plays the role of decay rates (inverse of correlation times) for the rotational operator of rank k and depends parametrically on the angular momentum of the state. For rank 1 and 2 one has [87, 84]

$$\Gamma_1 = 5J_L(0), \tag{6.28a}$$
$$\Gamma_2 = 3J_L(0), \tag{6.28b}$$

where $J_L(\omega)$ is the correlation function for the lattice. The main assumption here is that the lattice correlation function is flat in the frequency range determined by the exchanged quanta in the nuclear spin molecular spin system: $J_L(\omega) = J_L(0)$.

The spherical tensors are normal modes of the Liouville equation (6.27)

$$T_q^k(\mathbf{\Lambda})(t) = \mathrm{e}^{(\mathrm{i}\,q\,\omega_\Lambda - \Gamma_k)t} T_q^k(\mathbf{\Lambda}) \tag{6.29}$$

so that the correlation functions are

$$J_{qq}^k(\omega) = \frac{\left|T^k(\mathbf{\Lambda})\right|^2}{(2\Lambda+1)}\mathcal{J}(q\omega - q\omega_\Lambda, \Gamma_k) \Rightarrow \begin{cases} J_{qq}^1(\omega) = \frac{2}{3}\mathcal{J}(q\omega - q\omega_\Lambda, \Gamma_1), \\ J_{qq}^2(\omega) = \frac{1}{3}\mathcal{J}(q\omega - q\omega_\Lambda, \Gamma_2). \end{cases} \tag{6.30}$$

where the norm of the a spin operator is given by equation (2.34): for $\Lambda = 1$, $\left|T^1(\mathbf{\Lambda})\right|^2 = 2$ and $\left|T^2(\mathbf{\Lambda})\right|^2 = 1$. The relaxation time is given by the well-known expression [88, 89, 84]:

$$(\mathrm{T}_1)^{-1} = \frac{4}{3}\omega_c^2\mathcal{J}(\omega_\mathrm{H} - \omega_\Lambda, \Gamma_1) + \frac{3}{25}\omega_d^2\left[\mathcal{J}(\omega_\mathrm{H} - \omega_\Lambda, \Gamma_2) + 4\mathcal{J}(2\omega_\mathrm{H} - 2\omega_\Lambda, \Gamma_2)\right]. \tag{6.31}$$

6.3.2 Axial symmetry

At site of axial symmetry $\eta = 0$. For sake of simplicity only the case of large local field $\omega_H << \delta'$ will be discussed. It is not possible to assume a priori that $\rho_\Lambda(T) = 1/3$ in equation (6.20) unless $\hbar\delta' << k_B T$. When $\hbar\delta' \geq k_B T$ one has to use a modified equation of motion, rather than equation (6.29), to take into account the temperature dependence of the Liouvillian [90]. In the limit of large electric field the projection of the molecular spin along the axis of symmetry is a good quantum number. The spectral densities $\overline{J}^k_{q_1 q_2}(\omega)$ with $q_1 \neq q_2$ or $|q_1| = |q_2| = 1$ are depressed as Γ/δ'. The relevant non-null correlation functions are:

$$\overline{J}^1_{00}(\omega) = \frac{2}{2 + e^{2x}} \mathcal{J}(\omega, \Gamma_{10}) \tag{6.32a}$$

$$\overline{J}^2_{00}(\omega) = \frac{3 + \tanh x}{3(3 - \tanh x)} \mathcal{J}(\omega, \Gamma_{20}) \tag{6.32b}$$

$$\overline{J}^2_{\pm 2 \pm 2}(\omega; \beta) = \frac{1}{2 + e^{2x}} \mathcal{J}\left(\omega \pm 2\omega_\Lambda \cos\beta, \Gamma_{22}\right) \tag{6.32c}$$

where

$$\Gamma_{10} = 4J_L(0) + J_L(3\kappa)\,[1 + \tanh x] \tag{6.33a}$$

$$\Gamma_{20} = J_L(3\kappa)\,[3 - \tanh x] \tag{6.33b}$$

$$\Gamma_{22} = 2J_L(0) + J_L(3\kappa)\,[1 + \tanh x] \tag{6.33c}$$

Averaging of the Wigner matrices over the β angles in equation (6.22) accounts for a reduction of a factor 1/3 of the spin-rotation relaxation path (rank 1) and a factor 3/5 for the dipolar relaxation path with respect to the cubic symmetry. The dependence of the correlation functions on the angle β, equation (6.32), is taken into account by a first-order expansion in ω_Λ/ω_H. The orientation-averaged rate is

$$(T_{1a})^{-1} = \frac{2}{3}\omega_c^2 \overline{J}^1_{00}(\omega_H) + \frac{9}{125}\omega_d^2 \left[\overline{J}^2_{00}(\omega_H) + 2\overline{J}^2_{22}(\omega_H; \frac{\pi}{2}) \left(1 + 4\omega_H \omega_\Lambda \frac{\mathcal{J}(\omega_H, \Gamma_{22})}{3\Gamma_{22}} \right) + \right.$$

$$\left. + 4\overline{J}^2_{00}(2\omega_H) + 8\overline{J}^2_{22}(2\omega_H; \frac{\pi}{2}) \left(1 + 16\omega_H \omega_\Lambda \frac{\mathcal{J}(2\omega_H, \Gamma_{22})}{3\Gamma_{22}} \right) \right]. \tag{6.34}$$

Higher order corrections modify the rate by less than 1%.

6.3.3 No symmetry

At sites where there is no special symmetry $\eta \neq 0$. Only the case of large local field $\delta' >> \omega_H$ and maximum biaxaility $\eta = 1$ will be considered. In the limit of large electric field all the spectral densities $\overline{J}^k_{q_1 q_2}(\omega)$ with rank 1 or with $|q_1| = |q_2| = 1$ are depressed

as Γ/δ': the spin-rotation mechanism is completely quenched and relaxation is purely dipolar. Using the definitions in equation (6.26) the finite correlation functions of rank 2 are written as

$$\overline{J}^2_{00}(\omega) = f(s,t)\mathcal{J}(\omega,\Gamma_2) + g(s,t)\mathcal{J}(\omega,\Gamma'_2), \tag{6.35a}$$

$$\overline{J}^2_{02}(\omega) = \overline{J}^2_{20}(\omega) = \sqrt{\frac{2}{3}}\left(\frac{3-s}{1+s}\right) f(s,t)\mathcal{J}(\omega,\Gamma_2) + \sqrt{\frac{2}{3}}\left(\frac{3+s}{1-s}\right) g(s,t)\mathcal{J}(\omega,\Gamma'_2), \tag{6.35b}$$

$$\overline{J}^2_{\pm2\pm2}(\omega) = \overline{J}^2_{\mp2\pm2}(\omega) = \frac{2}{3}\left(\frac{3-s}{1+s}\right)^2 f(s,t)\mathcal{J}(\omega,\Gamma_2) + \frac{2}{3}\left(\frac{3+s}{1-s}\right)^2 g(s,t)\mathcal{J}(\omega,\Gamma'_2). \tag{6.35c}$$

where the correlation rates are

$$\Gamma_2 = J_L(\kappa)\left[3 + s\frac{3-s^2}{1+s^2}\right] \tag{6.36a}$$

$$\Gamma'_2 = J_L(\kappa)\left[3 - s\frac{3-s^2}{1+s^2}\right] \tag{6.36b}$$

and the supporting functions are

$$f(s,t) = \begin{cases} \frac{(1+s)^2(4s+t)}{32s(3+s^2)} \text{ if } \delta' < 0, \\ \frac{(1+s)^2(4s-t)}{32s(3+s^2)} \text{ if } \delta' > 0. \end{cases} \tag{6.37a}$$

$$g(s,t) = \begin{cases} \frac{(1-s)^2(4s-t)}{32s(3+s^2)} \text{ if } \delta' < 0, \\ \frac{(1-s)^2(4s+t)}{32s(3+s^2)} \text{ if } \delta' > 0. \end{cases} \tag{6.37b}$$

with $s = \sqrt{1+\operatorname{sech} x}$ and $t = \tanh x$.

Since the correlation functions does not depend explicitly on the angle β, the orientation-averaged rate is obtained by integrating the angular dependence of the Wigner matrices

$$(\mathrm{T}_{1a})^{-1} = \frac{3}{125}\omega_d^2\Big[3\overline{J}^2_{00}(\omega_\mathrm{H}) + 12\overline{J}^2_{00}(2\omega_\mathrm{H}) + 2\overline{J}^2_{22}(\omega_\mathrm{H}) + 14\overline{J}^2_{22}(2\omega_\mathrm{H}) - 2\sqrt{6}\overline{J}^2_{20}(\omega_\mathrm{H}) + 12\sqrt{6}\overline{J}^2_{20}(2\omega_\mathrm{H})\Big]. \tag{6.38}$$

6.3.4 Interaction with the lattice

In $\mathrm{H_2@C_{60}}$ the lattice consists of all the degrees of freedom that are associated to the fullerene cages. For each $\mathrm{C_{60}}$ molecule there are 174 normal vibrational modes, 3 rotational modes and 3 translational modes. In the solid state the translational modes of the fullerenes are not independent but form a bath of phonons. Vibrational modes, rotations and phonons are the quantum lattice for $\mathrm{H_2@C_{60}}$. The intramolecular vibrational modes

are not involved in the dynamics of the sub-rotational levels since their frequency are greater than 250 cm^{-1}. In $H_2@C_{60}$ the coupling constant between the rotations of C_{60} and the ones of H_2 is related to small non spherical term in the cage-hydrogen potential. Relaxation though this channel is a second-order effect that depends on the mixing of the rotational ground state with excited roto-translational state with $\Lambda \geq 5$. Relaxation through interaction with the rotational modes of C_{60} is negligible. At any temperatures of interest for the study of ortho-$H_2@C_{60}$, the relaxation of the spin system is expected to be determined only through the phonon channel. The exact evaluation of the coupling between phonons and rotations in C_{60} and the evaluation of the quantum correlation functions are necessary for a quantitative comparison between the experimental and the theoretical relaxation rates. This last step will be subject to future theoretical developments.

6.4 Conclusions

In this chapter the spin dynamics of $H_2@C_{60}$ has been discussed. The general spin Hamiltonian of H_2 in the confined fullerene is discussed with attention to the scaling factors for spin-rotation and dipolar interactions in excited roto-translational states. The discussion of the scaling factors is fundamental for the analysis of high-temperature relaxation studies. NMR spectra of $H_2@C_{60}$ in the ground rotational-translational state are simulated in the limiting case of fast and slow thermal exchange among the rotational levels. The expressions of spin-lattice relaxation rates are given extending Fedders' theory to temperatures lower than the eventual splitting in the ortho-H_2 ground state.

The model discussed here is the starting point for more detailed studies of nuclear spin dynamics in $H_2@C_{60}$. A more complete formulation of the problem, which incorporate the dynamics of the rotational levels from the beginning by use of Liouville formalism, is in progress. The assumption of the independence of the combined nuclear spin molecular rotation Hamiltonian among nearby molecules is questionable. Although the protective cage is supposed to isolate the reciprocal interactions among hydrogen molecules, it is possible that electric quadrupole-quadrupole interactions may play a role in the dynamics of the rotational modes. More experimental studies on differently prepared sample, for example $H_2@C_{60}$ dilute with empty C_{60}, are in progress.

Chapter 7

Conclusions and final remarks

The aim of this Ph.D. thesis is to elucidate the quantum dynamics of the prototypical endohedral hydrogen-fullerene complex $H_2@C_{60}$ by means of theory and experiments. Infrared spectroscopy (IR) and nuclear magnetic resonance (NMR) have been used to probe the spatial and nuclear spin dynamics in $H_2@C_{60}$, respectively. The first part of the thesis deals with the development of the theoretical framework used to describe the vibrational-rotational-translational dynamics of the confined hydrogen, followed by a detailed analysis of the IR spectra of $H_2@C_{60}$. The second part of the thesis deals with the investigations of nuclear spin lineshapes and relaxation rates at cryogenic temperatures. The main outcomes of this work may be resumed in the following points:

- an efficient computational method for the representation of the Hamiltonian and electric dipole moment of endohedral hydrogen fullerenes. The method is based on the expansion of the confining potential and electric moment in terms of spherical multipoles and has been implemented in Mathematica[32] notebooks for fast simulations of the IR spectra of $H_2@C_{60}$ and recently $HD@C_{60}$ and $D_2@C_{60}$[91];

- the quantitative analysis of the infrared spectroscopy of $H_2@C_{60}$ between 300 to 6 K via the method discussed above leading to molecular parameters of the confined molecule, effective potentials for the roto-translational motion in the ground and first vibrational states and estimates of the induced dipole moment;

- a comparative NMR study of two samples of $H_2@C_{60}$ with different preparation histories;

- the study of the proton NMR lineshape and spin-lattice relaxation between 2 and 0.1 K;

- a preliminary theoretical framework for the analysis of the NMR spin dynamics in the solid state.

The agreement between the experimental IR spectra and the theoretical model is remarkable proving that the quantum dynamics and the infrared activity of endohedral

hydrogen are determined by non-bonding interactions between the two molecular entities at the level of a single supra-molecular unit. In particular it was found that:

- the rotational constant of the endohedral hydrogen, 59.9 cm^{-1}, is approximately 0.8% smaller than in free hydrogen, implying a longer internuclear equilibrium distance in the confined case.
- the fundamental vibrational frequency is redshifted approximatively 100 cm^{-1} than in free hydrogen;
- the longer internuclear distance and the redshift in vibrational frequency with respect to the free molecule are consistent with an attractive interaction between the hydrogen atoms and the C_{60} walls;
- the fundamental translational excitations, $N = 0$ to $N = 1$, in the ground and first excited vibrational state are 179.5 and 184.4 cm^{-1}, respectively. The largest contributions, about 130-140 cm^{-1}, comes from the harmonic attractive potential towards the center of the cage and the residual 20-25% from anharmonic corrections.

The experimental low-temperature NMR spectra show evidence of a dipolar powder pattern typical of free rotating ortho-hydrogen trapped in sites with reduced symmetry. NMR simulations indicate that observed spectra are consistent with a small local fields capable to lift degeneracy of the rotational levels in icosahedral symmetry. Such anisotropies may be related to distribution of ortho/para molecules in the nearby cages, imperfections in the lattice or occluded impurities.

Although the successful overall interpretation of the IR spectra, some of the observed features can not by explained in terms infrared activity in a single isolated supermolecule. These comprise the observation of the fundamental vibrational transitions and few splittings in some of the IR lines. The topic of infrared activity in the solid including static effects, as crystal fields induced by a low symmetry in the lattice, and dynamical effects, i.e. lattice vibrations, have not been discussed here and deserve a proper quantitative treatment. These deviations from the perfect icosahedral symmetry are consistent with the NMR findings. The advancement in the interpretation of the NMR observations is linked to a better understanding of the rotational dynamics in $H_2@C_{60}$. Experimental studies on diluted hydrogen fullerenes as well as on other confined isotopomers, that may improve the understanding of the nuclear spin dynamics, and the development of a more complete theoretical model to be used in the analysis of the NMR lineshapes and spin relaxations in endohedral fullerenes are in progress.

Bibliography

[1] R. J. Cross, *The Journal of Physical Chemistry A* **105**, 6943 (2001).

[2] M. Xu, F. Sebastianelli, B. R. Gibbons, Z. Bacić, R. Lawler, and N. J. Turro, *The Journal of chemical physics* **130**, 224306 (2009).

[3] G. Herzberg, *Molecular spectra and molecular structure, I. Spectra of diatomic molecules*, Van Nostrand Company, Inc. (Princeton), 2th edition, 1950.

[4] H. W. Kroto, J. R. Heath, S. C. O'Brien, R. F. Curl, and R. E. Smalley, *Nature* **318**, 162 (1985).

[5] A. Farkas, *Orthohydrogen, parahydrogen and heavy hydrogen*, Cambridge University Press, Cambridge (UK), 1935.

[6] W. I. F. David, R. M. Ibberson, J. C. Matthewman, K. Prassides, T. J. S. Dennis, J. P. Hare, H. W. Kroto, R. Taylor, and D. R. M. Walton, *Nature* **353**, 147 (1991).

[7] P. Heiney, J. Fischer, A. McGhie, W. Romanow, A. Denenstein, J. McCauley Jr., A. Smith, and D. Cox, *Physical Review Letters* **66**, 2911 (1991).

[8] R. Tycko, G. Dabbagh, R. M. Fleming, R. C. Haddon, A. V. Makhija, and S. M. Zahurak, *Physical Review Letters* **67**, 1886 (1991).

[9] P. Heiney, J. Fischer, A. McGhie, W. Romanow, A. Denenstein, J. McCauley, A. Smith, and D. Cox, *Physical Review Letters* **67**, 1468 (1991).

[10] R. Sachidanandam and A. Harris, *Physical Review Letters* **67**, 1467 (1991).

[11] W. Schranz, A. Fuith, P. Dolinar, H. Warhanek, M. Haluska, and H. Kuzmany, *Physical Review Letters* **71**, 1561 (1993).

[12] J. R. Heath, S. C. O'Brien, Q. Zhang, Y. Liu, R. F. Curl, F. K. Tittel, and R. E. Smalley, *Journal of the American Chemical Society* **107**, 7779 (1985).

[13] Y. Chai, T. Guo, C. Jin, R. E. Haufler, L. P. F. Chibante, J. Fure, L. Wang, J. M. Alford, and R. E. Smalley, *The Journal of Physical Chemistry* **95**, 7564 (1991).

[14] R. D. Johnson, M. S. de Vries, J. Salem, D. S. Bethune, and C. S. Yannoni, *Nature* **355**, 239 (1992).

[15] S. Stevenson, G. Rice, T. Glass, K. Harich, F. Cromer, M. R. Jordan, J. Craft, E. Hadju, R. Bible, M. M. Olmstead, K. Maitra, A. J. Fisher, A. L. Balch, H. C. Dorn, and Others, *Nature* **401**, 55 (1999).

[16] M. Krause, M. Hulman, H. Kuzmany, O. Dubay, G. Kresse, K. Vietze, G. Seifert, C. Wang, and H. Shinohara, *Physical Review Letters* **93**, 2 (2004).

[17] K. H. Michel, B. Verberck, M. Hulman, H. Kuzmany, and M. Krause, *The Journal of chemical physics* **126**, 064304 (2007).

[18] M. Saunders, H. a. Jimenez-Vazquez, R. J. Cross, S. Mroczkowski, M. L. Gross, D. E. Giblin, and R. J. Poreda, *Journal of the American Chemical Society* **116**, 2193 (1994).

[19] M. Saunders, R. J. J. Cross, H. A. Jimenez-Vazquez, R. Shimshi, and A. Khong, *Science (New York, N.Y.)* **271**, 1693 (1996).

[20] A. Khong, H. a. Jiménez-Vázquez, M. Saunders, R. J. Cross, J. Laskin, T. Peres, C. Lifshitz, R. Strongin, and A. B. Smith, *Journal of the American Chemical Society* **120**, 6380 (1998).

[21] Y. Murata, M. Murata, and K. Komatsu, *Journal of the American Chemical Society* **125**, 7152 (2003).

[22] K. Komatsu, M. Murata, and Y. Murata, *Science (New York, N.Y.)* **307**, 238 (2005).

[23] M. Murata, Y. Murata, and K. Komatsu, *Journal of the American Chemical Society* **128**, 8024 (2006).

[24] M. Murata, S. Maeda, Y. Morinaka, Y. Murata, and K. Komatsu, *Journal of the American Chemical Society* **130**, 15800 (2008).

[25] S. Mamone, J. Y.-C. Chen, R. Bhattacharyya, M. H. Levitt, R. G. Lawler, A. J. Horsewill, T. Rõõm, Z. Bačić, and N. J. Turro, *Coordination Chemistry Reviews* (2011).

[26] M. E. Rose, *Elementary Theory of Angular Momentum*, John Wiley & Sons, Inc, 1957.

[27] A. R. Edmonds, *Angular Momentum in Quantum Mechanics*, Princeton University Press, ii edition, 1960.

[28] D. M. Brink and G. Satchler, *Angular Momentum*, Oxford University Press, Oxford, iii edition, 1994.

[29] D. A. Varshalovich, A. N. Moskalev, and V. K. Kheronskii, *Quantum Theory of Angular Momentum*, World Scientific, Singapore, 1988.

[30] R. N. Zare, *Angular Momentum: Understanding Spatial Aspects in Chemistry and Physics*, 1 edition, 1988.

[31] H. Jahn and J. Hope, *Physical Review* **93**, 318 (1954).

[32] Wolfram Research, Mathematica, 2010.

[33] B. C. Sanctuary, *The Journal of Chemical Physics* **64**, 4352 (1976).

[34] D. Smith and J. H. M. Thornley, *Proceedings of the Physical Society* **89**, 779 (1966).

[35] W. Gordy and R. L. Cook, *Microwave Molecular Spectra*, Wiley-Interscience, iii edition, 1984.

[36] M. Abramowitz and I. A. Stegun, *Handbook of mathematical functions*, Dover Publication, New York, 1964.

[37] P. R. Fontana, *Journal of Mathematical Physics* **2**, 825 (1961).

[38] S. Mamone, G. Pileio, and M. H. Levitt, *Symmetry* **2**, 1423 (2010).

[39] M. Xu, F. Sebastianelli, K. Bacic, R. Lawler, and N. J. Turro, *J. Chem. Phys.* **128**, 11101 (2008).

[40] C. Cohen-Tannoudji, B. Diu, and F. Laloe, *Quantum mechanics*, Wiley (New York), 1 edition, 1977.

[41] D. VEIRS and G. ROSENBLATT, *Journal of Molecular Spectroscopy* **121**, 401 (1987).

[42] W. Shaffer, *Reviews of Modern Physics* **16**, 245 (1944).

[43] W. SHAFFER and B. KROHN, *Journal of Molecular Spectroscopy* **63**, 323 (1976).

[44] J. M. Brown and A. Carrington, *Rotational Spectroscopy of Diatomic Molecules*, Cambridge University Press, 2003.

[45] J. L. Hunt and H. L. Welsh, *Canadian Journal of Physics* **42**, 873 (1964).

[46] H. Gush, W. Hare, E. Allen, and H. Welsh, *Canadian Journal of Physics* **38**, 176 (1960).

[47] J. VANKRANENDONK, *Physica* **23**, 825 (1957).

[48] J. VANKRANENDONK, *Physica* **24**, 347 (1958).

[49] J. D. Poll and J. V. Kranendonk, *Canadian Journal of Physics* **39**, 189 (1961).

[50] S. FitzGerald, S. Forth, and M. Rinkoski, *Physical Review B* **65**, 2 (2002).

[51] S. FitzGerald, H. Churchill, P. Korngut, C. Simmons, and Y. Strangas, *Physical Review B* **73**, 1 (2006).

[52] R. Herman and J. Lewis, *Physical Review B* **73**, 1 (2006).

[53] W. Meyer and L. Frommhold, *Physical Review A* **34**, 2771 (1986).

[54] W. Meyer and L. Frommhold, *Physical Review A* **34**, 2936 (1986).

[55] J. D. D. Poll and J. L. L. Hunt, *Canadian Journal of Physics* **54**, 461 (1976).

[56] R. Loudon, *The quantum theory of light*, Oxford University Press, 2000.

[57] R. C. Hilborn, *American Journal of Physics* **50**, 982 (1982).

[58] J. Hora, P. Pánek, K. Navrátil, B. Handlířová, J. Humlíček, H. Sitter, and D. Stifter, *Physical Review B* **54**, 5106 (1996).

[59] S. Mamone, M. Ge, D. Hüvonen, U. Nagel, A. Danquigny, F. Cuda, M. C. Grossel, Y. Murata, K. Komatsu, M. H. Levitt, T. Rõõm, M. Carravetta, Min Ge, D. Hüvonen, U. Nagel, A. Danquigny, F. Cuda, M. C. Grossel, Y. Murata, K. Komatsu, M. H. Levitt, T. R\?o\?om, and M. Carravetta, *The Journal of chemical physics* **130**, 081103 (2009).

[60] M. Ge, U. Nagel, D. Hüvonen, T. Rõõm, S. Mamone, M. H. Levitt, M. Carravetta, Y. Murata, K. Komatsu, J. Y.-C. Chen, and N. J. Turro, *The Journal of chemical physics* **134**, 054507 (2011).

[61] N. J. Turro, A. A. Martí, J. Y.-C. Chen, S. Jockusch, R. G. Lawler, M. Ruzzi, E. Sartori, S.-C. Chuang, K. Komatsu, and Y. Murata, *Journal of the American Chemical Society* **130**, 10506 (2008).

[62] N. J. Turro, J. Y.-C. Chen, E. Sartori, M. Ruzzi, A. Marti, R. Lawler, S. Jockusch, J. López-Gejo, K. Komatsu, Y. Murata, and J. L. Opez-gejo, *Accounts of chemical research* **43**, 335 (2010).

[63] M. Martin, X. Du, J. Kwon, and L. Mihaly, *Physical Review B* **50**, 173 (1994).

[64] a. Horsewill, S. Rols, M. Johnson, Y. Murata, M. Murata, K. Komatsu, M. Carravetta, S. Mamone, M. Levitt, J. Chen, J. Johnson, X. Lei, and N. Turro, *Physical Review B* **82**, 1 (2010).

[65] M. Xu, L. Ulivi, M. Celli, D. Colognesi, and Z. Bačić, *Physical Review B* **83**, 1 (2011).

[66] M. H. Levitt, *Spin Dynamics. Basics of Nuclear Magnetic Resonance*, Wiley, Chichester (UK), 2001.

[67] R. R. Ernst, G. Bodenhausen, and A. Wokaun, *Principles of Nuclear Magnetic Resonance in One and Two Dimensions*, Clarendon Press, Oxford, 1988.

[68] J. Powles, *Physics Letters* **2**, 58 (1962).

[69] M. Carravetta, A. Danquigny, S. Mamone, F. Cuda, O. G. Johannessen, I. Heinmaa, K. Panesar, R. Stern, M. C. Grossel, A. J. Horsewill, A. Samoson, M. Murata, Y. Murata, K. Komatsu, and M. H. Levitt, *Physical chemistry chemical physics : PCCP* **9**, 4879 (2007).

[70] E. V. Krjukov, J. D. O'Neill, and J. R. Owers-Bradley, *Journal of Low Temperature Physics* **140**, 397 (2005).

[71] A. Rao, K.-A. Wang, J. Holden, Y. Wang, P. Zhou, P. Eklund, C. Eloi, and J. Robertson, *Journal of Materials Research* **8**, 2277 (1993).

[72] C. C. Eloi, D. J. Robertson, A. Rao, P. Zhou, K.-A. Wang, and P. C. Eklund, *Journal of Materials Research* **8**, 3085 (1993).

[73] J. Kellogg, I. Rabi, N. Ramsey, and J. Zacharias, *Physical Review* **56**, 728 (1939).

[74] N. F. Ramsey, *Physical Review* **58**, 226 (1940).

[75] A. Harris, *Physical Review B* **1**, 3495 (1970).

[76] Y. Kohama, T. Rachi, J. Jing, Z. Li, J. Tang, R. Kumashiro, S. Izumisawa, H. Kawaji, T. Atake, H. Sawa, Y. Murata, K. Komatsu, and K. Tanigaki, *Physical Review Letters* **103**, 1 (2009).

[77] M. Edén and M. H. Levitt, *J. Magn. Reson.* **132**, 220 (1998).

[78] B. Stevensson and M. Edén, *J. Magn. Reson.* **181**, 162 (2006).

[79] M. Tomaselli and B. H. H. Meier, *The Journal of Chemical Physics* **115**, 11017 (2001).

[80] M. Tomaselli, *Molecular Physics* **101**, 3029 (2003).

[81] F. Reif and E. Purcell, *Physical Review* **91**, 631 (1953).

[82] M. Carravetta, O. G. G. Johannessen, M. H. H. Levitt, I. Heinmaa, R. Stern, A. Samoson, A. J. J. Horsewill, Y. Murata, and K. Komatsu, *The Journal of chemical physics* **124**, 104507 (2006).

[83] G. E. Pake, *The Journal of Chemical Physics* **16**, 327 (1948).

[84] P. Fedders, *Physical Review B* **20**, 2588 (1979).

[85] P. Fedders, *Physical Review B* **30**, 3603 (1984).

[86] A. G. Redfield, *IBM Journal of Research and Development* **1**, 19 (1957).

[87] P. Fedders, *Physical Review B* **10**, 4510 (1974).

[88] M. Bloom, I. Oppenheim, M. Lipsicas, C. G. Wade, and C. F. Yarnell, *The Journal of Chemical Physics* **43**, 1036 (1965).

[89] W. N. Hardy, *Canadian Journal of Physics* **44**, 265 (1966).

[90] P. Hubbard, *Reviews of Modern Physics* **33**, 249 (1961).

[91] M. Ge, U. Nagel, D. Huvonen, T. Room, M. S., M. Levitt, M. Carravetta, Y. Murata, K. Komatsu, X. Lei, and N. J. Turro, *J. Chem. Phys.* **Submitted** (2011).